



저작자표시-비영리-변경금지 2.0 대한민국

이용자는 아래의 조건을 따르는 경우에 한하여 자유롭게

- 이 저작물을 복제, 배포, 전송, 전시, 공연 및 방송할 수 있습니다.

다음과 같은 조건을 따라야 합니다:



저작자표시. 귀하는 원저작자를 표시하여야 합니다.



비영리. 귀하는 이 저작물을 영리 목적으로 이용할 수 없습니다.



변경금지. 귀하는 이 저작물을 개작, 변형 또는 가공할 수 없습니다.

- 귀하는, 이 저작물의 재이용이나 배포의 경우, 이 저작물에 적용된 이용허락조건을 명확하게 나타내어야 합니다.
- 저작권자로부터 별도의 허가를 받으면 이러한 조건들은 적용되지 않습니다.

저작권법에 따른 이용자의 권리는 위의 내용에 의하여 영향을 받지 않습니다.

이것은 [이용허락규약\(Legal Code\)](#)을 이해하기 쉽게 요약한 것입니다.

[Disclaimer](#)

공학박사 학위논문

차세대 배터리용 리튬 공기 이차
전지의 효율 향상에 대한 연구

**Study for high-performance Li air battery as an
advanced energy storage device**

2016년 2월

서울대학교 대학원

재료공학부

임희대

차세대 배터리용 리튬 공기 이차 전지의 효율 향상에 대한 연구

지도교수 강 기 석

이 논문을 공학박사 학위논문으로 제출함
2016 년 2 월

서울대학교 대학원
재료공학부
임 희 대

임희대 의 박사 학위논문을 인준함
2016 년 2 월

위 원 장 _____ 박 병 우 _____ (인)

부위원장 _____ 강 기 석 _____ (인)

위 원 _____ 박 수 영 _____ (인)

위 원 _____ 최 장 욱 _____ (인)

위 원 _____ 이 윤 정 _____ (인)

Abstract

Study for high-performance Li air battery as an advanced energy storage device

Hee-Dae Lim

Department of Materials Science and Engineering

College of Engineering

Seoul National University

The development of a new next-generation battery with high energy density lies at the heart of the emerging electric vehicle market. Among several candidates, the metal-gas battery system is particularly promising because it offers exceptionally high energy density at a level unattainable by conventional lithium-ion batteries. Especially, great interest has emerged on Li-O₂ battery with a hope for ultra-high-energy-density batteries. The Li-O₂ battery can deliver the highest theoretical energy density among any battery type, because the reaction between lithium and oxygen occurs directly on the

electrode surface, without any heavy transition metals or crystal framework, such as LiCoO_2 or LiFePO_4 . However, Li-O_2 batteries have in the past exhibited poor rechargeability and low power capability. While various attempts have been made to resolve these problems, the limitations of poor cyclability and rate capability still remain as critical drawbacks of the Li-O_2 battery. Accordingly, recent research on Li-O_2 batteries has mainly focused on the enhancement of overall electrochemical properties.

In each chapter, I proposed novel approaches for enhancing electrochemical properties of Li-O_2 batteries and introduced new types of metal-air systems such as $\text{Li-O}_2/\text{CO}_2$ battery and Li-SO_2 battery. I believe that the several approaches presented here can be used to guide the development of a new metal-gas system and will bring fresh insight to further the development of Li-air batteries. The content of each chapter is summarized as shown below.

Chapter 2 deals with the controlled porous framework of the woven carbon nanotube (CNT) sheet electrode as a new carbon cathode for Li-O_2 battery. I designed hierarchical carbon electrodes with highly aligned CNT fibrils and demonstrated that the electrode significantly enhanced the cyclability and rate capability of the Li-O_2 battery. The controlled framework of the woven CNT sheet electrode enabled effective formation and decomposition of lithium

peroxide, resulting in enhanced cyclability. The high mechanical strength, conductivity, and flexibility of the CNT fibrils contributed to the enhanced performance.

In **Chapter 3**, I proposed a new air-electrode design that incorporates catalysts in the hierarchically porous framework. A simple process of catalyst loading could successfully retain the optimal air pathways of the hierarchical carbon electrode and provide the condition for effective catalytic activity. The new electrode can deliver the cycle performance over 100 cycles, with 1,000 mAh g⁻¹ at a high current rate of 2 A g⁻¹. Additionally, I demonstrated how the Pt catalyst affected the morphology of the discharge products, which resulted in the enhanced cyclability of the Pt/CNT electrode.

Chapter 4 introduces a novel Li-O₂ battery using a soluble catalyst combined with a hierarchical nanoporous air-electrode. I combined a hierarchical nanoporous air-electrode with the LiI redox mediator as a soluble catalyst. A cross-woven CNT fibril sheet provided homogeneous macro- and microscale pores to facilitate the rapid transport of both the reaction ions and the catalyst. The porous three-dimensional network structure of the air-electrode provided a rapid ‘highway’ for the soluble catalyst, which resulted

in a markedly increased energy efficiency and enhanced cyclability. This will spur discussion of the optimal design of electrode architecture and the catalyst activity in Li-O₂ batteries and will attract broad interest in the field of energy storage and conversion.

Chapter 5 deals with the effect of CO₂ on the Li-air battery cell systems based on quantum mechanical (QM) calculations coupled with experimental verification. Up until now, most studies of lithium-air batteries were focused on the battery mechanism/operation in a pure oxygen environment; therefore, such devices should technically be called “lithium-oxygen batteries”. Consequently, to achieve the next step for a lithium-“air” battery, it is critical to understand how the reaction chemistry of such a battery is affected by non-O₂ components of ambient air (such as N₂, Ar, and CO₂). Despite their abundance in ambient air, N₂ and Ar, a noble gas, barely react with Li electrochemically within the cathode potential range, whereas CO₂ can potentially react with Li to yield Li₂CO₃ within the cathode voltage range. It was found that the presence of CO₂ significantly affects the discharge product of a Li-air cell and that the reaction pathways can be leveraged by changing the electrolyte.

Exploring a new chemistry in metal-gas systems plays a key role in creating new possibilities in the development of an ultra-high-energy-density battery. In **Chapter 6**, I shed new light on conventional Li-SO₂ batteries, which have been widely used for military devices because of their wide operating temperature range, high energy density, and long shelf life. Although Li-SO₂ batteries have been used as primary batteries to date, the feasibility of a rechargeable Li-SO₂ battery is demonstrated here based on the reversible formation and decomposition of the solid product, Li₂S₂O₄. The charge polarization is markedly lower than that of a Li-O₂ cell even without a catalyst. Consequently, the observed energy efficiency of the Li-SO₂ system is significantly better than that of the Li-O₂ system.

Keywords: battery, energy storage, air battery, O₂ battery, catalyst, Li-SO₂ battery, soluble catalyst

Student Number: 2011-30942

Table of Contents

Abstract	3
Table of Contents	8
List of Figures	11
List of Tables	15
Chapter 1. Introduction	
1.1 Research Background.....	16
1.2 References	20
Chapter 2. Cathode Design for Reversible Li Air Battery	
2.1 Introduction	23
2.2 Experimental Details	26
2.3 Results and Discussion	
2.3.1 Fabrication of well-aligned CNT fibril sheets.....	27
2.3.2 Electrochemical properties	28
2.3.3 The origin of the enhanced performances	30
2.4 Conclusion.....	34
2.5 References	42
Chapter 3. Catalyst-embedded Hierarchical Air Electrode	
3.1 Introduction	44
3.2 Experimental Details	47
3.3 Results and Discussion	
3.3.1 Pt-loaded CNT fibril electrode	49
3.3.2 The origin of the enhanced cycle stability.....	52

3.4	Conclusion.....	56
3.5	References	70
Chapter 4. Soluble Catalyst for Efficient Li Air Battery		
4.1	Introduction.....	74
4.2	Experimental Details.....	78
4.3	Results and Discussion	
4.3.1	Redox mediator and air-electrode architecture.....	80
4.3.2	Electrochemical performances of the Li-O ₂ cell	81
4.3.3	Reversibility and the redox mediator	85
4.4	Conclusion.....	89
4.5	References	99
Chapter 5. Li-O₂/CO₂ battery		
5.1	Introduction.....	102
5.2	Experimental Details	
5.2.1	Computational details.....	105
5.2.2	Experimental details.....	106
5.3	Results and Discussion	
5.3.1	Calculations for the reaction pathways	108
5.3.2	Experimental demonstrations for Li-O ₂ /CO ₂ cells.....	116
5.4	Conclusion.....	123
5.5	References	144
Chapter 6. Li-SO₂ battery		
6.1	Introduction.....	148
6.2	Experimental Details	
6.2.1	Preparation of Li-SO ₂ cells.....	151
6.2.2	Electrochemical characterization and analyses	151

6.3	Results and Discussion	
6.3.1	Working principles and properties of Li-SO ₂ battery	153
6.3.2	Rechargeability of Li-SO ₂ battery	155
6.3.3	Catalyst for efficient Li-SO ₂ battery.....	156
6.4	Conclusion.....	161
6.5	References	169
	Abstract in Korean.....	172

List of Figures

Figure 2-1. SEM images of the CNT fibril at low magnification and high magnification.

Figure 2-2. Discharge/charge profiles of the Li-O₂ cells using an air electrode based on a woven CNT, Ketjen black, and CNT powder.

Figure 2-3. Discharge/charge profiles and cyclability of Li-O₂ cells using an air electrode based on a woven CNT.

Figure 2-4. SEM and TEM images of the CNT fibril electrode during electrochemical test.

Figure 2-5. Electron diffraction patterns of an as-prepared electrode and the electrode after the first discharge.

Figure 2-6. EDS mapping of the CNT string after the first discharge.

Figure 2-7. SEM images of the air electrode based on a woven CNT after 100 cycles at various magnifications.

Figure 3-1. SEM and TEM images at various magnifications of the CNT electrodes before Pt coating and after Pt coating.

Figure 3-2. SEM images of the Pt/CNT electrode.

Figure 3-3. Additional TEM images of the Pt/CNT electrode at various magnifications.

Figure 3-4. TEM image of a single string of Pt/CNT at a high magnification and the EDS line map of Pt.

Figure 3-5. Electrochemical profiles of the CNT and Pt/CNT electrodes.

Figure 3-6. Time vs. voltage and current profiles of the first 10 cycles for the Pt/CNT electrode.

Figure 3-7. Discharge/charge profiles of the Pt/CNT electrode at 2000 mA g⁻¹ with full discharge/charge between 2.0–4.5 V.

Figure 3-8. Cyclability of the Li-O₂ cell with a Pt/CNT electrode at a current rate of 2,000 mA g⁻¹.

Figure 3-9. TEM images of the Pt/CNT electrode after the first discharge to 1,000 mAh g⁻¹ and after full discharge to 2.0 V.

Figure 3-10. Various TEM images of the Pt/CNT electrode after the first charge.

Figure 3-11. GITT voltage profiles of the Pt/CNT electrode.

Figure 3-12. SEM images at various magnifications of the CNT electrode without catalyst and the Pt/CNT electrode after the first discharge to 2.0 V.

Figure 3-13. SEM images at various magnifications of the CNT electrode without catalyst and the Pt/CNT electrode at the end of cycles.

Figure 4-1. Scheme of the combination of the redox mediator and air-electrode architecture.

Figure 4-2. SEM images of the CNT fibril electrode at various magnifications.

Figure 4-3. Electrochemical performances of Li-O₂ cells with the LiI catalyst.

Figure 4-4. Cyclability of the CNT fibril electrodes without a catalyst and with the Pt catalyst.

Figure 4-5. Electrochemical properties of a Li-O₂ cell using a Ketjen black electrode without a catalyst and with the LiI catalyst.

Figure 4-6. Electrochemical analysis of Li-O₂ cells in the presence of a LiI catalyst.

Figure 4-7. Characterizations for the reversibility of Li-O₂ cells using the LiI catalyst.

Figure 4-8. Discharge/charge profiles of a Li-O₂ cell using a dual-electrolyte system.

Figure 4-9. TEM image of the air-electrode at the end of the cycles.

Figure 5-1. Binding energy trend of relaxed coordinate scan between O_2^- and Li^+ under Poisson-Boltzmann solvation model.

Figure 5-2. Structures of chemical species which are derived by initial reaction step with O_2^- ; $O_2^- + Li^+ \rightarrow LiO_2$, $O_2^- + CO_2 \rightarrow CO_4^-$, transition and decomposed state of EC, DMSO and DME.

Figure 5-3. Activation barrier and binding reaction energy from DFT calculations during which O_2^- is coordinating with Li^+ , CO_2 and electrolyte.

Figure 5-4. DFT predicted trend of activation barrier and binding reaction energy plotted against $[\text{dielectric constant}]^{-1}$ for the *initial complex formation (ICF)* steps of forming LiO_2 and CO_4^- .

Figure 5-5. DFT relative energy changes from LiO_2 to Li_2O_2 for three possible reaction pathways using DMSO and DME electrolytes.

Figure 5-6. Two-dimensional energy surface map including every possible intermediate species from the dioxygen anion radical of O_2^- (formed after ORR reaction) to $(Li_2O_2)_1$ and $(Li_2CO_3)_2$ using DME and DMSO electrolytes.

Figure 5-7. Detailed structures of dissociation process from $C_2O_6^{2-}$ to $(CO_3^{2-} \cdots CO_3^{2-})$ by reduction under DMSO implicit solvation model.

Figure 5-8. Reduction processes which include Li^+ effect from $C_2O_6^{2-}$ to $C_2O_6^{4-}$ under DMSO implicit solvation model.

Figure 5-9. Electrochemical properties, SEM images, and XRD results of a Li- O_2 cell and a Li- O_2/CO_2 cell with DMSO electrolyte.

Figure 5-10. GITT discharge voltage profile obtained for a Li- O_2 cell and a Li- O_2/CO_2 cell with DMSO electrolyte (inset: the potential vs. time plot).

Figure 5-11. Electrochemical properties, SEM images, and XRD results of a Li- O_2 cell and a Li- O_2/CO_2 cell with DME electrolyte.

Figure 5-12. Electrochemical properties and XRD results of Li- O_2/CO_2 cells with DMSO electrolyte and DME electrolyte at a 9:1 pressure ratio of O_2 and CO_2 .

Figure 5-13. The first discharge/charge profiles and the XRD patterns after discharge and charge of the Li- O_2/CO_2 cell with DMSO electrolyte.

Figure 6-1. Schematic illustration of the concept of a rechargeable Li-SO₂ battery during discharge and charge and comparison of the electrochemical profiles of Li-O₂ and Li-SO₂ batteries.

Figure 6-2. *Ex-situ* XRD and SEM analysis of a Li-SO₂ battery at each step.

Figure 6-3. SEM images of cathode at low magnification after the first discharge and after re-charge.

Figure 6-4. Comparison of the electrochemical profiles of the Li-SO₂ cell without and with a catalyst. XRD results of the Li-SO₂ cell using a catalyst and *In-situ* DEMS result.

Figure 6-5. The cyclability of a Li-SO₂ battery at a constant current rate of 0.2 mA/cm² between 2.0–4.2 V.

Figure 6-6. XRD pattern of the cathode after cycling. XPS spectra of S 2p: after re-charge, and at the end of cycling.

Figure 6-7. XPS spectra of S 2p after the first discharge.

List of Table

Table 5-1. Physical properties of selected electrolyte

Table 5-2. Most probable reaction pathway for Li_2CO_3 formation using DMSO electrolyte, as determined from DFT calculations

Table 5-3. Most probable reaction pathway for Li_2CO_3 formation using DME electrolyte, as determined from DFT calculations

Table 5-4. Most probable reaction pathway for Li_2O_2 formation using DMSO and DME electrolytes

Chapter 1. Introduction

1.1. Research Background

A great deal of attention for large-scale energy storage have led to increasing research interest in developing high-performance energy storage devices.¹⁻⁵ The current prevailing lithium-ion battery (LIB) has been widely used for portable devices; however, the energy density is still insufficient for large-scale applications such as smart grids or electric vehicles. To overcome the limitations of current state of LIB technology, there is significant interest in the development of next-generation batteries, or so-called post-LIB batteries.

Among several candidates for post-LIBs, enormous attention has been especially focused on Li-O₂ batteries in the hope that they could dramatically increase the energy density suitable for electric vehicles.^{6,7} In Li-O₂ batteries, there are no crystal framework or heavy transition metals to store Li ions, which lead to a substantially higher energy density (~3,500 Wh kg⁻¹).^{8,9} Li-O₂ batteries could theoretically deliver higher energy density than any other types of conventional batteries. Furthermore, the use of an unlimited source of oxygen from ambient air makes it more attractive. The electrochemical reaction mechanism between Li ion and O₂ is quite simple. One molecule of

O₂ from the air reacts with two Li ions ($\text{Li}^+ + \text{O}_2 + \text{e}^- \rightleftharpoons \text{Li}_2\text{O}_2$, 2.96 V).^{6,10}

Despite their high energy density, its range of practical application is thus far significantly restricted due to its unacceptably low cyclability and energy efficiency. These drawbacks are attributable to the formation of non-conductive discharge products. The discharge product of Li₂O₂ (lithium peroxide) continuously accumulates on the pores of electrode during discharge and could clog this electrode, preventing further reactions.^{11,12} This is the major reason for the poor efficiency and low cyclability of Li-O₂ battery. The reaction requires a substrate with highly conductive and large surface to accommodate the non-conductive solid discharge products. Therefore, a choice of appropriate substrate materials to accommodate discharge products is a key factor to determine the electrochemical properties of Li-O₂ cells.

Since the first Li-air batteries were reported by Abraham and Jiang,¹³ many researchers have utilized porous carbon substrates such as Ketjen black, Super P, and CNTs to improve the electrochemical performance of Li-O₂ batteries.¹⁴⁻¹⁷ However, it was recently proved that a reactive carbon surface is easily contaminated with the reaction of Li₂O₂ by forming a byproduct of Li₂CO₃.^{18,19} Therefore, the electrode needs to be designed to minimize the undesirable clogging and promotes the electrochemical reactivity.

Developing an ideal air-electrode design is still awaited for an advanced Li-O₂ batteries.

Another important factors that affect the electrochemical performance of the Li-O₂ battery is a catalyst. An intrinsic low conductivity of Li₂O₂ are the major contributors to the high polarization and low energy efficiency of Li-O₂ batteries.²⁰⁻²² Accordingly, to decrease the large polarization, development of an appropriate catalyst lies at the heart of all Li-O₂ systems. Researchers have used solid catalyst at the early stage of Li-O₂ batteries derived from conventional oxygen evolution reaction (OER) catalysts, which have been commonly used for water-splitting fields or fuel cells.²³⁻²⁶ However, an active site between solid discharge products (Li₂O₂) and solid catalyst is limited, which leads to a low catalytic activities.

As an innovative breakthrough, soluble catalyst was recently suggested. Soluble catalysts could potentially deliver better catalytic activity than their solid counterparts.^{27,28} Unlike immobile solid catalysts, soluble catalysts easily catalyze the decomposition of the solid discharge products and can even reach to the electrically isolated particles. Accordingly, many researchers have reported several kinds of soluble catalyst such as LiI,^{10,29} tetrathiafulvalene (TTF),²⁷ tetramethylpiperidinyloxy (TEMPO),³⁰ and iron phthalocyanine (FePc)³¹ etc. Considering that conventional solid catalyst

could not effectively decrease a charge polarization, mobile soluble catalyst would be a promising candidate, which can make Li-O₂ battery feasible as a future energy-storage-device. Consequently, recent research on L-O₂ batteries has focused intensively on searching several methods that can enhance the cycle stability and energy efficiency.

1.2. References

1. M. Armand and J. M. Tarascon, *Nature*, **2008**, *451*, 652-657.
2. A. S. Arico, P. Bruce, B. Scrosati, J.-M. Tarascon and W. van Schalkwijk, *Nat. Mater.*, **2005**, *4*, 366-377.
3. X. Ji, K. T. Lee and L. F. Nazar, *Nat. Mater.*, **2009**, *8*, 500-506.
4. B. Scrosati and J. Garche, *J. Power Sources*, **2010**, *195*, 2419-2430.
5. Y. Yang, M. T. McDowell, A. Jackson, J. J. Cha, S. S. Hong and Y. Cui, *Nano Lett.*, **2010**, *10*, 1486-1491.
6. P. G. Bruce, S. A. Freunberger, L. J. Hardwick and J.-M. Tarascon, *Nat. Mater.*, **2012**, *11*, 19-29.
7. R. Black, S. H. Oh, J.-H. Lee, T. Yim, B. Adams and L. F. Nazar, *J. Am. Chem. Soc.*, **2012**, *134*, 2902-2905.
8. Z. Peng, S. A. Freunberger, L. J. Hardwick, Y. Chen, V. Giordani, F. Bardé, P. Novák, D. Graham, J.-M. Tarascon and P. G. Bruce, *Angew. Chem. Int. Ed.*, **2011**, *123*, 6475-6479.
9. Y.-C. Lu, H. A. Gasteiger and Y. Shao-Horn, *J. Am. Chem. Soc.*, **2011**, *133*, 19048-19051.
10. H.-D. Lim, H. Song, J. Kim, H. Gwon, Y. Bae, K.-Y. Park, J. Hong, H. Kim, T. Kim, Y.H. Kim, X. Lepró, R. Ovalle-Robles, R.H. Baughman and K. Kang, *Angew. Chem., Int. Ed.*, **2014**, *53*, 3926-3931.
11. S. S. Zhang, X. Ren and J. Read, *Electrochim. Acta*, **2011**, *56*, 4544-4548.
12. D. Zheng, H.-S. Lee, X.-Q. Yang and D. Qu, *Electrochem. Commun.*, **2013**, *28*, 17-19.

13. K. M. Abraham and Z. Jiang, *J. Electrochem. Soc.*, 1996, **143**, 1-5.
14. H.-D. Lim, K.-Y. Park, H. Song, E. Y. Jang, H. Gwon, J. Kim, Y. H. Kim, M. D. Lima, R. O. Robles, X. Lepró, R. H. Baughman and K. Kang, *Adv. Mater.*, **2013**, *25*, 1348-1352.
15. C. S. Park, K. S. Kim and Y. J. Park, *J. Power Sources*, **2013**, *244*, 72-79.
16. Y. Li, J. Wang, X. Li, D. Geng, R. Li and X. Sun, *Chem. Commun.*, **2011**, *47*, 9438-9440.
17. J. Read, *J. Electrochem. Soc.*, **2002**, *149*, A1190-A1195.
18. M. M. Ottakam Thotiyl, S. A. Freunberger, Z. Peng and P. G. Bruce, *J. Am. Chem. Soc.*, **2012**, *135*, 494-500.
19. B. D. McCloskey, A. Speidel, R. Scheffler, D. C. Miller, V. Viswanathan, J. S. Hummelshøj, J. K. Nørskov and A. C. Luntz, *J. Phys. Chem. Lett.*, **2012**, *3*, 997-1001.
20. S. Liu, Z. Wang, C. Yu, Z. Zhao, X. Fan, Z. Ling, J. Qiu, *J. Mater. Chem. A*, **2013**, *1*, 12033-12037.
21. Y. Zhu, S. Liu, C. Jin, S. Bie, R. Yang, J. Wu, *J. Mater. Chem. A*, **2015**, *3*, 13563-13567.
22. R. Black, B. Adams, L. F. Nazar, *Adv. Energy Mater.*, **2012**, *2*, 801-815.
23. J. Suntivich, H. A. Gasteiger, N. Yabuuchi, H. Nakanishi, J. B. Goodenough, Y. Shao-Horn, *Nat. Chem.*, **2011**, *3*, 546-550.
24. Y.-C. Lu, Z. Xu, H. A. Gasteiger, S. Chen, K. Hamad-Schifferli, Y. Shao-Horn, *J. Am. Chem. Soc.*, **2010**, *132*, 12170-12171.
25. Z. Peng, S. A. Freunberger, Y. Chen, P. G. Bruce, *Science*, **2012**, *337*, 563-566.

26. W.-H. Ryu, T.-H. Yoon, S. H. Song, S. Jeon, Y.-J. Park, I.-D. Kim, *Nano Lett.*, **2013**, *13*, 4190-4197.
27. Y. Chen, S. A. Freunberger, Z. Peng, O. Fontaine, P. G. Bruce, *Nat. Chem.*, **2013**, *5*, 489-494.
28. T. Shiga, Y. Hase, Y. Kato, M. Inoue, K. Takechi, *Chem. Commun.*, **2013**, *49*, 9152-9154.
29. M. Yu, X. Ren, L. Ma, Y. Wu, *Nat. Commun.*, **2014**, *5*, 5111.
30. B. J. Bergner, A. Schürmann, K. Pepler, A. Garsuch, J. Janek, *J. Am. Chem. Soc.*, **2014**, *136*, 15054-15064.
31. D. Sun, Y. Shen, W. Zhang, L. Yu, Z. Yi, W. Yin, D. Wang, Y. Huang, J. Wang, D. Wang, J. B. Goodenough, *J. Am. Chem. Soc.*, **2014**, *136*, 8941-8946.

Chapter 2. Cathode Design for Reversible Li Air Battery

(The contents of this chapter has been published in *Advanced Materials*.

Reprinted from [H.-D. Lim *et al.*, *Adv. Mater.*, **2013**, *25*, 1348-1352]

Copyright 2013 WILEY-VCH)

2.1. Introduction

With increasing demand for ultra-high-energy-density storage systems, considerable effort has been recently focused on Li-O₂ batteries.¹⁻⁴ The Li-O₂ battery can deliver substantially higher energy density (~3,500 Wh kg⁻¹) than conventional Li-ion batteries.^{4,5} However, such key limitations, including poor cyclability, low Coulombic efficiency, and relatively low capacity must be resolved for the Li-O₂ battery to be considered for applications.

Recent studies have shown that identifying a stable electrolyte is critically important for increasing the cycle life of Li-O₂ batteries.^{6,7} Conventional carbonate-based electrolyte easily deteriorates upon attack of reactive oxygen radicals.^{6,8} Even non-carbonate-based electrolytes, such as

tetraethylene glycol dimethylether (TEGDME) and dimethoxyethane (DME), are not stable, and cannot sufficiently improve the cycle life.^{7,9} Another important measure to improve rechargeability is to enhance reaction kinetics for the formation and decomposition of Li_2O_2 by designing a nanostructured air electrode. Because the discharge product, Li_2O_2 , continuously accumulates on the pores of an air electrode, it can potentially clog this electrode and become electrically disconnected, preventing further reactions. These isolated discharge products undergo minimal recharging. Therefore, the air electrode needs to be designed such that it minimizes the undesirable clogging and promotes the electrochemical reactivity. As the control of the morphology and porosity of the electrode greatly affects on the capacity and rate capability,¹⁰ various nanostructured air electrodes have been reported using carbon nanoparticles, graphene, graphene oxide, or carbon nanotubes (CNTs).¹¹⁻¹⁴ However, the poor cyclability and low rate capability remain as critical drawbacks of the Li-O_2 batteries, and the ideally designed electrode architecture is still awaited.

We here show that a hierarchical porous electrodes comprising well-aligned CNTs fibrils can serve as an important model for controlled porosity and demonstrate that they can significantly enhance the cycle stability and rate capability of the Li-O_2 batteries. The controlled porous framework of these

woven CNT electrodes enables effective formation/decomposition of lithium peroxide by providing facile accessibility of oxygen to the inner side of the air electrode and preventing the clogging of pores by discharge product, even during the deep discharge. We found that the discharge products were uniformly deposited on the individual CNTs and CNT bundles, so pores are not clogged. This unique feature led to the high cycle life and unprecedentedly high rate performance of the Li-O₂ cell. We believe that the facile controllability of porous morphology using well-aligned CNT fibrils can provide an important tool in identifying an ideally designed air electrode.

2.2. Experimental Details

An individual sheet of the highly oriented CNT fibril was fabricated from dense carbon forests which was synthesized by catalytic chemical vapor deposition using acetylene gas as the carbon source.¹⁵ Air electrodes were prepared with 10 sheets of the CNT fibril on a Ni-mesh current collector (1/2 in. diameter). No binder, catalyst, or additional conductive carbon was used; therefore, no organic solvent or heat process was needed for the fabrication of the air electrodes. The total weight of the CNT was approximately 0.015 mg, similar to the weights of other types of carbon electrodes used as a reference for comparison. The areal density of the aligned CNT fibrils on the Ni-mesh was 0.016 mg cm⁻². The electrochemical properties were measured using a potentiogalvanostat (WonA Tech, WBCS 3000, Korea) in a pure oxygen atmosphere of 770 Torr, which was maintained by an automated throttle valve. The discharge/charge was done within the voltage range of 2.0 - 4.7 V at a current rate of 2,000 mA g⁻¹ which corresponded to ~0.032 mA cm⁻² of current density. The specific capacities were described in terms of “per gram of active carbon weight” (CNT sheets, Ketjen black, or CNT powder).

2.3. Results and Discussion

2.3.1. Fabrication of well-aligned CNT fibril sheets

The air electrode with controlled pore structure was fabricated by orthogonally plying individual sheets of aligned multiwalled nanotubes (MWNTs) without use of any binder or solvent. These MWNT sheets, which are drawn from specially prepared ~400 μm high carbon nanotube forests, are initially an aerogel having about the density of air and a greater gravimetric strength in the nanotube orientation direction than the strongest steel.¹⁵

Figure 2-1 shows SEM images of the prepared air electrode. Well-aligned CNT fibril sheets were woven like a mesh structure. One layer of the CNT fibril sheet was composed of a number of micro-sized strings. An individual string is a bundle of multiwall CNTs, ~15 nm in diameter (Figure 2-1b). The inset in Figure 2-1a shows that these well-ordered structures are maintained over a large area.

Highly aligned, self-woven sheets were used as an electrode for the Li-O₂ cell. The air electrodes were prepared by orthogonally plying sheets of the CNT fibril on a Ni-mesh current collector. The electrolyte consisted of 0.21 ml of TEGDME with 1M LiPF₆. Before the test, the air electrode and

separator were soaked in the electrolyte to ensure wetting of the electrolyte. Lithium metal (3/8 in. diameter), a glass fiber separator (Whatman GF/D microfiber filter paper, 2.7 μm pore size), and the air electrode were assembled into Swagelok cells.

2.3.2. Electrochemical properties

Figure 2-2a shows the galvanostatic charge/discharge profiles of the cell with the woven CNT air electrode. A discharge capacity of $\sim 2,500 \text{ mAh g}^{-1}$ could be delivered with comparable charge capacity. The electrochemical profile did not change significantly over cycles without increasing the polarization. The stable formation/decomposition cycles successfully continued with high Coulombic efficiency, for up to 20 cycles (Figure 2-2b). This cycle performance represents a dramatic enhancement over conventional air electrodes, as shown in Figure 2-2a. The Ketjen black air electrode, which has been typically used for Li-O₂ batteries (Figure 2-2c and 2-2d),^{16,17} can deliver reasonably high first-discharge capacity; however, the capacity decays rapidly after only a few cycles, consistent with previous works.^{9, 18} The fast capacity decay is accompanied by a significant increase in the polarization, mainly attributed to the rise in the electrode resistance. We ascribe the increase in the electrode resistance to the accumulation of

discharge products and its incomplete decomposition during cycles. The same amount of carbon and electrolyte was used in our comparisons. Furthermore, we tested Li-O₂ cells using an air electrode based on randomly stacked CNT powder (Figure 2-2e and 2-2f). Even though the rechargeability was slightly improved, compared with the Ketjen black air electrode, it was significantly inferior to that of the Li-O₂ cell based on the woven CNT air electrode.

The enhanced cyclability of the woven CNT air electrode is quite notable in two aspects. First, the cycling was done with a deep discharge. Typically, a deep discharge to 2 V substantially increases the resistance of the electrode, and subsequent charging causes severe polarization, resulting in a limited cycle life.⁹ Recent studies have shown that restricting the charge/discharge voltage or capacity can enhance the cycle performance by avoiding the deep discharge state.¹⁹⁻²² However, it should be stressed that no such restrictions were applied in this case. As a comparative experiment, we confirmed that cycling with a limited capacity (1,000 mAh g⁻¹) further enhanced the cycle performance. The cycle performance in Figure 2-3 paralleled the best cycle data published so far¹⁹ at higher current rates of 1,000 mA g⁻¹ (Figure 2-3a and 2-3b) and 2,000 mA g⁻¹ (Figure 2-3c and 2-3d), which once again demonstrated the superiority of the woven CNT air electrode. Second, for a

Li-O₂ cell, the enhanced cyclability of the woven CNT air electrode was notable in that it could operate reversibly, even at an exceptionally high current density. While conventional Li-air batteries have been operated at relatively low current rates (~50-200 mA g⁻¹),^{3,11,23} the current density applied here was at least ten times higher (2,000 mA g⁻¹).

2.3.3. The origin of the enhanced performances

The enhanced electrochemical properties are attributed to the unique open framework of the woven CNT sheets array. The woven fibrils with well-aligned CNTs ensured a highly porous framework, which allowed the oxygen to easily access the inner space of the electrode. The hierarchical porous structure prevented the clogging of the discharge products and promoted the surface reaction of the formation/decomposition of Li₂O₂ on the CNT. This suggests that the high mechanical flexibility and electrical conductivity of the woven CNT¹⁵ contributed to the enhanced performance. The growth of discharge products in the pores of the electrode during cycles could expand the pore volume, which would result in the deterioration of the pore structure or, moreover, the isolation of individual carbon nanoparticles in the conventional air electrode. In contrast, the durability of the woven structure of the CNT fibrils was stable, even for large changes in the volume.

The overall framework of the CNT fibril did not change, even after 100 cycles (Figure 2-4d), as will be discussed below.

The woven CNT air electrode was analyzed after the cycles. Each CNT in the bundle was homogeneously coated with the discharge products after the discharge, as shown in Figure 2-4a. No blockage or clogging occurred, even during the deep-discharge state (Figure 2-4a and 2-4b). The TEM image in Figure 2-4c clearly indicates that a ~10-nm-thick layer of discharge products was uniformly deposited on the CNT surface (inset of the figure), which was identified to be Li_2O_2 from selected area electron diffraction (SAED) in Figure 2-5. Furthermore, energy dispersive spectroscopy (EDS) mapping of the air electrode after the first discharge indicated the formation of Li_2O_2 (Figure 2-6). It is noteworthy that the open framework of the air electrode was well maintained, even after 100 cycles (Figure 2-4d), which indicates the structural stability of the woven CNT air electrode. Additional SEM images of the electrode after 100 cycles (under various magnifications), shown in Figure 2-7, also confirmed that the porous structure of the electrode was retained. This is in clear contrast to the CNT powder electrode with random stacking, shown in Figure 2-4e. The CNT powder electrode was completely clogged after the first discharge, as shown in Figure 2-4f, which will be discussed below.

Some bead-like discharge products, 100 nm in diameter, were also observed, in addition to the uniform coating on the CNT (Figure 2-4b and 2-4c). These bead-like discharge products were more predominant in the CNT coating after 100 cycles (Figure 2-4d). This observation may provide insight into the reaction mechanism and the reason for the cycle limitation after 20 cycles. During the initial discharge process, the formation of Li_2O_2 occurred first on the fresh surface of the CNT, which resulted in uniform deposition of Li_2O_2 along the CNT. However, when the discharge products were deposited over a certain critical thickness, the electron transfer from the CNT through the deposit was limited; thus, the discharge reaction occurred only locally, resulting in randomly distributed bead-like discharge products, as indicated in Figure 2-4c. These bead-like discharge products did not decompose easily during charging, due to insufficient electron transfer from the CNT, but instead remained as low-conductivity byproducts on the CNT surface. As cycling continued, the remaining bead-like discharge products increased, gradually reducing the active surface area for the reaction, which led to a decay in the capacity. We speculate that the prevention of localized discharge product formation is important in further improving the cycle life. Furthermore, the critical thickness of Li_2O_2 on the air electrode before bead formation needs to be studied fundamentally. Nevertheless, we believe that

the morphological capability of woven CNT to produce uniform deposition of the discharge product significantly enhanced the cycle performance compared with the random carbon structure of conventional air electrodes.

The uniform formation of discharge products on the surface of the CNT is also advantageous with regard to reaction kinetics. In typical Li-O₂, conventional carbon structures with random pores will deposit the discharge products randomly, even on undesired sites of the air electrode, which may cause partial clogging. Once clogging occurs, only the outer space of the air electrode is accessible to the oxygen atmosphere preventing a continuous accessing of oxygen to the inner sites.^{16,24} This is clearly demonstrated in Figure 2-4e and 2-4f; the randomly distributed CNT air electrode was completely clogged after the discharge, in contrast to the aligned CNT air electrode. The discharge products covered the outer electrode surface and blocked the access of oxygen, resulting in cycle degradation. However, the highly aligned open structure of the woven CNT fibril would enable the easy access of oxygen to the inner carbon; therefore, there was a larger active surface area in the CNT that could participate in the reaction, which, in turn, facilitated uniform coating of the discharge product.

2.4. Conclusion

In this work, a hierarchical carbon air electrode with controlled porosity was fabricated from well-aligned CNT fibrils. The unique porous morphology of the air electrode significantly improved the cyclability of the LiO₂ battery without a catalyst, even at an extremely high current density (2 A g⁻¹). This was attributed to the facile accessibility of oxygen to the inner side of the electrode, and the large active surface of the CNT in the hierarchically woven air electrode. While this work showed that orthogonally aligned CNT air electrode was successful in enhancing the electrochemical reactivity, various morphologies of air electrode can be realized simply by changing the weaving manner of CNT fibrils, which we believe can facilitate in identifying the ideally architected air electrode in the future.

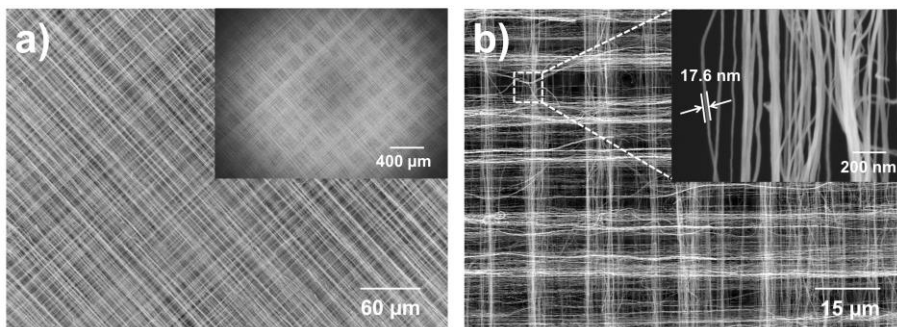


Figure 2-1. SEM images of the CNT fibril at (a) low magnification (inset: large area image of the air electrode), and (b) high magnification.

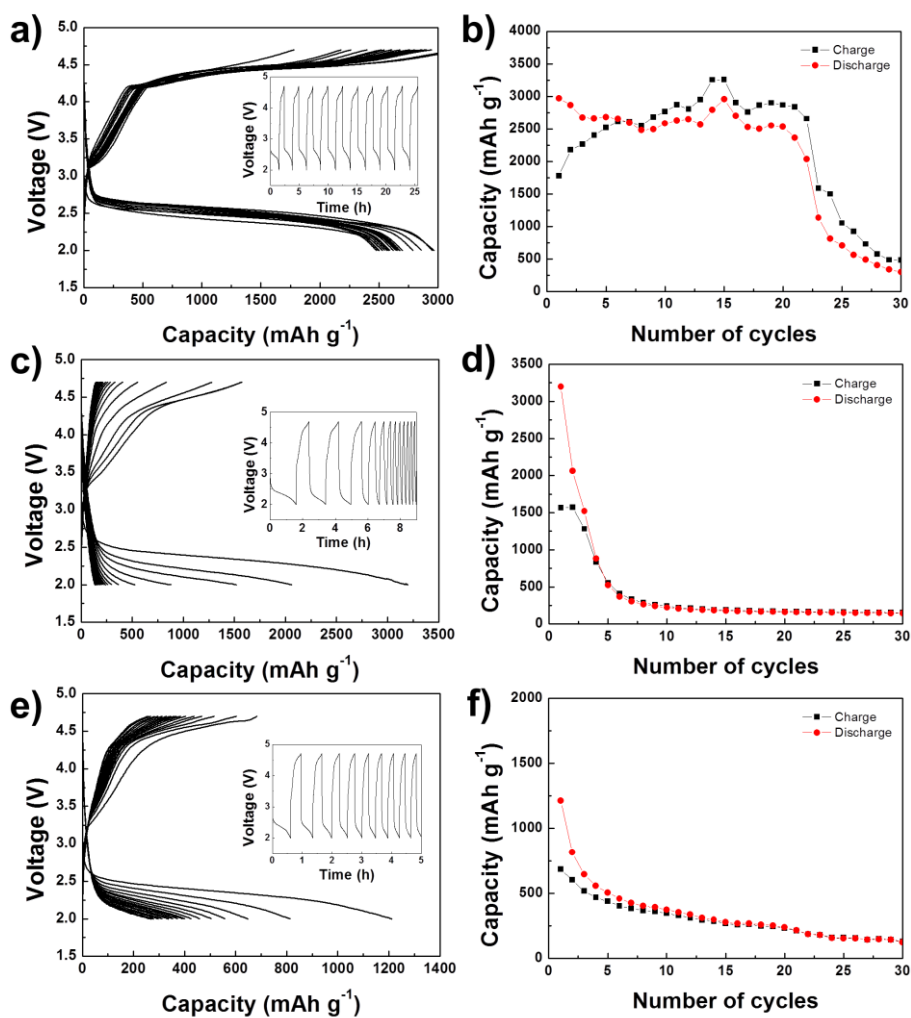


Figure 2-2. Discharge/charge profiles of the Li-O₂ cells using an air electrode based on (a) a woven CNT, (c) Ketjen black, and (e) CNT powder, for 20 cycles between 2.0 - 4.7 V at a current rate of 2,000 mA g⁻¹. The cyclability of the air electrode based on (b) a woven CNT, (d) Ketjen black, and (f) CNT powder (inset: voltage vs. time graph of the initial 10 cycles).

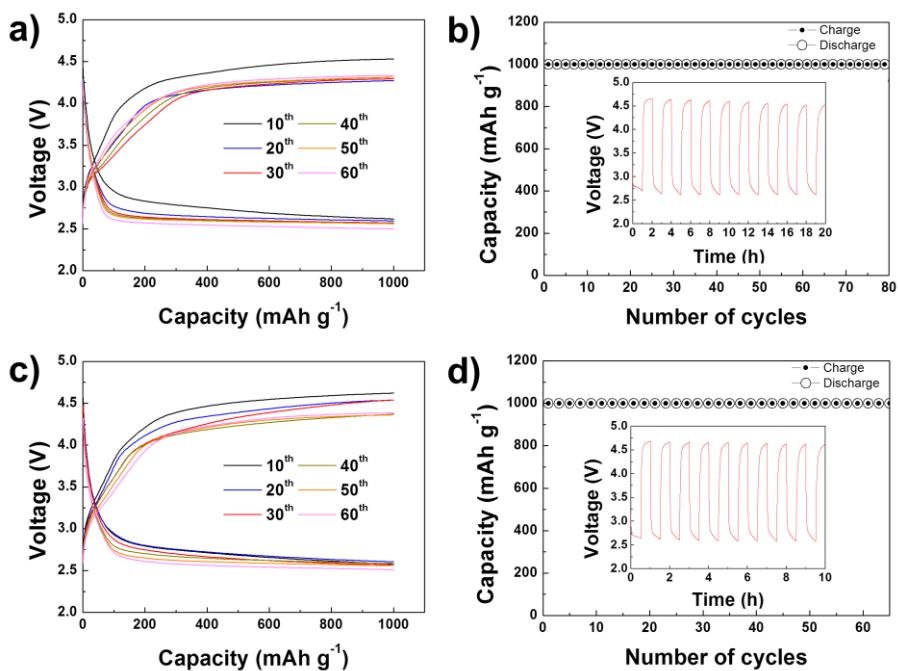


Figure 2-3. (a) Discharge/charge profiles and (b) cyclability of Li-O₂ cells using an air electrode based on a woven CNT at a current rate of 1,000 mA g⁻¹. (c) Discharge/charge profiles and (d) cyclability at a current rate of 2,000 mA g⁻¹ (inset: voltage vs. time graph of the initial 10 cycles).

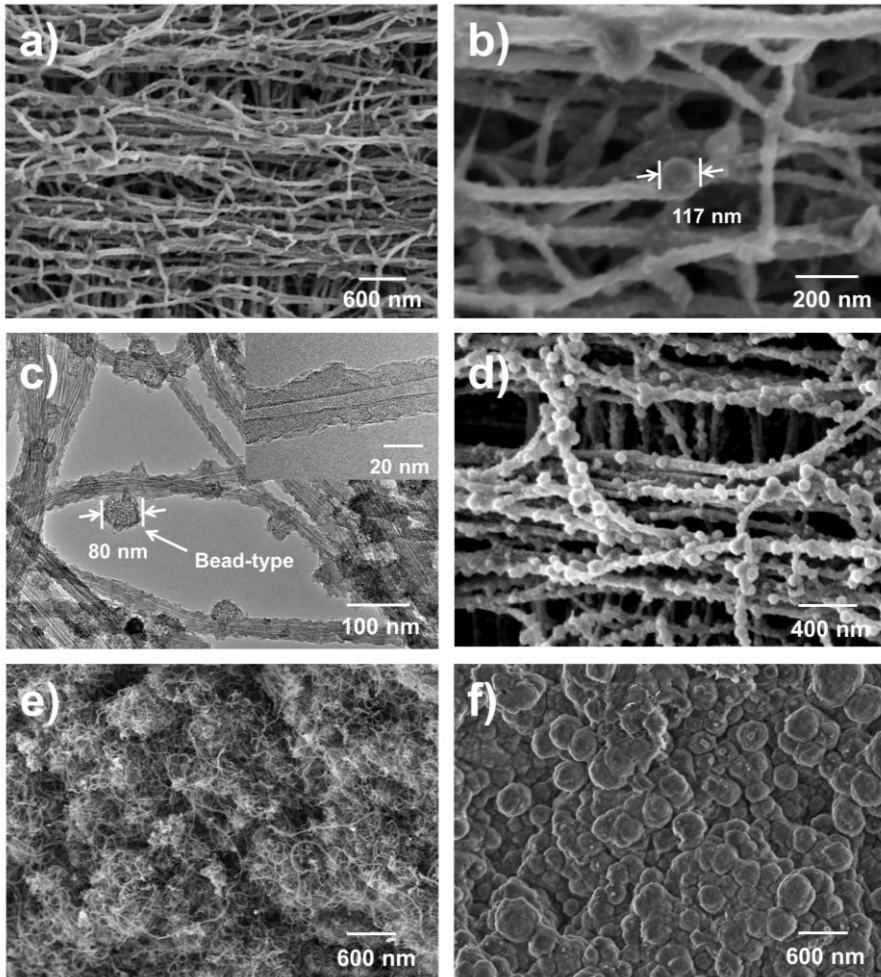


Figure 2-4. SEM images of the CNT fibril after the first discharge at (a) low magnification, and (b) high magnification. (c) TEM image of a CNT fibril after the first discharge (inset: high-magnification TEM image). (d) SEM image of the CNT fibril after 100 cycles. SEM images of normal CNT powders (e) as-prepared and (f) after the first discharge.

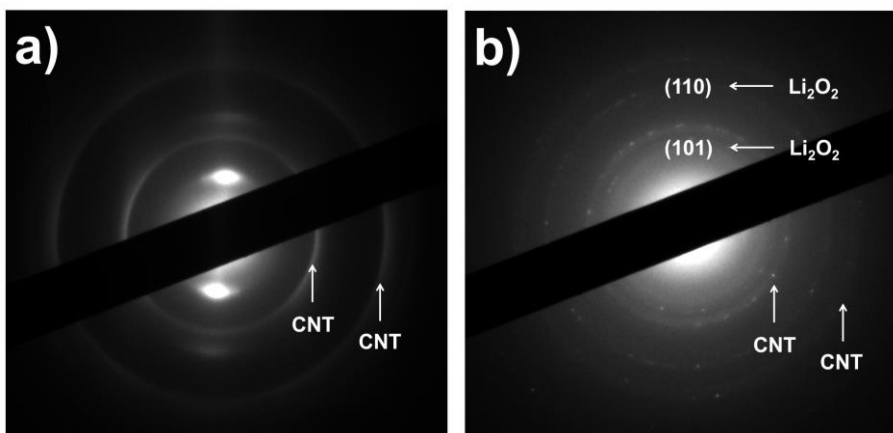


Figure 2-5. Electron diffraction patterns of (a) an as-prepared electrode and (b) the electrode after the first discharge. The formation of Li₂O₂ was detected after the discharge.

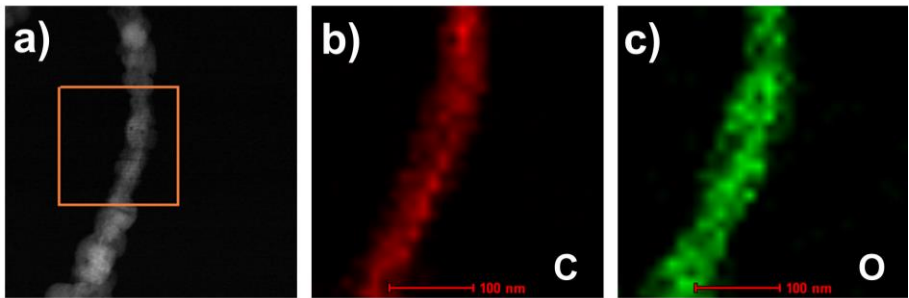


Figure 2-6. EDS mapping of the CNT string after the first discharge: (a) original TEM image, (b) carbon elemental map, and (c) oxygen elemental map. EDS mapping was used to demonstrate the uniform coating of the discharge products on the CNT surface. The oxygen elemental mapping was thicker than that of the carbon, which indicates the uniform formation of an oxide on the entire CNT surface.

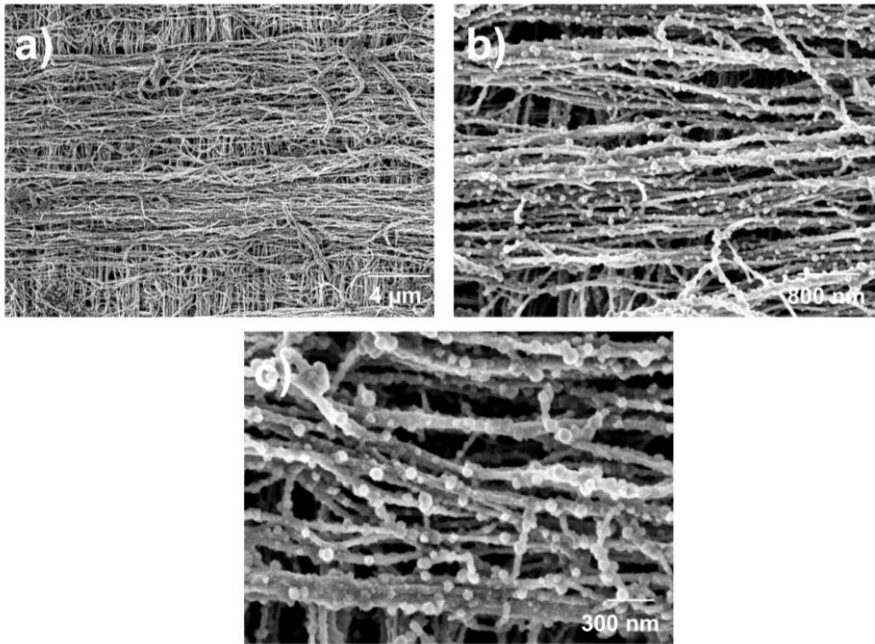


Figure 2-7. SEM images of the air electrode based on a woven CNT after 100 cycles at various magnifications. Many small beads were produced after 100 cycles. Nevertheless, it is worthwhile to note that the overall structure was maintained after many cycles.

2.5. References

1. R. Black, S. H. Oh, J.-H. Lee, T. Yim, B. Adams, L. F. Nazar, *J. Am. Chem. Soc.* **2012**, *134*, 2902.
2. Z. Peng, S. A. Freunberger, L. J. Hardwick, Y. Chen, V. Giordani, F. Bardé, P. Novák, D. Graham, J.-M. Tarascon, P. G. Bruce, *Angew. Chem.* **2011**, *123*, 6475.
3. Y.-C. Lu, H. A. Gasteiger, Y. Shao-Horn, *J. Am. Chem. Soc.* **2011**, *133*, 19048.
4. P. G. Bruce, S. A. Freunberger, L. J. Hardwick, J.-M. Tarascon, *Nat. Mater.* **2012**, *11*, 19.
5. K. M. Abraham, Z. Jiang, *J. Electrochem. Soc.* **1996**, *143*, 1.
6. B. D. McCloskey, D. S. Bethune, R. M. Shelby, G. Girishkumar, A. C. Luntz, *J. Phys. Chem. Lett.* **2011**, *2*, 1161.
7. S. A. Freunberger, Y. Chen, N. E. Drewett, L. J. Hardwick, F. Bardé, P. G. Bruce, *Angew. Chem.* **2011**, *50*, 8609.
8. S. A. Freunberger, Y. Chen, Z. Peng, J. M. Griffin, L. J. Hardwick, F. Bardé, P. Novák, P. G. Bruce, *J. Am. Chem. Soc.* **2011**, *133*, 8040.
9. C. O. Laoire, S. Mukerjee, E. J. Plichta, M. A. Hendrickson, K. M. Abraham, *J. Electrochem. Soc.* **2011**, *158*, A302.
10. M. Mirzaeian, P. J. Hall, *Electrochim. Acta* **2009**, *54*, 7444.
11. Z.-L. Wang, D. Xu, J.-J. Xu, L.-L. Zhang, X.-B. Zhang, *Adv. Funct. Mater.* **2012**, *22*, 3699.
12. Y. Li, J. Wang, X. Li, J. Liu, D. Geng, J. Yang, R. Li, X. Sun, *Electrochem. Commun.* **2011**, *13*, 668.

13. Y. Li, J. Wang, X. Li, D. Geng, R. Li, X. Sun, *Chem. Commun.* **2011**, 47, 9438.
14. X. Ren, S. S. Zhang, D. T. Tran, J. Read, *J. Mater. Chem.* **2011**, 21, 10118.
15. M. Zhang, S. Fang, A. A. Zakhidov, S. B. Lee, A. E. Aliev, C. D. Williams, K. R. Atkinson, R. H. Baughman, *Science* **2005**, 309, 1215.
16. J. Xiao, D. Wang, W. Xu, D. Wang, R. E. Williford, J. Liu, J.-G. Zhang, *J. Electrochem. Soc.* **2010**, 157, A487.
17. S. D. Beattie, D. M. Manolescu, S. L. Blair, *J. Electrochem. Soc.* **2009**, 156, A44.
18. A. Débart, J. Bao, G. Armstrong, P. G. Bruce, *J. Power Sources* **2007**, 174, 1177.
19. H.-G. Jung, J. Hassoun, J.-B. Park, Y.-K. Sun, B. Scrosati, *Nat. Chem.* **2012**, 4, 579.
20. E. Yoo, H. Zhou, *ACS Nano* **2011**, 5, 3020.
21. D. Xu, Z.-l. Wang, J.-j. Xu, L.-l. Zhang, X.-b. Zhang, *Chem. Commun.* **2012**, 48, 6948.
22. H.-D. Lim, K.-Y. Park, H. Gwon, J. Hong, H. Kim, K. Kang, *Chem. Commun.* **2012**, 48, 8374.
23. A. Débart, A. J. Paterson, J. Bao, P. G. Bruce, *Angew. Chem.* **2008**, 120, 4597.
24. S. S. Zhang, D. Foster, J. Read, *J. Power Sources* **2010**, 195, 1235.

Chapter 3. Catalyst-embedded Hierarchical Air Electrode

(The essence of this chapter has been published in *Energy & Environmental Science*. Reproduced from [H.-D. Lim, *et al.*, *Energy Environ. Sci.*, **2013**, *6*, 3570-3575] with permission from The Royal Society of Chemistry)

3.1. Introduction

Increasing demands for large-scale energy devices, such as electric vehicles (xEVs), require next-generation battery designs beyond those of the current Li-ion batteries (LIBs).¹⁻⁴ Among several candidates for post-LIBs, attention has focused on the Li-O₂ battery because of its remarkably high energy density that can reach about 3,500 Wh/kg.⁵⁻⁷ This high energy density is achievable because the electrochemical reaction between Li and O₂ in the Li-O₂ cell does not require the host crystal framework that typically includes heavy transition metals as redox elements.⁸⁻¹⁰ Moreover, the availability of an unlimited source of oxygen from ambient air makes it more attractive as a next-generation battery. However, key limitations, such as poor cyclability and low coulombic efficiency, must be resolved for the Li-O₂ battery to be

considered for extensive applications.

The major factors that affect the electrochemical performance of the Li-O₂ battery include the compatibility of the electrolyte, the electrode design, and the catalyst. At the early stages of Li-O₂ battery development, conventional LIB electrolytes, such as ethylene carbonate/dimethyl carbonate (EC/DMC) and propylene carbonate (PC), were used.¹¹⁻¹³ However, it was soon revealed that the carbonate-based electrolyte was unstable, yielding undesirable byproducts such as Li₂CO₃.^{14,15} As an alternative, non-carbonate-based electrolytes, such as dimethoxyethane (DME) and tetraethylene glycol dimethylether (TEGDME), were suggested.¹⁶⁻¹⁹ Although some improvements were achieved, they were also unstable and decomposed during prolonged cycling.²⁰ Accordingly, new reliable electrolytes for the Li-O₂ system remain elusive.^{21,22} While the electrolyte deterioration needs to be solved, the design of the air electrode is also an important factor that determines the capacity and the cycle efficiency.²³⁻²⁵ Because the solid-state discharge products are deposited and decomposed on the air electrode, the transport of reactants and the distribution of catalysts in the electrode becomes critical in the recharging process. The use of porous graphene, nanoporous gold, and perovskite nanotubes for the air electrode clearly improved the electrochemical performance of the Li-O₂ cell.²⁶⁻²⁸ More

recently, we demonstrated that the optimal design of air pathways using hierarchical carbon nanotube (CNT) fibrils with controlled porosity can significantly enhance the cycle stability. The defect-less CNT fibrils could also minimize the formation of byproduct Li_2CO_3 similar to the nanoporous gold electrode.^{29,30}

Here, we propose a new air-electrode design that incorporates catalysts in a hierarchically macroporous framework. A simple process of catalyst loading could successfully retain the optimal air pathways of the hierarchical carbon electrode and provide the right conditions for effective catalytic activity. The new electrode delivered stable cycle performance over 130 cycles with 1,000 mAh g^{-1} at a high current rate of 2 A g^{-1} . Also, even with full discharge/charge, it could sustain the high energy up to 100 cycles, which is very challenging for current Li-O_2 battery systems.

3.2. Experimental Details

A sheet of aligned multiwalled nanotubes (MWNTs) was fabricated from a CNT forest, which was synthesized by catalytic chemical vapor deposition using acetylene gas as the source. The detailed procedures for the preparation of the CNT forest and the CNT fibrils are described in previous reports.^{29,31} For the air electrode, 10 sheets of CNT fibrils were cross-woven layer-by-layer on a Ni mesh (Nillaco Corp., 12.7 mm in diameter), which was used as a current collector. There was no other conductive carbon source or binder added. The prepared CNT electrode was coated with Pt nanoparticles by DC sputtering (BAL-TEC., SCD 005). The coating time and current were maintained at 100 s and 20 mA, respectively. The Li-O₂ cells were assembled in a Swagelok-type cell by stacking the prepared air-electrodes, a glass-fiber separator (Whatman GF/D, 2.7- μ m pore size), and lithium metal in sequence. 1 M LiPF₆ in TEGDME electrolyte was used, and all the prepared cells were relaxed for 12 h in an oxygen atmosphere before testing. Electrochemical properties were measured using a potentiogalvanostat (WonA Tech, WBCS 3000, Korea). Each cell was carefully controlled and the outer pressure was maintained at oxygen atmosphere (770 Torr) using an automated throttle valve, which ensured high reproducibility

and reliability. The specific capacities were calculated based on the CNT weight. X-ray photoelectron spectroscopy (XPS, Thermo VG Scientific, Sigma Probe, UK) was used to analyze the reaction products at each step.

3.3. Results and Discussion

3.3.1. Pt-loaded CNT fibril electrode

The air electrode was constructed based on hierarchically woven CNT fibrils with micro mesh and nano-sized pores as shown in Figure 3-1. The highly aligned CNT sheets were cross-woven such that they formed a mesh, which ensured a homogenous and well-ventilated structure. The CNT fibrils were loaded with Pt nanoparticles, which was previously demonstrated as an effective catalyst for the oxygen evolution reaction (OER),³²⁻³⁷ to make the catalyst-embedded air electrode. Figure 3-1b illustrates that all of the individual CNT strings were evenly coated with the nanoparticles. The CNTs were approximately 15 nm thick, and the size of the Pt particles was about 3-4 nm. The crosslinked CNT sheet with the open framework was maintained even after the deposition of the Pt nanoparticles, which assured that all of the CNT surfaces could be used as active reaction sites. The three-dimensionally aligned pore structure of the Pt-CNT fibrils not only allowed facile accessibility for Li ions and oxygen, but also effectively exposed catalysts to the discharge products, thereby providing the ideal condition for the catalytic reaction. Additional scanning electron microscopy (SEM) and transmission electron microscopy (TEM) images of the Pt-loaded CNT fibril electrode are

given in Figures 3-2, 3-3, and 3-4. It is noteworthy that the highly aligned pore structure of the CNT sheets was advantageous in loading the nano catalyst even in the inner space of the electrode. The open aligned structure could prevent preferential deposition on the outer side of the electrode even with the one-step physical deposition method. The simple physical deposition sustained the open electrode structure, while the wet-chemical deposition often causes difficulties in maintaining the initial structure because of the capillary forces during drying. The choice of catalyst and its loading weight were easily controllable, which will be beneficial for further studies of various catalysts.

The electrochemical performance of the Pt-loaded CNT fibril (Pt/CNT fibril) electrode was evaluated in comparison with that of the catalyst-free CNT fibril electrode. Figure 3-5a shows the electrochemical profiles of the two electrodes at a current rate of $2,000 \text{ mAh g}^{-1}$ with a depth of discharge of 1000 mAh g^{-1} . The Pt/CNT fibrils clearly reduced the overpotentials by about 500 mV during charge (OER). After multiple charge and discharge cycles, lower overpotentials, compared with the bare CNT fibril electrode, were maintained (Figure 3-6). The smaller overpotential was retained even at elevated current densities. Rate capability testing of the two electrodes (Figure 3-5b) indicated that charging at $4,000 \text{ mA g}^{-1}$ still showed a lower

overpotential by about 200–300 mV than the catalyst-free electrode confirming the catalytic activity of Pt during OER. While the polarization still increased with the higher current density, the overpotential of the Pt/CNT electrode remained considerably lower. However, it was noted that the OER activity of the Pt catalyst was particularly notable at a low depth of discharge (about 1000 mAh g⁻¹). If we consider the deep discharge state to 2.0 V (about 2,500 mAh g⁻¹), the OER overpotential was not significantly reduced during the recharge even when the same catalyst was used (Figure 3-7). Because the insulating discharge products were deposited on the electrode surface, the active surface area was gradually passivated by the discharge products. In the deep discharge state, the large amount of discharge products would form a thick insulating film layer and significantly passivate the catalytic activity in terms of decomposing the products. Therefore, the catalytic activity in this case would not be as dramatic as for a low depth of discharge. Thus, in Li-O₂ batteries, the relationship between catalyst activity and the depth of discharge must be considered together.³⁸

The cycle stability of the Pt/CNT fibril electrode was evaluated (Figure 3-8). Remarkably stable cycles were achieved for capacity-limited cycling at 1000 mAh g⁻¹, which could continue over 130 cycles (Figure 3-8a). This is far superior to the bare CNT fibril electrode (the inset of Figure 3-8a), which

was stable only up to 70 cycles under the same condition. The enhanced cycling performance of Pt/CNT was observed even in the full discharge/charge cycle protocols between 2.0-4.7 V (Figure 3-8b). Compared with the bare CNT fibril electrode, which could only achieve about 30 full discharge/charge cycles²⁹, the Pt/CNT electrode had an outstanding capability for the reversible formation and decomposition of Li_2O_2 with a high efficiency. More than 100 cycles of full discharge/charge has rarely been reached by Li-O₂ batteries because of clogging of the discharge products and incomplete decomposition reactions during prolonged cycling. Although the low loading weight of the CNT sheets having the open framework is an obvious drawback for practical applications, the high reversibility of the Pt/CNT electrode even during prolonged cycling at high rates is certainly notable. It is also interesting to note that the enhanced cycle stability was achieved for full discharge/charge even though the reduction of the overpotential under the same condition was not remarkable. This discrepancy will be discussed later with respect to the nature of the deposition of the discharge products.

3.3.2. The origin of the enhanced cycle stability

To elucidate the origin of the enhanced cycle stability, the morphological

changes in the discharge products during the discharge and charge were investigated by tracing the electron microscopy images at different DODs (depths of discharge of the electrode). Figure 3-9(a-d) shows TEM and SEM images after the first discharge at DODs of 1000 mAh g⁻¹ and 2,500 mAh g⁻¹. After the first discharge at 1000 mAh g⁻¹ (Figure 3-9a and 3-9b), uniform formation of discharge products was found on the CNT surfaces. Because of the uniform growth of the discharge products, the open framework of the parent CNT sheets was well maintained without clogging (Figure 3-9). This demonstrated a high durability of the Pt/CNT electrode. With the deep discharge, the thickness of the discharge products continuously increased with continuous and uniform formation on the CNT surfaces (Figure 3-9c and 3-9d). Also, the formed discharge products were clearly decomposed after charging (Figure 3-10). This was in good agreement with the galvanostatic intermittent titration technique (GITT, Figure 3-11) data that proved the high reversibility of the Pt/CNT electrode. Interestingly, we found that the Pt catalyst strongly affected the morphologies of the discharge products. While the bare CNT fibril electrode yielded large beads about 80 nm in size after discharge (Figure 3-9e and 3-9f), the beads were not seen on the Pt/CNT electrode. Instead, simply a thicker discharge product was formed. The additional SEM images at various magnifications (Figure 3-12)

more clearly demonstrate the differences between the bare CNT and the Pt/CNT electrodes. It was previously shown that the formation of numerous large beads accompanies cycle degradation.²⁹ As the number of beads substantially increased with cycling, the beads completely covered the active CNT surfaces at the end of the cycling, resulting in the cycle failure in the case of the bare CNT electrode (Figure 3-13). The segregation of the discharge products in the form of beads can lead to electrical isolation, which can limit recharging (decomposition) upon cycling and ultimately lead to failure. With the Pt/CNT electrode, in contrast, the uniform deposition of products on the surfaces further continued without the formation of large beads even at the deep discharge states (Figures 3-9 and 3-12). We believe that the uniformly distributed nano-catalyst promoted the homogeneous film-like formation of the discharge products. Furthermore, the absence of isolated discharge products in the form of the beads could prevent the loss of active materials. This implies that the OER-enhancing Pt catalyst not only helped to reduce the charging polarization but also controlled the morphology of the discharge products, thereby contributing to the enhanced cycle stability. It is worthwhile to note that despite the insignificant reduction of overpotential with deep discharge/charge cycling, the Pt-embedded electrode maintained its higher cycle stability. This behavior is

attributed to the dual roles of the Pt OER catalyst, i.e., promoting uniform deposition of the discharge products even for deep discharged states and facilitating the decomposition reaction upon re-charging.

3.4. Conclusion

The hierarchically porous air electrode incorporating a catalyst was designed by cross-weaving aligned CNT sheets and embedding Pt nanoparticles. The ideal catalyst-embedded air electrode contributed to the facile accessibility of lithium and oxygen and provided the conditions for effective catalytic activity. The remarkable cycle stability over 100 cycles with full discharge/charge could be achieved at the high current rate of 2 A g⁻¹; this is also attributed to the dual function of the embedded Pt catalyst, which not only reduced the charge polarization substantially, but also promoted the homogeneous film-like formation of the discharge products. The design of an air electrode that considers both the transport pathway and the catalyst distribution is expected to guide further Li-O₂ battery development.

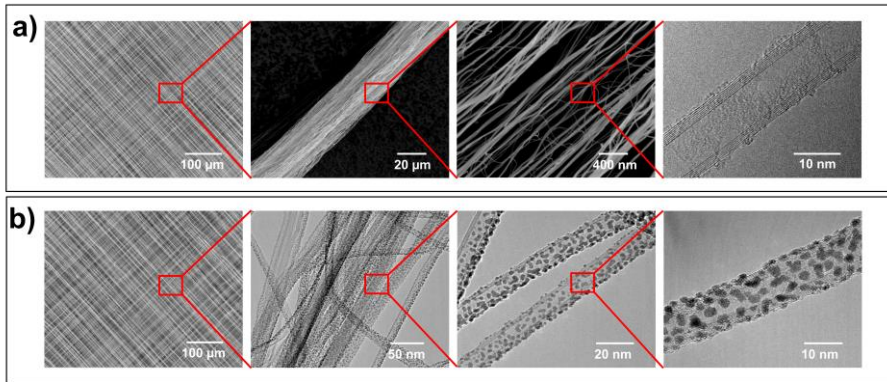


Figure 3-1. (a) SEM images at various magnifications of the CNT electrode before Pt coating and a TEM image of a single CNT. (b) SEM and TEM images at various magnifications of the Pt/CNT electrode after Pt coating.

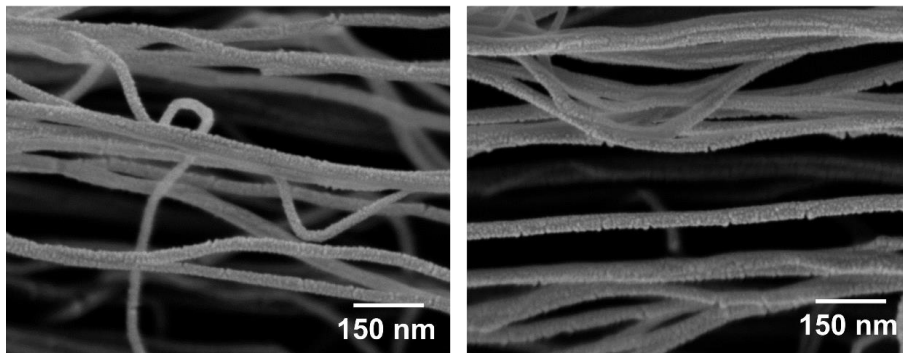


Figure 3-2. SEM images of the Pt/CNT electrode. The scabrous surface texture indicates that all of the individual CNT strings are homogenously coated with Pt nanoparticles.

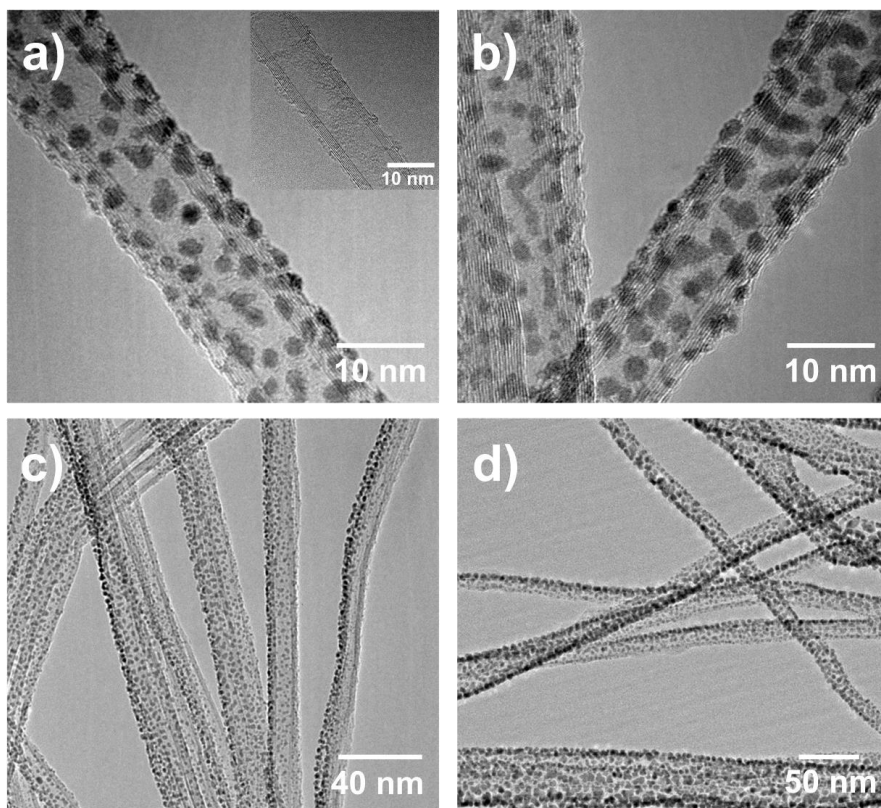


Figure 3-3. Additional TEM images of the Pt/CNT electrode at various magnifications (Inset: TEM image of the as-prepared CNT).

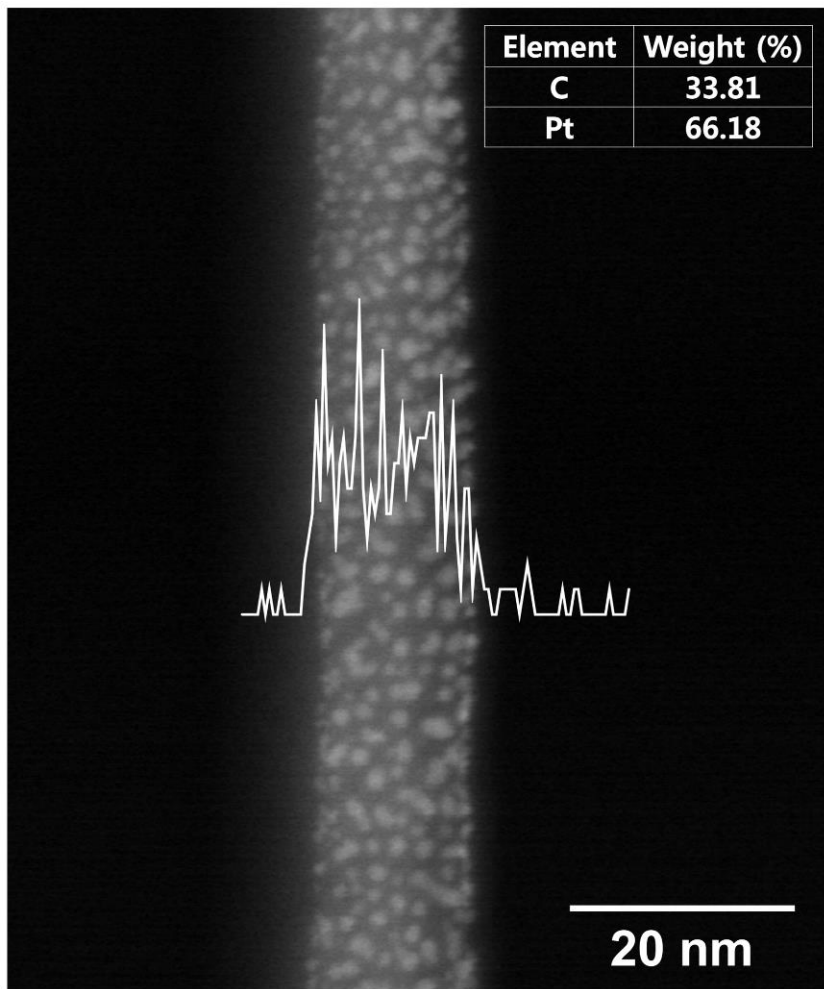


Figure 3-4. TEM image of a single string of Pt/CNT at a high magnification and the EDS line map of Pt. The inset table shows the quantitative analysis of Pt and C.

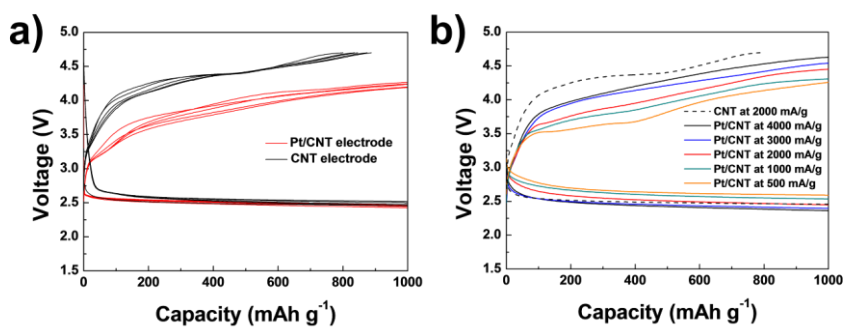


Figure 3-5. (a) Electrochemical profiles of the CNT (black line) and Pt/CNT (red line) electrodes at a current rate of 2,000 mA g⁻¹ with the limited depth of discharge at 1000 mAh g⁻¹. (b) Rate capabilities of the Pt/CNT electrode.

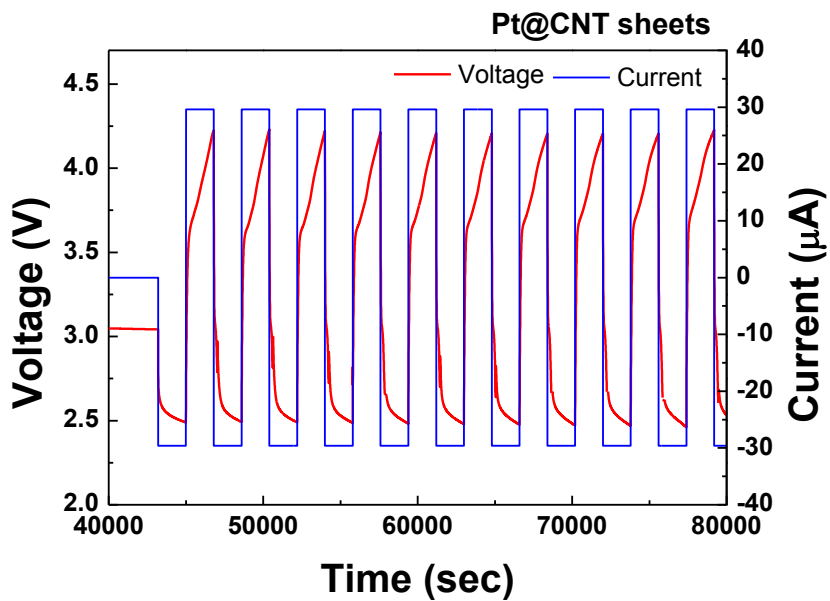


Figure 3-6. Time vs. voltage and current profiles of the first 10 cycles for the Pt/CNT electrode. Before the test, all of the cells were relaxed in an oxygen atmosphere for 12 h.

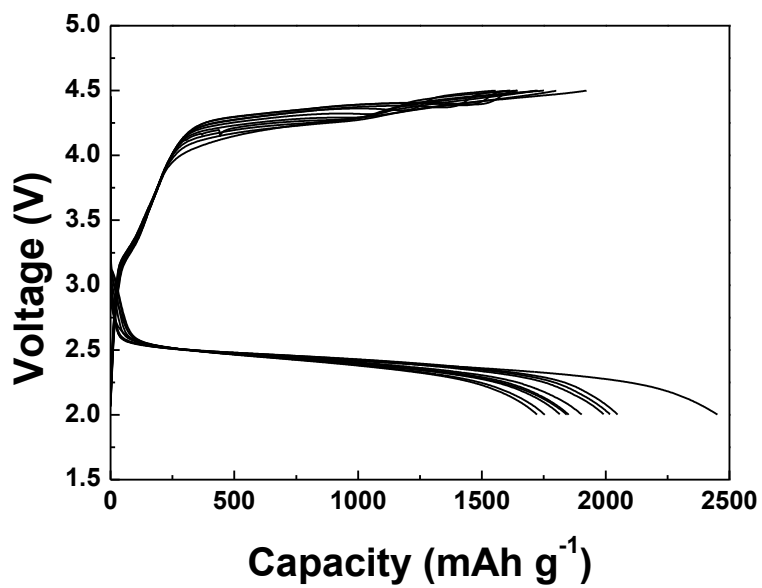


Figure 3-7. Discharge/charge profiles of the Pt/CNT electrode at 2000 mA g⁻¹ with full discharge/charge between 2.0–4.5 V.

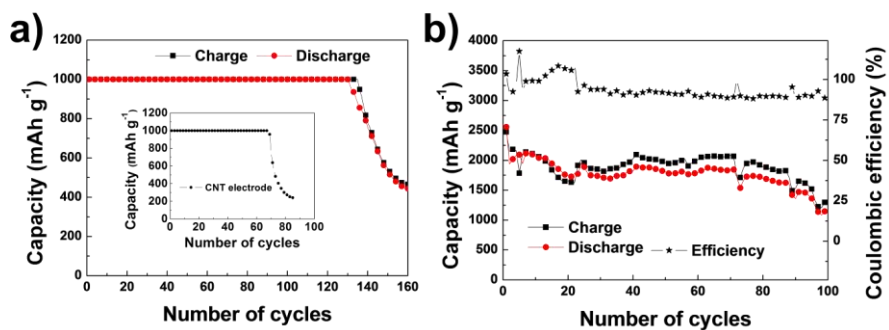


Figure 3-8. (a) Cyclability of the Li-O₂ cell with a Pt/CNT electrode at a current rate of 2,000 mA g⁻¹ with (a) the limited depth of discharge at 1000 mAh g⁻¹ and (b) fully discharged/charged between 2.0–4.7 V. (Inset: Cyclability of the Li-O₂ cell with a CNT electrode).

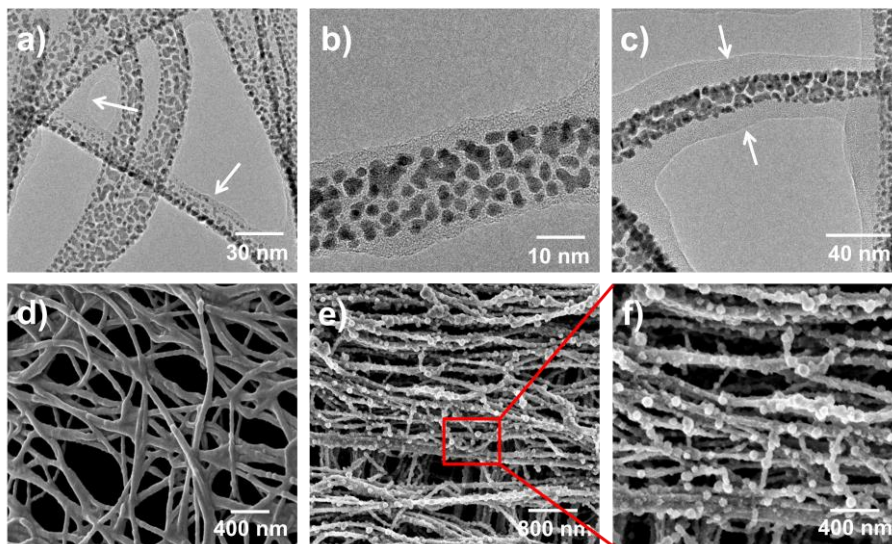


Figure 3-9. (a, b) TEM images of the Pt/CNT electrode after the first discharge to 1,000 mAh g⁻¹. (c) TEM and (d) SEM images of the Pt/CNT electrode after full discharge to 2.0 V. (e, f) SEM images of the catalyst-free CNT electrode after discharge.

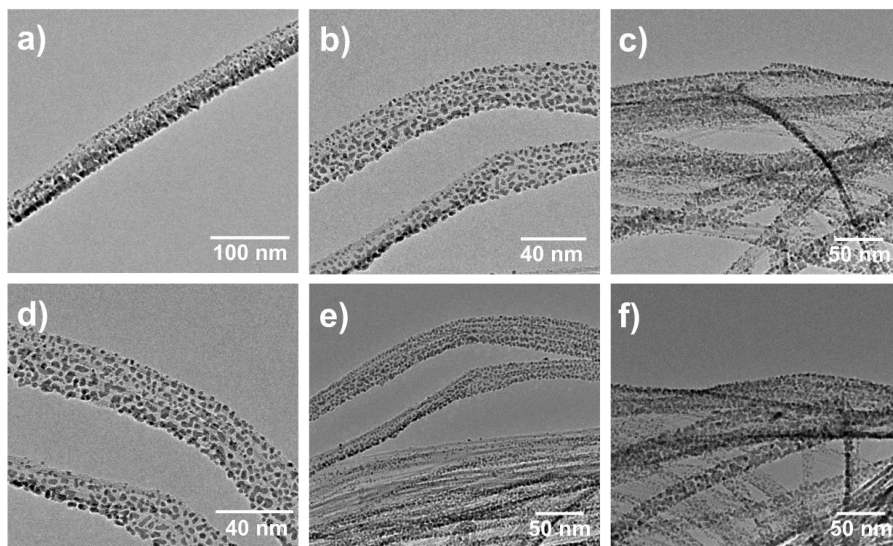


Figure 3-10. Various TEM images of the Pt/CNT electrode after the first charge. The discharge products were clearly decomposed and clean CNT surfaces were observed.

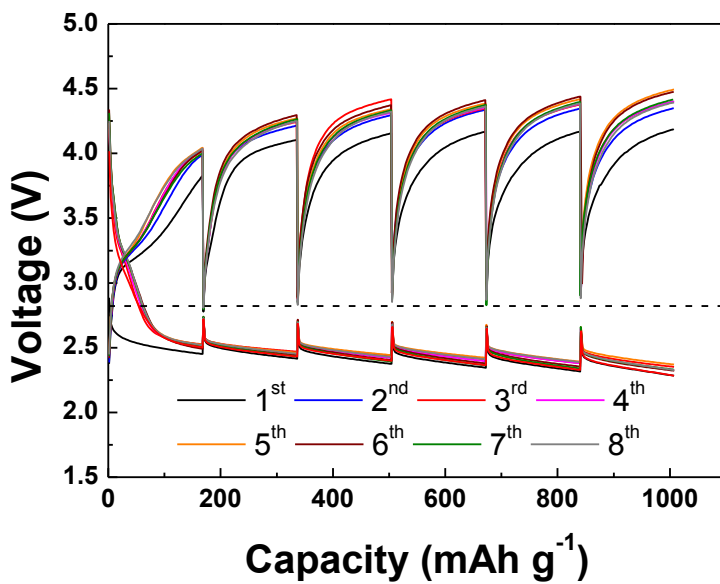


Figure 3-11. (a) GITT voltage profiles of the Pt/CNT electrode. During discharge/charge, the relaxation potential at each step approached the theoretical formation potential of Li₂O₂ (2.96 V).

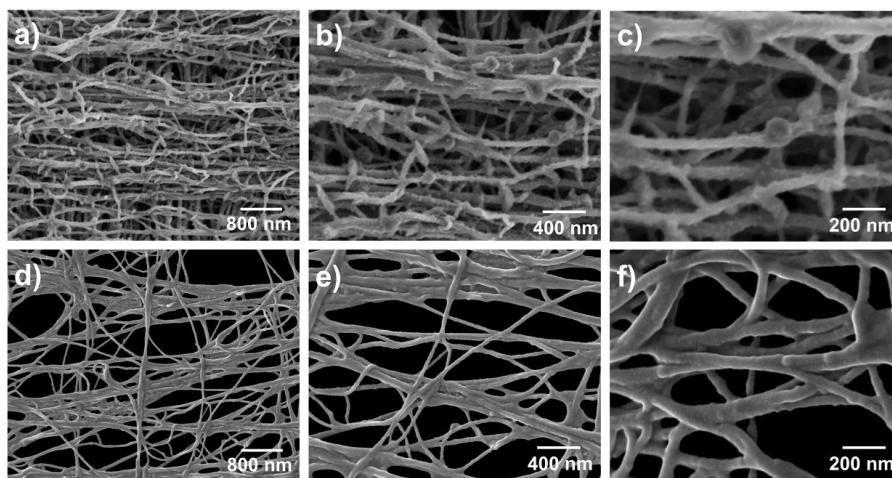


Figure 3-12. SEM images at various magnifications of (a–c) the CNT electrode without catalyst and (d–f) the Pt/CNT electrode after the first discharge to 2.0 V.

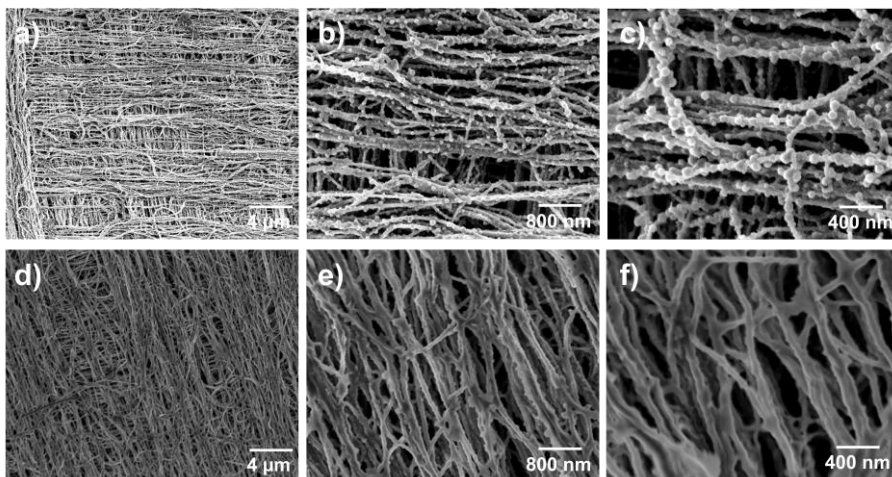


Figure 3-13. SEM images at various magnifications of (a–c) the CNT electrode without catalyst and (d–f) the Pt/CNT electrode at the end of cycles (30 and 100 cycles, respectively).

3.5. References

1. F. Cheng and J. Chen, *Nat Chem*, **2012**, *4*, 962-963.
2. P. Hartmann, C. L. Bender, M. Vračar, A. K. Dürr, A. Garsuch, J. Janek and P. Adelhelm, *Nat. Mater.*, **2012**, *12*, 228–232.
3. H.-G. Jung, J. Hassoun, J.-B. Park, Y.-K. Sun and B. Scrosati, *Nat. Chem.*, **2012**, *4*, 579-585.
4. J.-S. Lee, S. Tai Kim, R. Cao, N.-S. Choi, M. Liu, K. T. Lee and J. Cho, *Adv. Energy Mater.*, **2011**, *1*, 34-50.
5. P. G. Bruce, S. A. Freunberger, L. J. Hardwick and J.-M. Tarascon, *Nat. Mater.*, **2012**, *11*, 19-29.
6. R. Black, S. H. Oh, J.-H. Lee, T. Yim, B. Adams and L. F. Nazar, *J. Am. Chem. Soc.*, **2012**, *134*, 2902-2905.
7. Y. Cui, Z. Wen, X. Liang, Y. Lu, J. Jin, M. Wu and X. Wu, *Energy Environ. Sci.*, **2012**, *5*, 7893-7897.
8. Z. Peng, S. A. Freunberger, L. J. Hardwick, Y. Chen, V. Giordani, F. Bardé, P. Novák, D. Graham, J.-M. Tarascon and P. G. Bruce, *Angew. Chem.*, **2011**, *123*, 6475-6479.
9. A. Kraytsberg and Y. Ein-Eli, *J. Power Sources*, **2011**, *196*, 886-893.
10. J. Christensen, P. Albertus, R. S. Sanchez-Carrera, T. Lohmann, B. Kozinsky, R. Liedtke, J. Ahmed and A. Kojic, *J. Electrochem. Soc.*, **2012**, *159*, R1-R30.
11. J. Read, *J. Electrochem. Soc.*, **2002**, *149*, A1190-A1195.
12. A. Débart, A. J. Paterson, J. Bao and P. G. Bruce, *Angew. Chem.*, **2008**, *120*, 4597-4600.
13. S. D. Beattie, D. M. Manolescu and S. L. Blair, *J. Electrochem.*

Soc., **2009**, *156*, A44-A47.

14. S. A. Freunberger, Y. Chen, Z. Peng, J. M. Griffin, L. J. Hardwick, F. Bardé, P. Novák and P. G. Bruce, *J. Am. Chem. Soc.*, **2011**, *133*, 8040-8047.
15. Z. Zhang, J. Lu, R. S. Assary, P. Du, H. H. Wang, Y. K. Sun, Y. Qin, K. C. Lau, J. Greeley, P. C. Redfern, H. Iddir, L. A. Curtiss and K. Amine, *J. Phys. Chem. C*, **2011**, *115*, 25535-25542.
16. B. D. McCloskey, D. S. Bethune, R. M. Shelby, G. Girishkumar and A. C. Luntz, *J. Phys. Chem. Lett.*, **2011**, *2*, 1161-1166.
17. C. O. Laoire, S. Mukerjee, E. J. Plichta, M. A. Hendrickson and K. M. Abraham, *J. Electrochem. Soc.*, **2011**, *158*, A302-A308.
18. F. Li, T. Zhang, Y. Yamada, A. Yamada and H. Zhou, *Adv. Energy Mater.*, **2013**, *3*, 532-538.
19. C. S. Park, K. S. Kim and Y. J. Park, *J. Power Sources*, **2013**, *244*, 72-79.
20. S. A. Freunberger, Y. Chen, N. E. Drewett, L. J. Hardwick, F. Bardé and P. G. Bruce, *Angew. Chem., Int. Ed.*, **2011**, *50*, 8609-8613.
21. W. Walker, V. Giordani, J. Uddin, V. S. Bryantsev, G. V. Chase and D. Addison, *J. Am. Chem. Soc.*, **2013**, *135*, 2076-2079.
22. E. Nasybulin, W. Xu, M. H. Engelhard, Z. Nie, S. D. Burton, L. Cosimbescu, M. E. Gross and J.-G. Zhang, *J. Phys. Chem. C*, **2013**, *117*, 2635-2645.
23. X. Lin, L. Zhou, T. Huang and A. Yu, *J. Mater. Chem. A*, **2013**, *1*, 1239-1245.
24. V. Etacheri, D. Sharon, A. Garsuch, M. Afri, A. A. Frimer and D. Aurbach, *J. Mater. Chem. A*, **2013**, *1*, 5021-5030.

25. M. Mirzaeian and P. J. Hall, *Electrochim. Acta*, **2009**, *54*, 7444-7451.
26. J. Xiao, D. Mei, X. Li, W. Xu, D. Wang, G. L. Graff, W. D. Bennett, Z. Nie, L. V. Saraf, I. A. Aksay, J. Liu and J.-G. Zhang, *Nano Lett.*, **2011**, *11*, 5071-5078.
27. J.-J. Xu, D. Xu, Z.-L. Wang, H.-G. Wang, L.-L. Zhang and X.-B. Zhang, *Angew. Chem., Int. Ed.*, **2013**, *52*, 3887-3890.
28. R. R. Mitchell, B. M. Gallant, C. V. Thompson and Y. Shao-Horn, *Energy Environ. Sci.*, **2011**, *4*, 2952-2958.
29. H.-D. Lim, K.-Y. Park, H. Song, E. Y. Jang, H. Gwon, J. Kim, Y. H. Kim, M. D. Lima, R. O. Robles, X. Lepró, R. H. Baughman and K. Kang, *Adv. Mater.*, **2013**, *25*, 1348-1352.
30. Z. Peng, S. A. Freunberger, Y. Chen and P. G. Bruce, *Science*, **2012**, *337*, 563-566.
31. M. Zhang, S. Fang, A. A. Zakhidov, S. B. Lee, A. E. Aliev, C. D. Williams, K. R. Atkinson and R. H. Baughman, *Science*, **2005**, *309*, 1215-1219.
32. S. Meini, N. Tsiouvaras, K. U. Schwenke, M. Piana, H. Beyer, L. Lange and H. A. Gasteiger, *Phys. Chem. Chem. Phys.*, **2013**, *15*, 11478-11493.
33. J. R. Harding, Y.-C. Lu, Y. Tsukada and Y. Shao-Horn, *Phys. Chem. Chem. Phys.*, **2012**, *14*, 10540-10546.
34. Y. Lu, Z. Wen, J. Jin, Y. Cui, M. Wu and S. Sun, *J Solid State Electrochem*, **2012**, *16*, 1863-1868.
35. F.-S. Ke, B. C. Solomon, S.-G. Ma and X.-D. Zhou, *Electrochim. Acta*, **2012**, *85*, 444-449.

36. L. Wang, M. Ara, K. Wadumesthrige, S. Salley and K. Y. S. Ng, *J. Power Sources*, **2013**, 234, 8-15.
37. E. Yoo and H. Zhou, *ACS Nano*, **2011**, 5, 3020-3026.
38. H.-D. Lim, K.-Y. Park, H. Gwon, J. Hong, H. Kim and K. Kang, *Chem. Commun.*, **2012**, 48, 8374-8376.

Chapter 4. Soluble Catalyst for Efficient Li Air Battery

(The contents of this chapter has been published in *Angewandte Chemie International Edition*. Reprinted from [H.-D. Lim *et al.*, *Angew. Chem., Int. Ed.*, **2014**, *53*, 3926-3931] Copyright 2014 WILEY-VCH)

4.1. Introduction

Growing concerns over the depletion of fossil fuels and the environment has led to global efforts to secure sustainable energy supplies. One of the key elements to a sustainable energy solution is to develop long-life, efficient and low-cost energy storage systems. While Li-ion batteries have served as one of the most reliable energy storage systems thus far, Li-O₂ batteries have recently attracted a considerable amount of interest as an alternative to conventional Li-ion batteries. Li-O₂ chemistry theoretically delivers the greatest energy density among various types of batteries by eliminating the use of the heavy transition metals typically used as redox elements.¹⁻⁴ Li-O₂ batteries operate based on simple reaction chemistry between Li ions and oxygen ($2\text{Li}^+ + \text{O}_2 + 2\text{e}^- \rightarrow \text{Li}_2\text{O}_2$, 2.96 V vs. Li/Li⁺).⁵⁻⁸ The use of the

unlimited source of oxygen as a cathode material is also a strong advantage for its possible widespread usage. Although the reaction mechanism is simple and straightforward, the practical use of Li-O₂ batteries has been restricted by their high over-charge potential, low efficiency, and poor cyclability.^{9,10} These drawbacks are attributable to the formation of solid-type and non-conductive Li₂O₂ discharge products, which induce not only high polarization when they decompose during charging but also poor rate capability and poor reversibility. For these reasons, 'rechargeable' Li-O₂ batteries cannot be operated over a certain number of cycles which is far less than that under which Li-ion batteries typically operate. Moreover, the energy efficiency (output energy/input energy) is unacceptably low for use as an energy storage system.^{11,12}

To overcome the limitations of current Li-O₂ battery technology, diverse approaches combining multiple strategies are required. Each elemental improvement must be combined for an overall performance enhancement. One of the important elemental technologies related to this involves the promotion of the catalytic activity during the charging reaction of Li₂O₂, which is critical to decrease the polarization and increase the reversibility.¹³ Thus far, various types of oxides and metals have been tried as catalysts, showing some improvements.¹⁴⁻¹⁶ However, in addition to their insufficient

catalytic activity, the immobile nature of the interface between the catalysts and the discharge products (solid-solid interface) has also limited the catalytically active region to an area close to the interface.¹⁷ This implies that the incorporation of the catalysts in the electrode requires a proper design considering the possible morphology of the discharge products and the air-electrode shape. On the other hand, recently suggested soluble catalysts using redox mediators potentially exhibit better catalytic activity than their solid counterparts.^{13,18} Unlike immobile solid catalysts, diffusible catalysts are far more likely to catalyze the decomposition of the solid discharge products. Soluble catalysts can even reach the interior of the air-electrode and facilitate the decomposition of non-conductive discharge products, even when the products are electrically isolated. However, in order to maximize the activity of diffusible catalysts, a corresponding air-electrode design should be considered simultaneously.¹⁹⁻²⁴ The air-electrode architecture needs to provide an environment for the diffusible catalyst effortlessly to penetrate throughout the entire air-electrode area. It should also be capable of yielding discharge products with a morphology best suited for recharging reactions by the type of catalyst used.

In this respect, we combined a hierarchically woven porous carbon nanotube (CNT) fibril air-electrode with a highly active redox mediator as

soluble catalyst in our Li-O₂ cell. Upon cycling, the Li₂O₂ discharge products were uniformly coated as a thin layer on the CNT fibril, which provided a high surface area on which the soluble catalysts can effectively react. A cross-woven CNT fibril sheet provided aligned macro- and microscale pores to facilitate the rapid transport of both the reaction ions and the catalysts without clogging even after a deep discharge process.^{20,25} We report that this multiple optimization approach resulted in unprecedentedly high rechargeability in a Li-O₂ battery with the highest energy efficiency. The significantly enhanced catalytic activity caused by the continuous ‘highway’ for diffusing catalysts also led to markedly reduced polarization (~0.25 V). The cycle performance surpassed that of any other reported Li-O₂ battery, establishing stable cyclability that exceeded 900 cycles with 1,000 mAh g⁻¹. The significant enhancement of the rechargeability and the efficiency reported here is expected to pave the way to the development of practically ‘rechargeable’ Li-O₂ batteries.

4.2. Experimental Details

Preparation of Li-O₂ cells. The air-electrode was prepared by stacking 10 sheets of CNT fibrils onto a Ni mesh (Nillaco Corp., 12.7 mm in diameter) current collector. The detailed procedure for fabrication of the air-electrode has been described in previous reports.^{20,25} Li metal (3/8 inch diameter), a glass fiber separator (Whatman GF/D microfiber filter paper, 2.7 μm pore size), and the CNT-based air-electrode were assembled in sequence in a Swagelok-type Li-air cell. 1M lithium bis(trifluoromethane)sulfonamide (LiTFSI) in tetraethylene glycol dimethylether (TEGDME) was used as the electrolyte, and 0.05 M LiI was added as the redox mediator. All of the Li-O₂ cells were operated in a pure 770-Torr oxygen atmosphere that was accurately maintained using an automated throttle valve. The prepared air-electrode and separator were soaked in the electrolyte prior to assembly to ensure sufficient absorption of the electrolyte. Before the test, all cells were stabilized for 1 h in an oxygen atmosphere.

Characterizations. The electrochemical properties were measured using a potentiogalvanostat (WonA Tech, WBCS 3000, Korea) at a current density of 2000 mA g⁻¹. All discharge/charge capacities were calculated based on per-gram units of the CNT fibril only. No binder or additives were used. X-

ray photoelectron spectroscopy (XPS, Thermo VG Scientific, Sigma Probe, UK), X-ray diffractometry (XRD, Rigaku, D/MAX-RB diffractometer, Tokyo, Japan), High-resolution dispersive Raman microscopy (HRD-Raman, LabRAM HR UV/Vis/NIR), field-emission scanning electron microscopy (FE-SEM, Philips, XL 30 FEG, Eindhoven, Netherlands), and transmission electron microscopy (TEM, JEOL 3010, Japan) were used for characterization purpose.

4.3. Results and Discussion

4.3.1. Redox mediator and air-electrode architecture

Redox mediators as a diffusible catalyst in Li-O₂ batteries must conform to several conditions, as follows. (1) The redox potential (oxidation/reduction) of the mediator should be compatible with that of Li₂O₂ formation, *i.e.*, the oxidation potential needs to be slightly higher than the equilibrium potential of the Li₂O₂ formation. (2) The oxidized form of the redox mediator should be capable of efficiently decomposing Li₂O₂. (3) The redox mediator must not react with electrolyte solvents or the Li metal anode, and it should be highly dissolvable in the electrolyte. Considering the above requirements, we selected LiI as the soluble redox mediator for our Li-O₂ system due to its appropriate redox potential and stability in conventional organic electrolytes.^{18,26} The expected redox mediator reaction is one in which iodide (I⁻) ions are initially oxidized on the electrode surface to I₃⁻ or I₂ while charging. Subsequently, the oxidized reactants (I₃⁻ or I₂) chemically react with Li₂O₂, producing Li⁺ and O₂ gas, with a reverse reaction into the initial iodide (I⁻) ions.^{18,26}

Combined with the LiI redox mediator, the air-electrode framework was optimized to facilitate its transport through the electrode and maximize the

catalytic activity. Our combined strategy is schematically illustrated in Figure 4-1. In a conventional carbon electrode using Ketjen black or Super P carbon, the over-potential during charge is generally high without a catalyst (The red line in Figure 4-1). When a soluble catalyst is used, the over-potential is reduced, but it can still be appreciably high if the clogging of the pores inhibits the efficient transport of both the catalysts and the reaction products during the discharge process (the blue line in Figure 4-1). This situation is feasible when irregular carbon particles in a conventional air-electrode are distributed in a disorderly manner. In such a case, the discharge products are randomly agglomerated and block the pores of the air-electrode.^{20,27,28} On the other hand, a hierarchically aligned porous air-electrode framework (Figure 4-2) can prohibit clogging by the discharge products. The presence of both micro- and nano-pores is expected to lead to a thin and uniform formation of Li_2O_2 on the CNT surface, which will maintain the rapid pathway for both the soluble catalyst and the reaction products (the green line in Figure 4-1).^{20,25}

4.3.2. Electrochemical performances of the Li-O₂ cell

Figure 4-3 shows the electrochemical properties of CNT fibril electrodes with the LiI redox mediator. While CNT electrodes without catalysts

exhibited relatively high over-potential (~ 1.5 V) during charge, a slightly lower over-potential (~ 0.5 V) was observed in the presence of a solid Pt catalyst. Furthermore, an even lower over-potential (~ 0.25 V) could be achieved with a soluble LiI catalyst. A marked reduction of the polarization was found regardless of the type of salt (LiPF_6 or LiTFSI) used, as shown in Figure 4-3a. It is noteworthy that the over-potential during charge is nearly identical to the theoretical reaction potential of I^- to I_3^- or I_2 ,^{18,26} showing the smallest polarization value to date. The over-potential during charge is even lower than that during the discharge process. As a consequence of the remarkable reduction of the over-potential, the cyclability was dramatically improved, as shown in Figures 4-3b and 4-3c. Stable and reversible cycling was observed for more than 900 cycles without a notable change in the electrochemical profile. This cycle performance far exceeds those of the CNT fibril electrode without a catalyst (~ 90 cycles)²⁰ or with Pt as a catalyst (~ 170 cycles)²⁵, as shown in Figure 4-4. Even when the discharge depth was increased to 3000 mAh g^{-1} , stable cycling was maintained for more than 300 cycles (Figure 4-3d).

The activity of the soluble redox mediator is believed to be synergistically enhanced through the combination with the hierarchically aligned porous CNT framework. Although Li-O_2 cells with a conventional carbon electrode

(e.g., Ketjen black and binder) also showed reduced polarization when a soluble catalyst was used, as shown in Figure 4-5, they are greatly inferior compared to the aligned porous CNT fibril electrodes. The polarization during charge is still greater than 3.5 V and the enhancement of the cyclability is limited. These findings indicate that the performance of the redox mediator varies significantly depending on the structure of the air-electrode, implying that an optimal environment for a soluble catalyst freely to diffuse through the interior/exterior of the air-electrode is necessary to maximize the catalytic performance.

Along with the redox mediator and electrode architecture, another important aspect that we believe contributed to the remarkable cycle stability is the suppression of the side reactions that often take place with high-voltage cycling. The high charging voltage arising from the large polarization induces problems such as carbon corrosion and electrolyte deterioration.^{29,30} Ottakam Thotiyl *et al.* showed that the irreversible formation of byproducts due to the corrosion of the carbon begins to occur above 3.5 V, resulting in poor cycle life of Li-O₂ batteries.²⁹ Byproducts including Li₂CO₃ and LiOH generally form during cycling and continuously accumulate on the carbon surface during this process. Decomposition of the TEGDME solvent is also triggered over 4.0 V, forming byproducts such as

Li_2CO_3 and LiOH .^{31,32} Given that the charge process is mainly done at 3.25 V and considering that the terminal voltage of the charge remains below 3.5 V (Figure 4-3c) during the cycling process, main side reactions are expected to be substantially suppressed in our case.

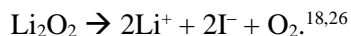
The power capability of the Li-O₂ cell was tested at various current rates, as shown in Figures 4-6a and 4-6b. The current rate was gradually raised from 200 mA g⁻¹ to 6,000 mA g⁻¹ and then reduced back to 200 mA g⁻¹. It is notable that the degree of polarization did not drastically increase, even when the current density was 30 times higher. The charging voltage remained below 3.5 V and the polarization did not exceed 0.5 V, even at the high current rate of 6,000 mA g⁻¹. Furthermore, the electrochemical profiles remained nearly constant after the return to the initial rate, as shown in Figure 4-6b. This result demonstrates superior rate-capability and reversibility. For a further investigation of the reversibility of the Li-O₂ cells, the galvanostatic intermittent titration technique (GITT) was used for ten consecutive cycles, as shown in Figures 4-6c and 4-6d. Nearly identical electrochemical profiles were observed for all cycles. The relaxation potential at each step approached the theoretical potential of Li₂O₂ formation, indicating that the formation/decomposition of Li₂O₂ continued quite reversibly.

4.3.3. Reversibility and the redox mediator

The reversible formation/decomposition of Li_2O_2 was investigated further with a TEM analysis. Figure 4-7a shows that reaction products were deposited on the CNT surface after the discharge process. While most discharge products form a thin layer on the CNT, there were some bead-like products after the full discharge process. Nevertheless, they were dispersed on the CNT surface without clogging,^{6,20,25,33} which is expected to provide a favorable environment for soluble catalysts efficiently to flow. The diffraction patterns in Figure 4-7c suggest the formation of Li_2O_2 during cycling. The observed bead formation and the diffraction patterns are consistent with previous reports in which no catalyst was used.^{20,25} Upon charging, the Li_2O_2 completely disappear from the electrode, indicating high rechargeability, as shown in Figure 4-7b. The diffraction patterns in Figure 4-7c also confirm the absence of Li_2O_2 after the charge. Additionally, microscopic images of the formation/decomposition of Li_2O_2 were monitored by HR-TEM, as shown in Figure 4-7d. We observed that the Li_2O_2 begins to grow directly on the CNT surface with a thickness of a few nanometer until the half discharge. A slight modulation was detected for the thin Li_2O_2 layer on the CNT. With further lithiation, this modulation became more prominent and led to the formation of the bead-type particles. Charging

of the air-electrode reversed the reaction. The bead-type Li_2O_2 first disappears, and the modulated Li_2O_2 layer on the CNT then gradually fades away as the charge continues. Finally, all of the discharge products completely disappear at the end of the charging process.

The reversibility of the redox mediator was investigated by assessing whether the iodide ions (I^-) return to the initial state during cycling. Electrolytes in the as-prepared state, after discharging, and after charging were examined using Raman spectroscopy, as shown in Figure 4-7e. While the oxidized forms of I_2 and I_3^- have clear vibration modes at 189, 112 and 165 cm^{-1} , respectively, the initial form of I^- has no vibration mode.^{34,35} No noticeable changes were observed after discharging and charging and no trace of I_2 or I_3^- ions was noted. These findings indicate that these oxidized species immediately return to their initial I^- ion state upon a reaction with Li_2O_2 during the charge process. To assess the ability of the redox mediator as catalysts further, we dissolved 0.05 M of I_2 in the TEGDME solvent and injected Li_2O_2 powder into the solvent. Figure 4-7f shows that oxygen gas evolved immediately after the injection of the Li_2O_2 , indicating a rapid reaction between the redox mediator and the Li_2O_2 . The volume of the evolved oxygen as measured by gas spectroscopy was $\sim 4.14\text{ mL}$, which is comparable to the expected value (4.48 mL) based on the reaction of $\text{I}_2 +$



The combined approach using soluble catalysts and an aligned porous electrode can be applied to various types of Li-O₂ cells. As a model example, we applied this strategy to a hybrid Li-O₂ system in which dual electrolytes of TEGDME (liquid) and LiSICON (solid) were used in the configuration of Li metal anode/LiTFSI in the TEGDME/LiSICON/LiI + LiTFSI in TEGDME/cathode in sequence. Figure 4-8 shows that electrochemical profiles analogous to the conventional Li-O₂ system were obtained in the hybrid Li-O₂ system with remarkably small over-potential levels, indicating that this combined approach is also valid in other types of Li-O₂ cells.

A persistent problem with all the current Li-O₂ cells, nevertheless, is that the electrolyte is not sufficiently stable. In the presence of Li metal, TEGDME forms LiOH byproducts on Li anode^{13,36,37}; thus, a protection layer on the anode is needed to prevent undesirable reactions. The partial formation of byproducts on the CNT surface also proceeds with cycles and eventually leads to cell failure. We found that the air-electrodes after failure were covered with the byproducts of Li₂CO₃ and LiOH (Figure 4-9). The air-electrode after failure could not be reused, even if we used a new electrolyte, separator and Li metal. This implies that some degree of electrode degradation is unavoidable even if we control the degree of polarization

below 3.5 V. The development of a reliably stable electrolyte and air-electrode substrate is indispensable for even longer cycling exceeding 1,000 times for Li-O₂ batteries. These problems must be addressed to spur further progress in Li-O₂ battery technology.

4.4. Conclusion

In summary, a highly efficient and reversible Li-O₂ battery was demonstrated using a hierarchically aligned porous air-electrode in combination with a soluble LiI catalyst. The optimal design of the air-electrode provides effectively rapid channels for both the reaction products and the soluble catalyst. The facile diffusion of the soluble catalyst throughout the entire air-electrode could remarkably decrease the polarization during the charging process, enabling dramatically enhanced rechargeability and excellent energy efficiency. The key challenge for future Li-O₂ batteries is synergistically to combine diverse elemental technologies for an overall performance enhancement.

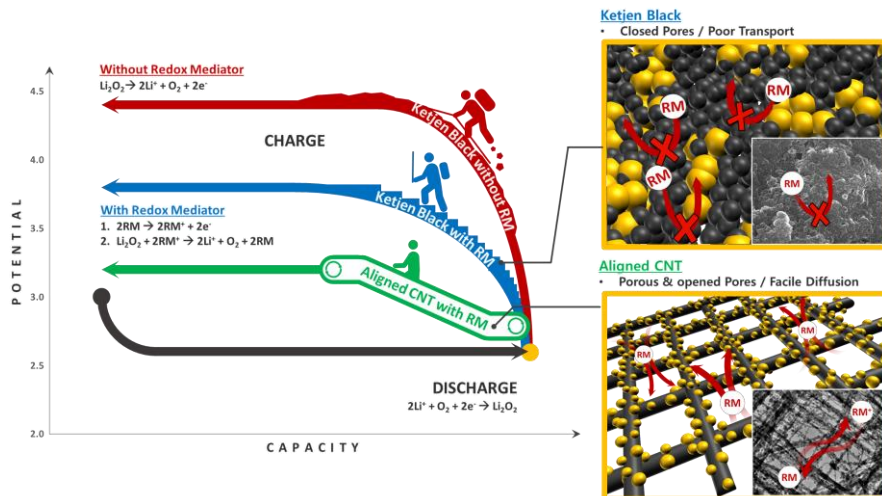


Figure 4-1. Schematic illustration of the role of the redox mediator in a Li-O₂ battery system made using a hierarchical CNT fibril electrode.

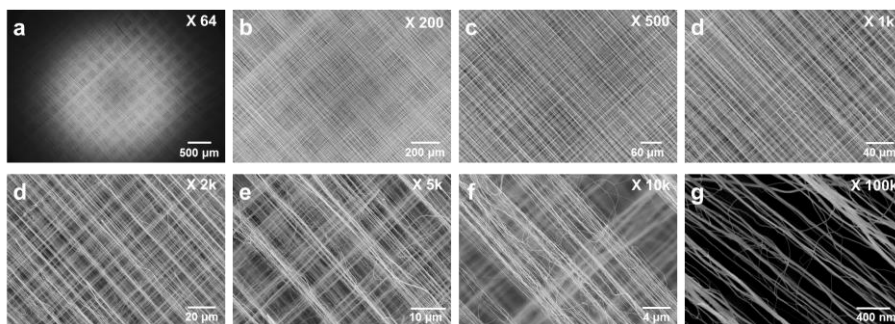


Figure 4-2. SEM images of the CNT fibril electrode at various magnifications.

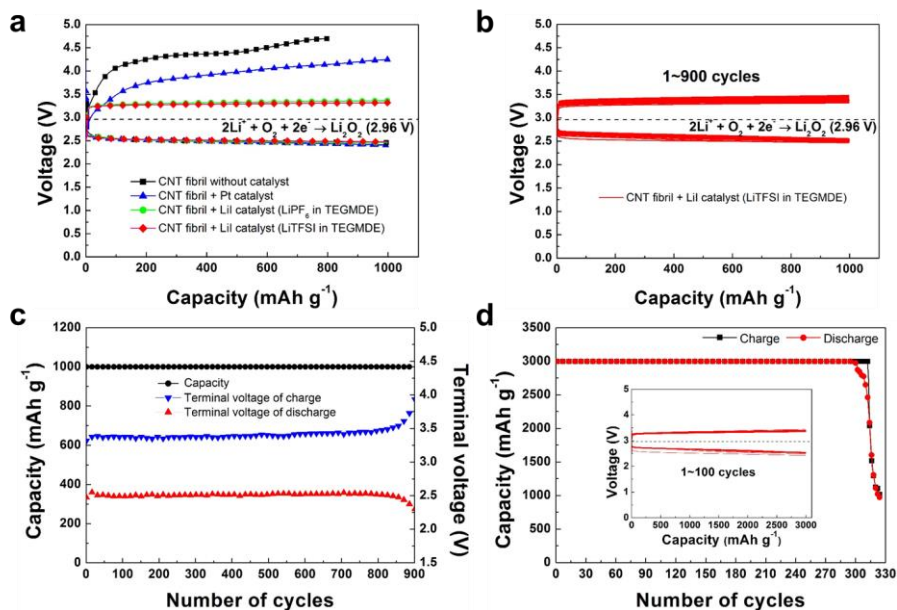


Figure 4-3. (a) Discharge/charge profiles of CNT fibril electrodes without a catalyst, with the Pt catalyst, and with the LiI catalyst at a discharge depth of 1000 mAh g⁻¹ and a current rate of 2,000 mA g⁻¹. (b) Electrochemical profiles and (c) cyclability and terminal voltages of the CNT fibril electrodes with a LiI catalyst. (d) Cyclability of the CNT fibril electrodes in the presence of a LiI catalyst at a discharge depth of 3000 mAh g⁻¹.

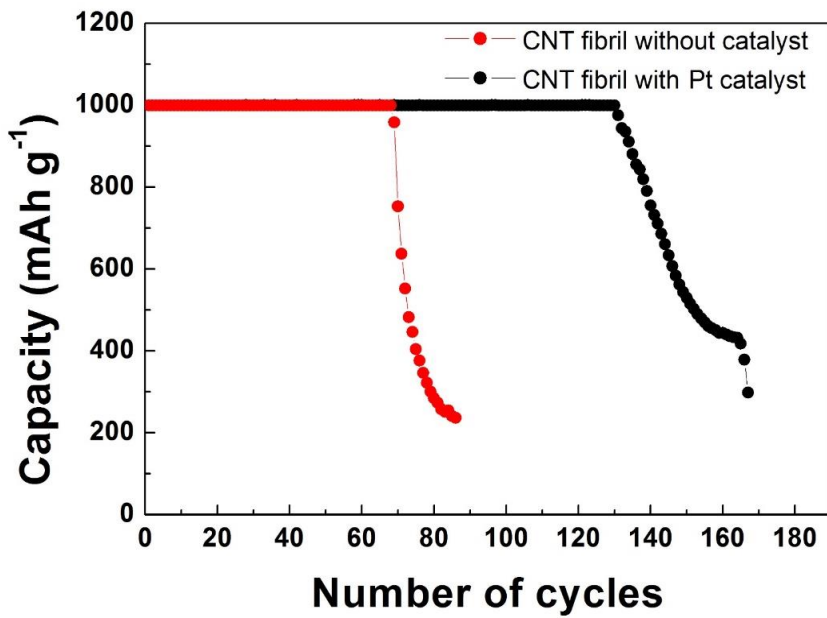


Figure 4-4. Cyclability of the CNT fibril electrodes without a catalyst and with the Pt catalyst.

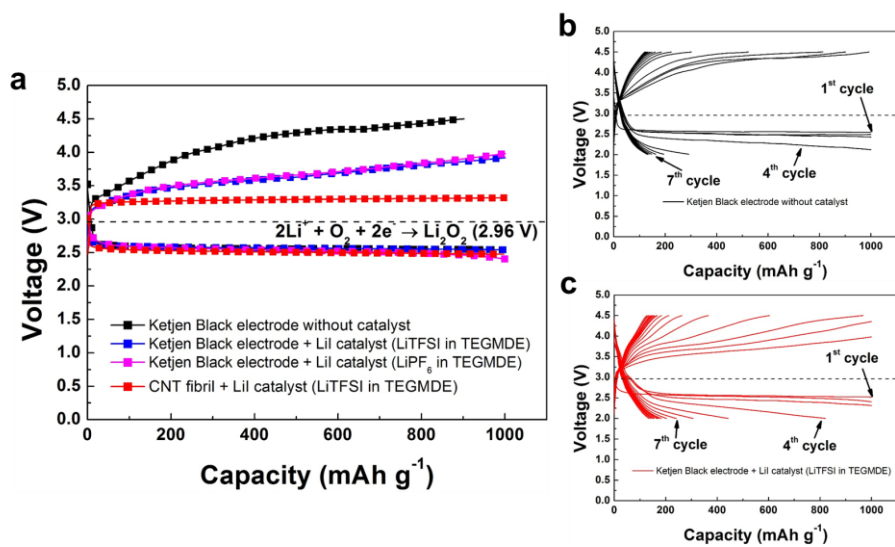


Figure 4-5. Electrochemical properties of a Li-O₂ cell using a Ketjen black electrode without a catalyst and with the LiI catalyst.

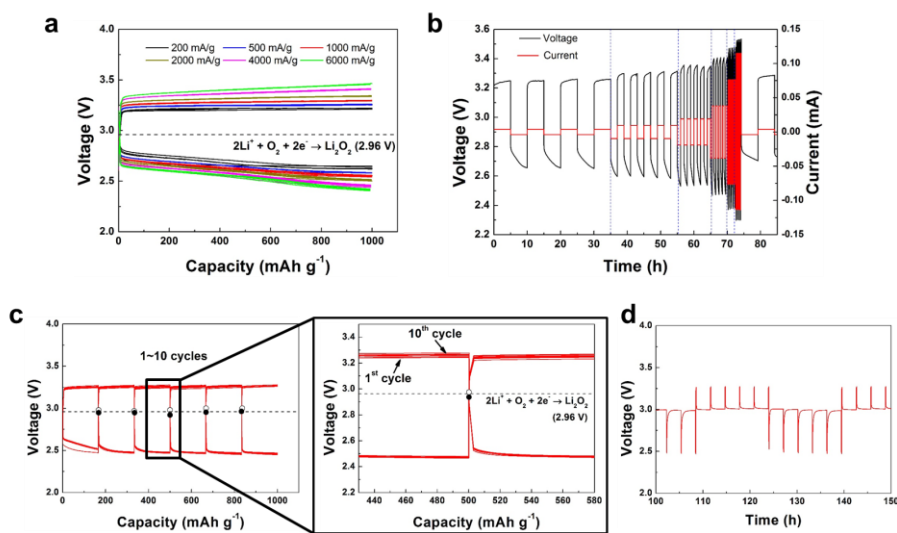


Figure 4-6. (a,b) Power capability of CNT fibril electrodes in the presence of a LiI catalyst at current rates from 200 mA g⁻¹ to 6000 mA g⁻¹. Each step is measured for 5 cycles. (c) GITT voltage profiles and (d) the corresponding potential vs. time plot for 10 cycles. Three hours of relaxation time was allowed at each step.

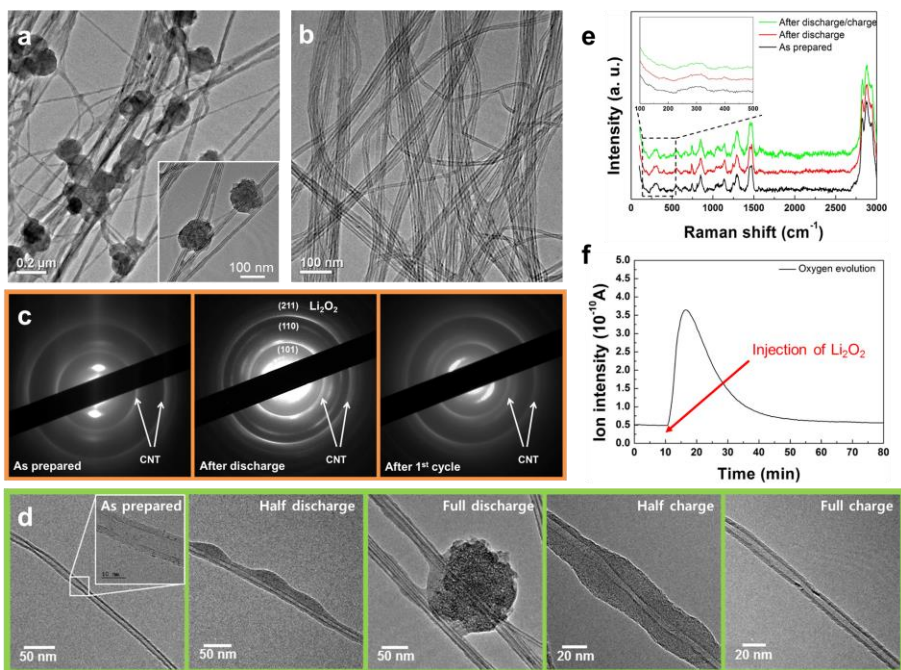
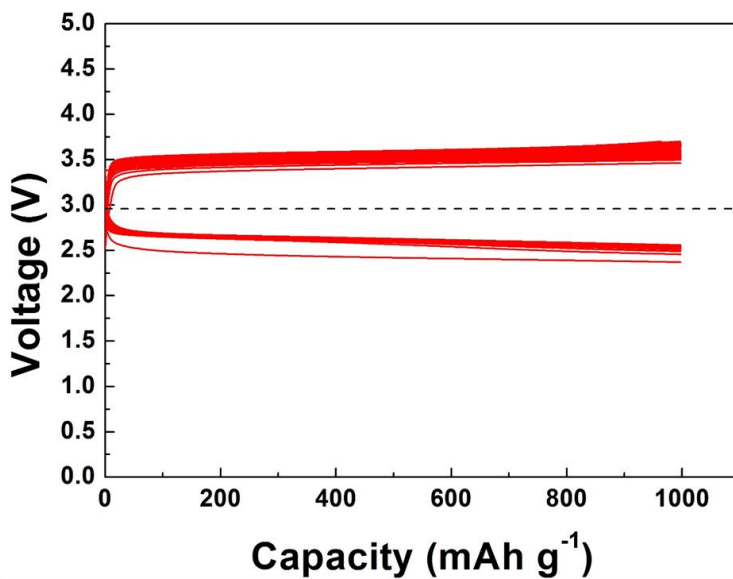


Figure 4-7. (a,b) TEM images of the air-electrode made using the LiI catalyst after the first discharge and first cycle. (c) The corresponding diffraction patterns as prepared, post-discharge, and after the first cycle. (d) Ex-situ TEM analysis of the discharge products; the procedure for the formation of Li₂O₂ on the CNT surface and its decomposition. (e) Raman spectra of the as prepared electrolytes, after the first discharge, and after the first cycle. (f) Gas analysis of the evolved oxygen after injection of Li₂O₂ powder into 0.05M I₂ dissolved in TEGDME solvent.



Anode | LiTFSI in TEGDME | Solid Electrolyte | LiI+LiTFSI in TEGDME | Cathode

Figure 4-8. Discharge/charge profiles of a Li-O₂ cell using a dual-electrolyte system; this is composed of a Li metal anode/LiFTSI in the TEGDME/solid electrolyte/LiI + LiFTSI in the TEGDME/cathode. CNT fibril electrode with the LiI catalyst at a discharge depth of 1000 mAh g⁻¹ and a current rate of 2,000 mA g⁻¹ is shown.

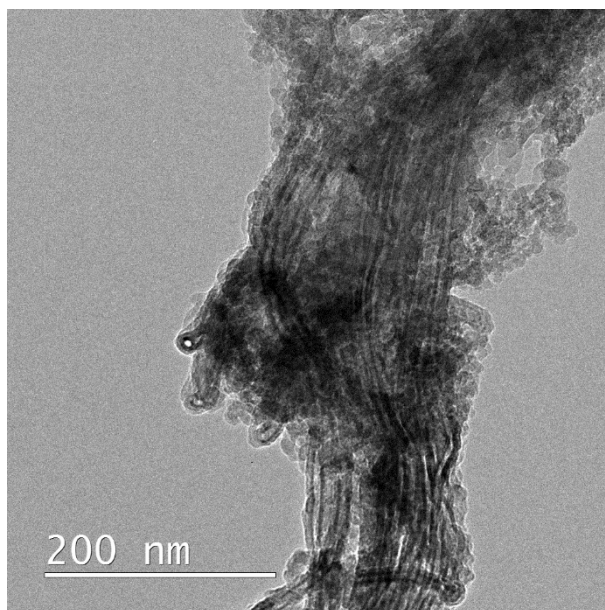


Figure 4-9. TEM image of the air-electrode at the end of the cycles.

4.5. References

1. K. M. Abraham, Z. Jiang, *J. Electrochem. Soc.* **1996**, *143*, 1-5.
2. P. G. Bruce, S. A. Freunberger, L. J. Hardwick, J.-M. Tarascon, *Nat. Mater.* **2012**, *11*, 19-29.
3. D. Oh, J. Qi, Y.-C. Lu, Y. Zhang, Y. Shao-Horn, A. M. Belcher, *Nat. Commun.* **2013**, *4*, 2756.
4. D. Zhai, H.-H. Wang, J. Yang, K. C. Lau, K. Li, K. Amine, L. A. Curtiss, *J. Am. Chem. Soc.* **2013**, *135*, 15364-15372.
5. J.-J. Xu, Z.-L. Wang, D. Xu, L.-L. Zhang, X.-B. Zhang, *Nat. Commun.* **2013**, *4*, 2438.
6. E. Yilmaz, C. Yogi, K. Yamanaka, T. Ohta, H. R. Byon, *Nano Lett.* **2013**, *13*, 4679-4684.
7. H.-K. Lim, H.-D. Lim, K.-Y. Park, D.-H. Seo, H. Gwon, J. Hong, W. A. Goddard, H. Kim, K. Kang, *J. Am. Chem. Soc.* **2013**, *135*, 9733-9742.
8. X. Ren, S. S. Zhang, D. T. Tran, J. Read, *J. Mater. Chem.* **2011**, *21*, 10118-10125.
9. B. Sun, P. Munroe, G. Wang, *Scientific Reports* **2013**, *3*, 2247.
10. J. Lu, Y. Lei, K. C. Lau, X. Luo, P. Du, J. Wen, R. S. Assary, U. Das, D. J. Miller, J. W. Elam, H. M. Albishri, D. A. El-Hady, Y.-K. Sun, L. A. Curtiss, K. Amine, *Nat. Commun.* **2013**, *4*, 2383.
11. S. Kumar, C. Selvaraj, N. Munichandraiah, L. G. Scanlon, *RSC Adv.* **2013**, *3*, 21706-21714.
12. J.-L. Shui, H.-H. Wang, D.-J. Liu, *Electrochem. Commun.* **2013**, *34*, 45-47.
13. Y. Chen, S. A. Freunberger, Z. Peng, O. Fontaine, P. G. Bruce, *Nat.*

Chem. **2013**, *5*, 489-494.

14. Y.-C. Lu, Z. Xu, H. A. Gasteiger, S. Chen, K. Hamad-Schifferli, Y. Shao-Horn, *J. Am. Chem. Soc.* **2010**, *132*, 12170-12171.

15. Y. Lu, Z. Wen, J. Jin, Y. Cui, M. Wu, S. Sun, *J. Solid State Electr.* **2012**, *16*, 1863-1868.

16. W.-H. Ryu, T.-H. Yoon, S. H. Song, S. Jeon, Y.-J. Park, I.-D. Kim, *Nano Lett.* **2013**, *13*, 4190-4197.

17. H.-D. Lim, H. Gwon, H. Kim, S.-W. Kim, T. Yoon, J. W. Choi, S. M. Oh, K. Kang, *Electrochim. Acta* **2013**, *90*, 63-70.

18. T. Shiga, Y. Hase, Y. Kato, M. Inoue, K. Takechi, *Chem. Commun.* **2013**, *49*, 9152-9154.

19. G. Zhao, Z. Xu, K. Sun, *J. Mater. Chem. A* **2013**, *1*, 12862-12867.

20. H.-D. Lim, K.-Y. Park, H. Song, E. Y. Jang, H. Gwon, J. Kim, Y. H. Kim, M. D. Lima, R. O. Robles, X. Lepró, R. H. Baughman, K. Kang, *Adv. Mater.* **2013**, *25*, 1348-1352.

21. W.-M. Liu, T.-T. Gao, Y. Yang, Q. Sun, Z.-W. Fu, *Phys. Chem. Chem. Phys.* **2013**, *15*, 15806-15810.

22. S. Liu, Z. Wang, C. Yu, Z. Zhao, X. Fan, Z. Ling, J. Qiu, *J. Mater. Chem. A* **2013**, *1*, 12033-12037.

23. Z. Guo, D. Zhou, X. Dong, Z. Qiu, Y. Wang, Y. Xia, *Adv. Mater.* **2013**, *25*, 5668-5672.

24. J.-J. Xu, D. Xu, Z.-L. Wang, H.-G. Wang, L.-L. Zhang, X.-B. Zhang, *Angew. Chem., Int. Ed.* **2013**, *52*, 3887-3890.

25. H.-D. Lim, H. Song, H. Gwon, K.-Y. Park, J. Kim, Y. Bae, H. Kim, S.-K. Jung, T. Kim, Y. H. Kim, X. Lepro, R. Ovalle-Robles, R. H. Baughman, K. Kang, *Energy Environ. Sci.* **2013**, *6*, 3570-3575.

26. G. V. Chase, S. Zecevic, T. W. Wesley, J. Uddin, K. A. Sasaki, P. G. Vincent, V. Bryantsev, M. Blanco, D. D. Addison, **2012**, US Patent Application No. 20120028137.
27. S. S. Zhang, D. Foster, J. Read, *J. Power Sources* **2010**, *195*, 1235-1240.
28. Y. Shao, F. Ding, J. Xiao, J. Zhang, W. Xu, S. Park, J.-G. Zhang, Y. Wang, J. Liu, *Adv. Funct. Mater.* **2013**, *23*, 987-1004.
29. M. M. Ottakam Thotiyl, S. A. Freunberger, Z. Peng, P. G. Bruce, *J. Am. Chem. Soc.* **2012**, *135*, 494-500.
30. B. D. McCloskey, A. Speidel, R. Scheffler, D. C. Miller, V. Viswanathan, J. S. Hummelshøj, J. K. Nørskov, A. C. Luntz, *J. Phys. Chem. Lett.* **2012**, *3*, 997-1001.
31. H.-D. Lim, K.-Y. Park, H. Gwon, J. Hong, H. Kim, K. Kang, *Chem. Commun.* **2012**, *48*, 8374-8376.
32. R. Black, S. H. Oh, J.-H. Lee, T. Yim, B. Adams, L. F. Nazar, *J. Am. Chem. Soc.* **2012**, *134*, 2902-2905.
33. Y. Chen, F. Li, D.-M. Tang, Z. Jian, C. Liu, D. Golberg, A. Yamada, H. Zhou, *J. Mater. Chem. A* **2013**, *1*, 13076-13081.
34. A. Spadoni, M. Falconieri, M. Lanchi, R. Liberatore, M. Marrocco, G. S. Sau, P. Tarquini, *Int. J. Hydrogen Energy* **2012**, *37*, 1326-1334.
35. H. Greijer, J. Lindgren, A. Hagfeldt, *J. Phys. Chem. B* **2001**, *105*, 6314-6320.
36. C. Laoire, S. Mukerjee, E. J. Plichta, M. A. Hendrickson, K. M. Abraham, *J. Electrochem. Soc.* **2011**, *158*, A302-A308.
37. J.-L. Shui, J. S. Okasinski, P. Kenesei, H. A. Dobbs, D. Zhao, J. D. Almer, D.-J. Liu, *Nat. Commun.* **2013**, *4*, 2255.

Chapter 5. Li-O₂/CO₂ battery

(The contents of this chapter has been published in *Journal of the American Chemical Society*. Reprinted with permission from [H.-D. Lim *et al.*, *J. Am. Chem. Soc.* **2013**, *135*, 9733-9742.]. Copyright (2013) American Chemical Society)

5.1. Introduction

The greatly increased demand for high energy density storage systems has heightened interest in Li-air batteries. A Li-air system potentially can deliver a gravimetric energy density of ~3,500 Wh/kg (from the simple reaction of Li with dioxygen (O₂)), which is substantially higher than other battery types (e.g., ~600 Wh/kg for a LiCoO₂ system).¹⁻⁴ However, despite this great advantage in energy density,⁵⁻⁷ major limitations in the reaction mechanism and its relation to the practical problems of Li-air batteries, which include poor cyclability, high polarization, and low rate capability, remain.⁸⁻¹² Furthermore, it is not yet known how the presence of the non-O₂ components of air affect the reaction mechanism in Li-air batteries because most previous studies have been conducted in a pure O₂ atmosphere, under the assumption that the other components of air will be less important in the operation of the

battery.¹³⁻¹⁶ In order to develop a Li-‘air’ battery technology usable at ambient conditions, it is critical to elucidate the effects of the other constituents of air (N₂, Ar, and CO₂) on the operations of the Li-air battery.

Among the various constituents of air, CO₂ should have the most influence on the chemistry of the Li-air cell. Although N₂ and noble gases such as Ar are more abundant in ambient air, the conventional cathode voltage range of ~3 V cannot activate electrochemical reactions involving these gases and Li; for example, the theoretical formation potential is ~0.444 V for the reaction $3\text{Li} + 1/2\text{N}_2 \rightarrow \text{Li}_3\text{N}$ [$\Delta_f G^\circ(\text{Li}_3\text{N}) = -10.25 \text{ kcal/mol/Li}$].¹⁷ In contrast, CO₂ is known to be much less inert than N₂ or Ar, and it can therefore undergo electrochemical reactions with Li (some involving O₂ as well); for example, the theoretical voltage for the formation of Li₂CO₃ is 3.82 V for the reaction $2\text{Li} + 1/2\text{O}_2 + \text{CO}_2 \rightarrow \text{Li}_2\text{CO}_3$ [$\Delta_f G^\circ(\text{Li}_2\text{CO}_3) = -135.30 \text{ kcal/mol/Li}$].¹⁸ Additionally, Li₂CO₃ is more a chemically stable compound than Li₂O₂ [$\Delta_f G^\circ(\text{Li}_2\text{O}_2) = -68.26 \text{ kcal/mol/Li}$].¹⁸ The difference in chemical stability implies that there is always a thermodynamic driving force to convert Li₂O₂, the desired discharge product of a Li-air cell, into Li₂CO₃ in the presence of CO₂. This observation has also led people to believe that the irreversible formation of Li₂CO₃ might limit the cyclability of Li-‘air’ batteries.¹⁹

Moreover, the high solubility of CO₂ gas in organic electrolytes (~50 times

more soluble than O_2)²⁰ results in the major possibility of CO_2 being incorporated in battery reactions, despite its low concentration in ambient air. Thus, to further the development of Li-air battery technology, it is critical to understand the reactions involving CO_2 and the chemistry of Li_2CO_3 within a Li-air cell. Although recent experimental studies have examined the effect of CO_2 gas in Li-air cells,^{21,22} there remains no mechanistic understanding of how the Li- O_2 reaction pathways and Li- O_2/CO_2 reaction pathways will compete with each other and how the final discharge product will be regulated during electrochemical reactions in Li-air batteries.

In this work, we report both theoretical studies regarding the fundamental reaction mechanism and experimental studies of Li-air battery performance, which is significantly altered by the presence of CO_2 . In particular, we showed that Li_2CO_3 can be selectively produced as a final discharge product depending on the dielectric properties of the electrolyte and demonstrated for the first time that Li_2CO_3 can undergo reversible reactions during the Li- O_2/CO_2 battery cycles.

5.2. Experimental Details

5.2.1. Computational details

We carried out quantum mechanical calculations based on density functional theory (DFT) using Jaguar 7.9.²³ We used the Becke three-parameter functional (B3)²⁴ combined with the correlation functional of Lee, Yang, and Parr (LYP)²⁵, along with the Pople 6-311++G** basis set.²⁶ The ground state geometries were fully optimized, and the transition state geometries were confirmed to have a single imaginary frequency. To describe various electrolytes²⁷⁻³⁰, solvation free energies were evaluated using the PBF (Poisson-Boltzmann Finite element method),^{31,32} as implemented in the Jaguar package. We used the experimental dielectric constant (ϵ) and calculated probe radii (R) from the molecular weight and liquid density of each electrolyte to describe the solvation of different electrolytes as listed in Table 5-1. The solvation energies of reactants, intermediates, and products were determined with self-consistently full optimizing solution phase geometries that include the atomic forces exerted by the implicit solvent in the reaction field. For the solvation energy of the transition state, we added the solvation energy calculated at the gas-phase transition state geometry in all cases, except the reaction of O_2^- with Li^+ , as

this gas-phase reaction is barrier-less. To evaluate the barrier energy for the reaction of O_2^- with Li^+ , we calculated the solution phase reaction energy profile while changing the distance between O_2^- and Li^+ and then used the maximum value as the barrier energy (see Figure 5-1).

In order to evaluate reaction energies of oxidation/reduction, it is important to define the reference energy of the electron generated from the electrode. We defined this electron reference energy as the energy cost associated with dissolving a Li cation into the electrolyte from solid Li (see SI), which is the energy for the counter half-reaction occurring at the anode. This definition allows direct comparison of the reaction energy (ΔE) with the reduction potential values for a Li/Li^+ electrode (V) *via* the Nernst equation, $\Delta E \approx \Delta G = -nFV$ (where ΔG is the reaction free energy, F is the Faraday constant, and n is the number of electrons involved in the reactions). For example, the calculated reaction energies for the O_2 reduction reaction are 2.64 eV for dimethyl sulfoxide (DMSO) and 1.51 eV for dimethoxyethane (DME), which are reasonably close to the experimental values of ~ 2.3 V (0.1 M TBAPF₆, DMSO) and ~ 1.8 V (0.1 M TBAPF₆, DME).³³

5.2.2. Experimental details

The porous air electrode was composed of a mixture of Ketjen black carbon

(EC 600JD, Ilshin Chemtech) and a binder (Kynal 2801) in a weight ratio of 8:2. N-methyl-2-pyrrolidone (NMP, Sigma-Aldrich, 99.5%) was used as a dispersing agent. The mixtures were pasted onto a Ni mesh or carbon paper. The electrode was dried at 120 °C for 1 hour to remove the residual NMP. Lithium metal (3/8 inch diameter), a glass fiber separator (Whatman GF/D microfiber filter paper, 2.7 μm pore size), and the air electrode were assembled into Swagelok-type Li-air cell.¹⁰ Either 0.21 ml of 1 M LiPF₆ in DMSO or 0.1 M LiPF₆ in DME was used as electrolyte. Each of the ‘Li-O₂ cells’ was operated in a pure oxygen atmosphere at a pressure of 770 Torr, maintained at a constant value using an automated throttle valve. The ‘Li-O₂/CO₂ cells’ were operated at a 1:1 pressure ratio of O₂ and CO₂, while all other conditions were identical to those for the Li-O₂ cells. The electrochemical properties were measured using a potentiogalvanostat (WonA Tech, WBCS 3000, Korea). The samples were characterized using an X-ray diffractometer (XRD, D8-Advance, Bruker, Germany) equipped to measure Cu K_α radiation and the Fourier transform infrared (FTIR, FT-IR-4200, JASCO, Japan) spectra in an argon atmosphere. The morphologies of compounds were observed using a field emission scanning electron microscope (FE-SEM, Philips, XL 30 FEG, Eindhoven, Netherlands).

5.3. Results and Discussion

5.3.1. Calculations for the reaction pathways

The sequential reactions occurring in the Li-O₂/CO₂ system were investigated using DFT first-principles calculations. Based on the reduction potential of CO₂/CO₂⁻ (-2.0 V vs. Ag in DMSO), which is about 1.6 V lower than that of O₂/O₂⁻ (-0.4 V vs. Ag in DMSO),²⁰ it is reasonable to assume that the first reaction step is an “*oxygen reduction reaction (ORR) step*”, as in a conventional Li-O₂ cell:^{34,35}



After the oxygen molecule captures an electron from the cathode, a radical nucleophile reagent is created that can react vigorously with neutral or cationic species in the cell, such as CO₂, Li⁺, or electrolytes. We designate this reaction step as the “*initial complex formation (ICF) step*” for the following discussion. This step consists of the following possible reactions:



Figure 5-2 illustrates the possible reaction pathways for the *ICF*, including the reaction energy (ΔE) and the activation barrier (ΔE^\ddagger) for this reaction in

the three electrolyte-containing media (EC, DMSO and DME). Detailed structural information for these chemical complexes is provided in the Figure 5-2.

In the electrolyte EC (Figure 5-3a), the reaction of the O_2^- radical with CO_2 is both thermodynamically and kinetically favored over its reaction with Li^+ ($\Delta E = -0.1$ kcal/mol and $\Delta E^\ddagger = 24.0$ kcal/mol for (2.1); $\Delta E = -1.4$ kcal/mol and $\Delta E^\ddagger = 3.5$ kcal/mol for (2.2)). However, considering the possibility of O_2^- reacting also with surrounding electrolyte molecules reveals that a ring-opening reaction with EC (2.3) is the most thermodynamically favored, with $\Delta E = -7.1$ kcal/mol (see Figure 5-2 for the structure of the decomposed EC). Thus, although the activation barrier (ΔE^\ddagger) for (2.3) (15.8 kcal/mol) is higher than that for (2.2) (3.5 kcal/mol), the significantly higher stability of the final products of (2.3) is expected to drive the reaction pathway toward decomposition of the EC electrolyte. This result is consistent with previous experiments using carbonate-based electrolytes in Li- O_2 cells³⁶ and explains why Li_2O_2 formation is not preferred in such systems. On the other hand, the electrolyte decomposition reaction (2.3) is not the most favored reaction in DMSO (Figure 5-3b) or in DME (Figure 5-3c) electrolytes. Here, the decomposition reaction is uphill (DMSO: 3.8 kcal/mol and DME: 23.4 kcal/mol), and the activation barriers are considerably higher than for (2.1)

and (2.2). This observation agrees well with recent findings that non-carbonate-based electrolytes are less susceptible to decomposition in Li-O₂ cells.^{27,37-39}

Nevertheless, the reaction pathway for O₂⁻ in DMSO in the presence of CO₂ is clearly distinguishable from the corresponding reaction pathway in DME. Figure 5-3b shows that the reaction of O₂⁻ with Li⁺ (2.1) results in a nearly identical energy state ($\Delta E = -1.6$ kcal/mol) as does reaction with CO₂ (2.2) in DMSO. However, the activation barrier for (2.1) is considerably higher than that for (2.2), implying that the reaction of O₂⁻ with CO₂ is kinetically favored over its reaction with Li⁺ in DMSO. In contrast, the reaction of O₂⁻ with Li⁺ is much more likely in DME, as shown in Figure 5-3c. While the activation barriers for both reactions (2.1) and (2.2) in DME are comparable, the final state energy of (2.1) is substantially more stable, indicating of the dominant LiO₂ formation.

We attribute the clearly different behavior of the reactions of O₂⁻ during the *ICF* step in various electrolytes to the variation in the dielectric properties of the solvents. Generally, electrolytes with high dielectric constants (ϵ) effectively shield and thereby stabilize charged ionic species. To initiate such a reaction in a high dielectric electrolyte (such as EC or DMSO), the strongly coordinating solvent shell of a charged species such as Li⁺ and O₂⁻

must be disrupted, at a considerable energy cost. Thus, reaction (2.1), which involves two individual charged species and their strongly coordinating solvent shells, requires a higher energy cost in EC (24.0 kcal/mol) and DMSO (21.8 kcal/mol) than is required in low dielectric DME (3.3 kcal/mol). In comparison, the reaction between O_2^- and CO_2 (2.2) is less sensitive to the dielectric behavior of electrolyte. Here, the reaction energies vary from -4.2 kcal/mol for DME to -1.4 kcal/mol for EC, with comparable activation energies. We attribute this to CO_2 , a neutral species, not forming a strong solvation shell.

Figure 5-4 shows the DFT results for other organic solvents. We see correlation between the reaction energies for *ICF* (2.1 and 2.2) and the dielectric constant of the electrolyte. Here, it is noted that the reaction energies decrease linearly with the inverse of dielectric constant of electrolyte, particularly for (2.1). However, the reaction of O_2^- with CO_2 (2.2) is affected by dielectric constant to a much lesser extent. The opposite behavior of these two reactions implies that for Li- O_2 / CO_2 batteries, O_2^- is likely to react with CO_2 in a high dielectric solvent and more likely to react with Li^+ in a low dielectric solvent. Thus, at the *ICF* step, the reactions mostly depend on the dielectric constant. We recommend that these general dependencies of the chemistry on the dielectric constant be considered in

choosing electrolytes for Li-air cells.

In the following analysis, we focus only on the reaction pathways in DMSO and DME electrolytes because (i) carbonate electrolytes such as EC are susceptible to decomposition upon exposure to O_2^- and (ii) there have been complete studies published on this decomposition reaction.^{28,39,40} In the subsequent DFT calculations, we examine the reaction pathways from the initial coordinated complexes, LiO_2 or CO_4^- , to monomeric Li_2O_2 and dimeric Li_2CO_3 , which serve as the nuclei of the final discharge products. The initial LiO_2 complex can yield Li_2O_2 monomer *via* three possible pathways:

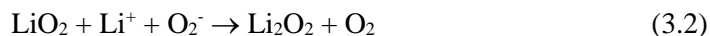
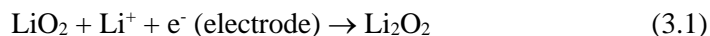


Figure 5-5 compares the energetics of these three possible pathways in DMSO (Figure 5-5a) and DME (Figure 5-5b). We find that reaction (3.1) is mostly favored over the other pathways regardless of the electrolyte ($\Delta E = -57.0$ kcal/mol for DMSO, $\Delta E = -53.4$ kcal/mol for DME). Reaction (3.2) is a downhill process only in DME (not in DMSO), where $\Delta E = -18.6$ kcal/mol for DME and $\Delta E = 3.9$ kcal/mol for DMSO. However, we note that the energy release of (3.2), even in DME, is relatively small compared to that of

(3.1). On the other hand, formation of Li_2O_2 through the dimerization of LiO_2 (3.3) is endothermic in both electrolytes: 5.6 kcal/mol in DMSO and 1.2 kcal/mol in DME electrolyte. Therefore, Li_2O_2 monomer, a seed for the Li_2O_2 crystal, is expected to be formed *via* reaction (3.1), where the cathode reduces the LiO_2 complex while simultaneously capturing a Li^+ ion from the electrolyte. This result implies that once the initial complex LiO_2 is formed, Li_2O_2 can readily form in the vicinity of the electrode, which is consistent with the previous experimental study.⁴¹

The other possible discharge product in a $\text{Li-O}_2/\text{CO}_2$ cell is Li_2CO_3 . Compared to Li_2O_2 formation, the reaction pathway for the formation of Li_2CO_3 is much more complicated because the initial complexes, Li^+ , O_2^- and CO_2 can undergo numerous possible intermediate reactions. Figure 5-6 illustrates the energetics for various reaction paths from O_2^- to Li_2CO_3 dimer in DMSO (Figure 5-6a) and DME (Figure 5-6b). The energies of all intermediate steps are calculated and shown as a colored map. For comparison, we also include the energy diagram for Li_2O_2 monomer formation along the y-axis. For simplicity, the reduction process during the incorporation of Li is depicted along the y-axis, while the corresponding process during CO_2 incorporation is depicted along the x-axis.

With regard to the incorporation of CO_2 (illustrated along the x-axis), we

considered all reduction steps are conducted by electron transfer from O_2^- referring to the previous experiment.⁴² Additionally, optimized structures of $\text{C}_2\text{O}_6^{3-}$ and $\text{C}_2\text{O}_6^{4-}$ with implicit solvation condition (produced by reduction of $\text{C}_2\text{O}_6^{2-}$, see Figure 5-7) indicate that the instability of the high charge concentration on this small molecule causes $\text{C}_2\text{O}_6^{2-}$ to dissociate *via* breakage of the peroxide bridge between the two CO_3 molecules. This results in the dissociation of $\text{C}_2\text{O}_6^{2-}$ into CO_3^- and CO_3^{2-} , followed by further reduction of these species to two CO_3^{2-} molecules, as shown in the dotted box of Figure 5-6. However, we find another pathway suggesting that the reduction of $\text{C}_2\text{O}_6^{2-}$ *via* coordination with Li^+ ions is preferred to dissociation. The electrostatic attraction between $\text{C}_2\text{O}_6^{2-}$ and Li^+ dominates over the dissociation reaction for $\text{C}_2\text{O}_6^{2-}$, which requires the injection of an additional electron into the anion. This process yields a Li_2CO_3 dimer with a structure identical to the crystal unit of Li_2CO_3 (Figure 5-8).

We find that there are indeed multiple reaction pathways that result in the formation of Li_2CO_3 because the binding of Li^+ with most anionic intermediate species is exothermic. In this respect, it is reasonable to consider the steepest descending pathway on the energy landscape as the most probable pathway in the overall reaction mechanism. The most probable reaction pathways to form Li_2CO_3 from O_2^- are displayed with

arrows in Figure 5-6 and tabulated in Table 5-2 and Table 5-3. In the reaction to form Li_2CO_3 , common pathways are generally shared in both DMSO and DME electrolytes. However, one notable difference in the most steeply descending pathways for each of the two electrolytes lies in the reduction of CO_4^- , as highlighted in Figure 5-6. In DMSO, the reduction of CO_4^- takes place with CO_2 incorporation in $\text{C}_2\text{O}_6^{2-}$, but in DME, this reduction involves Li^+ incorporation. We hypothesize that this dramatic difference arises from the difference in the dielectric behavior of two electrolytes. The high dielectric DMSO molecule allows stronger solvation of the charged species, thereby stabilizing the intermediate anion species. In contrast, the low dielectric DME molecule tends to neutralize the charged intermediates immediately due to weak solvation and charge screening. This trend is clearly observed throughout the overall reaction pathways.

Another important observation is that in the presence of CO_2 , the final discharge products may differ between the DMSO and DME systems. In DMSO, because the Li_2O_2 formation pathway is kinetically blocked at the *ICF* step, as discussed above, Li_2CO_3 is expected to be the only discharge product. In DME, formation of both Li_2O_2 and Li_2CO_3 is kinetically and thermodynamically favored. However, considering that LiO_2 formation is heavily favored compared to CO_4^- formation at the *ICF* step, we anticipate

Li_2O_2 to be a major discharge product in DME (but we note that the formation of Li_2CO_3 is unavoidable due to its thermodynamic stability, *vide supra*).

5.3.2. Experimental demonstrations for Li-O₂/CO₂ cells

To experimentally confirm the hypothesis that the dielectric property of the electrolyte influences the reaction pathway at the *ICF* step, leading to different final discharge products in Li-O₂/CO₂ batteries, we constructed Li-air (O₂/CO₂) cell systems using both DMSO and DME as electrolytes. As a reference, we constructed a Li cell using pure O₂ and compared with the results from a Li-O₂/CO₂ cell. The operation of the reference Li-O₂ cell using DMSO in Figures 5-9a and 5-9b indicates that Li_2O_2 is the major discharge product, with trace amounts of LiOH, which is consistent with previous reports.^{27,30} However, a Li-O₂/CO₂ cell using the same DMSO electrolyte clearly shows different results, shown in Figures 5-9c and 5-9d. While the discharge profile appears similar, with a comparable capacity of the reference cell, crystalline Li_2CO_3 is formed after the first discharge in the O₂/CO₂ mixed gas system. This stands in striking contrast to the conventional Li-O₂ cells, which produce only Li_2O_2 as a discharge product. Moreover, we find that the morphology of the discharge product in the Li-

O₂/CO₂ cell is clearly different from that in the Li-O₂ cell. The discharge products in the Li-O₂/CO₂ cell grow in a flake-like shape with a preferred orientation, as shown in the inset of Figure 5-9c; however, the Li-O₂ cell (as shown in the inset of Figure 5-9a) produces discharge products without a particular shape, consistent with previous reports.^{23,27,37} It should also be noted that the discharge potential is slightly higher (by 0.1 V) in the Li-O₂/CO₂ cell; this will be discussed in further detail later in this manuscript.

GITT measurements also indicate that the reaction mechanism and final products are different in the presence of CO₂. As shown in Figure 5-10, after a full relaxation of the potential ($dV/dt: \sim 3.38 \times 10^{-6} \text{ V s}^{-1}$), the equilibrium potential of Li-O₂ cell (blue) reaches a value near 2.9 V regardless of the state of charge (SOC). This value compares well with the DFT formation potential of the major discharge product, Li₂O₂, which is 2.96 V.^{1,43} In contrast, identical GITT measurements on the Li-O₂/CO₂ cell (red) show that the equilibrium potential is substantially higher, ~ 3.3 V. While comparing the open-circuit voltage does not provide direct evidence for Li₂CO₃ formation, it is noteworthy that the formation potential of Li₂CO₃ is 3.82 V, which is higher than that of Li₂O₂. These values are comparable to our DFT results for the calculated formation potentials of 2.90 V to yield Li₂O₂ and 3.81 V to yield Li₂CO₃, respectively (refer to the footnotes of Tables 5-2 and 5-4).

Identical experiments on Li-O₂ and Li-O₂/CO₂ cells were performed in the DME electrolyte. For the reference Li-O₂ cell with DME, Figures 5-11a and b clearly show the formation of crystalline Li₂O₂ after the discharge process, in agreement with previous experimental reports.^{28,44} However, for the Li-O₂/CO₂ cell, we found that the discharge process deposits an amorphous product. XRD could not identify the phase of this product, but FT-IR revealed that the discharge product was a mixture of Li₂O₂ and Li₂CO₃ (the inset of Figure 5-11d). Despite the similar intensity of the IR peaks for Li₂O₂ and Li₂CO₃, we cannot conclude that the quantities of both products present are comparable to each other because IR data are largely dependent on the composition of the surface, and Li₂O₂ can readily absorb CO₂ under CO₂-rich conditions, resulting in partial conversion of Li₂O₂ into Li₂CO₃ at the surface region.

Although there is no obvious way to characterize the major final discharge product when DME electrolyte is used, we can obtain some valuable information regarding the major products by examining the difference in discharge capacities presented in Figures 5-11a and 5-11c, which show that the discharge capacity of the Li-O₂/CO₂ cell is half that of the Li-O₂ cell. Assuming that the activities of O₂ and CO₂ are comparable, the discharge capacity of the Li-O₂ and the Li-O₂/CO₂ cells should be similar, even though

the discharge products are different (Li_2O_2 vs. Li_2CO_3). However, given that the partial pressure ratio of O_2 and CO_2 is 1:1, our observation that the capacity of the $\text{Li-O}_2/\text{CO}_2$ cell is reduced by half allows us to deduce that CO_2 is significantly less electrochemically active compared to O_2 . Thus, primarily Li_2O_2 is formed during the discharge process. In additional experiments using different ratios of O_2 and CO_2 (Figure 5-12), we confirmed that the overall discharge capacity is proportional to the partial pressure of oxygen in DME.^{33,34} In contrast, in the case of DMSO, discharge capacity remains essentially constant regardless of the oxygen partial pressure because CO_2 is electrochemically active, and therefore, contributes equally to the capacity. Thus, it is quite reasonable to consider Li_2O_2 as the major initial discharge product in DME, which is in excellent agreement with our DFT predictions.

Even though the particle morphology does not provide direct evidence of particular phases, the growth behavior can provide additional information regarding the phase identity. As shown in the insets of Figures 5-11a and c, the morphologies of the discharge products in DME are macroscopically similar. This is in clear contrast with the case of DMSO, where the morphologies of the discharge products were notably different between the Li-O_2 cell and the $\text{Li-O}_2/\text{CO}_2$ cell. The similar morphological characteristic

of discharge products was attributed to the comparable discharge processes of Li-O₂ and Li-O₂/CO₂ cells in DME.

As previously mentioned, based on the relative formation energies of Li₂O₂ and Li₂CO₃ and as demonstrated using our Li-O₂/CO₂ cells with DME, the partial formation of Li₂CO₃ is inevitable in the presence of CO₂. Consequently, for the development of secondary Li-air batteries, it is important to preserve the electrochemical decomposability of Li₂CO₃. Thus, we further investigated the possibility of a rechargeable Li-O₂/CO₂ battery using DMSO as an electrolyte, based on the reversible formation and decomposition of Li₂CO₃.

As shown in Figure 5-13a, the first discharge/charge profile of the Li-O₂/CO₂ cell is notably different from that of the conventional Li-O₂ cell. The operating potential of the Li-O₂/CO₂ cell (red) is slightly higher than that of the conventional Li-O₂ cell (blue), which we attribute to the greater formation energy of Li₂CO₃ compared to Li₂O₂. The three steps observed in the charge profile of the Li-O₂ cell are consistent with previous results, based on the decomposition of Li₂O₂.^{28,37,38} We note that the flat charge potential observed experimentally near 4.2 V in the Li-O₂/CO₂ cell corresponds to the potential for Li₂CO₃ decomposition in a Li-O₂ cell using a carbonate-based electrolyte.^{28,39} The distinguishable electrochemical profiles of both cells

again provide support for the differing reaction chemistry in Li-air cells depending on the constituents of the gas.

The XRD analysis of the Li-O₂/CO₂ cell, presented in Figure 5-13b, demonstrates that the discharge product, Li₂CO₃, is decomposed reversibly by an electrochemical oxidation process under 4.5 V, which demonstrates that the high dielectric medium of DMSO can be effective in electrochemically activating CO₂. This suggests that a rechargeable battery based on Li₂CO₃ chemistry is feasible. At this point, we note that production of Li₂CO₃ has resulted from the input of CO₂ into the Li-air cell, not from the decomposition of electrolyte that is commonly observed in Li-air cells that use carbonate-based electrolytes.^{15,29}

The rechargeability of the Li-O₂/CO₂ cell, based on the chemistry of Li₂CO₃, was further tested, as shown in Figures 5-13c and d. The cells were operated with capacity-limited cycling, which is presently often used to investigate the cyclability of Li-air batteries.^{13,45,46} Quite interestingly, prolonged cycles without any catalysts or additives show a stable reversible reaction. We note that this is an outstanding result compared to previous reports based on Li-O₂ cells using carbonate-type electrolytes (where serious electrolyte decomposition deteriorates the cell cyclability) or even compared with the Li-O₂ cell using DMSO electrolyte (where byproducts, such as

LiOH, can be produced continuously over many cycles^{27,30}). Indeed, our analysis of the final product shows that there is only a single discharge product, Li_2CO_3 , without any other byproducts, such as LiOH. We expect that the outstanding thermodynamic stability of Li_2CO_3 minimizes the possibility of side reactions, leading to the enhanced cyclability of these systems. This also suggests that reaction design to inhibit the formation of LiOH should be the next advance made in the development of practical Li-air batteries.

5.4. Conclusion

To further progress toward their practical application, Li-air batteries must be operated in an ambient air environment consisting of O₂, CO₂, N₂, etc. Thus, in this study, we investigated the effect of CO₂, the gas component of ambient air that most influences the chemistry of Li-air cells. On the basis of quantum mechanical (QM) calculations coupled with experiments, we described the reaction chemistry of a Li-‘air’ cell consisting of Li, O₂, and CO₂ during the initial stage of battery operation. We found that the electrolyte solvation effect can be useful for leveraging the reaction pathway at the *initial complex formation (ICF)* step by altering the potential energy surface, which is predicted to change the final discharge product of the Li-air cell. Indeed, our experimental results from a Li-O₂/CO₂ cell showed that the high dielectric DMSO favors electrochemical activation of CO₂ to form Li₂CO₃, while the low dielectric DME tends to form Li₂O₂ as a major discharge product, consistent with the theoretical investigations.

Furthermore, we determined, for the first time, that the electrochemical activation of CO₂ within the high dielectric medium of DMSO enables the reversible formation of Li₂CO₃ instead of Li₂O₂. This is of vital importance because the superior thermodynamic stability of Li₂CO₃ leads to its

formation being unavoidable in an environment containing CO₂. Moreover, the realization of cell cycling based on the stability of Li₂CO₃ seems to help attain a more stable cyclability for Li-air cells.

Based on our systematic investigation of the reaction chemistry of CO₂ within a Li-air battery cell combined with the idea of “reaction pathway leveraging using dielectric media”, we suggest that the use of a high dielectric electrolyte may help to preserve the reversible reaction of Li₂CO₃ by electrochemically activating CO₂. However, we should note that the electrolytes with the highest dielectric constants are usually either protic or carbonate-type; the former is not suitable for Li-ion chemistry and the latter has stability problems. Thus, DMSO might be optimal. In addition, our findings might further open up the new possibility for a novel rechargeable Li-O₂/CO₂ battery based on the single discharge product of Li₂CO₃, which has proven advantageous with regard to cyclability.

Solvent	ϵ	Probe radii, R (Å)	Viscosity (cP)	Solubility (mM)	
				O ₂	CO ₂
Ethylene carbonate ^{47,48}	89.6	2.36	1.90	N/A	85.0
Dimethyl sulfoxide ²⁰	47.2	2.41	1.95	2.1	125.0
Dimethoxyethane ³³	7.2	2.77	0.46	9.6	N/A

* All properties are measured at 25°C except for ethylene carbonate (40°C)

Table 5-1. Physical properties of selected electrolytes

Elementary Reaction	Reaction Energy (kcal/mol)
$4\text{O}_2 + 4\text{e}^- (\text{electrode}) \rightarrow 4\text{O}_2^-$	-61.0 x 4
$\text{O}_2^- + \text{CO}_2 \rightarrow \text{CO}_4^-$	-1.6
$\text{CO}_4^- + \text{O}_2^- \rightarrow \text{CO}_4^{2-} + \text{O}_2$	-9.9
$\text{CO}_4^{2-} + \text{CO}_2 \rightarrow \text{C}_2\text{O}_6^{2-}$	-17.4
$\text{C}_2\text{O}_6^{2-} + \text{Li}^+ \rightarrow \text{LiC}_2\text{O}_6^-$	+0.9
$\text{LiC}_2\text{O}_6^- + \text{O}_2^- \rightarrow \text{LiC}_2\text{O}_6^{2-} + \text{O}_2$	-16.1
$\text{LiC}_2\text{O}_6^{2-} + \text{O}_2^- \rightarrow \text{LiC}_2\text{O}_6^{3-} + \text{O}_2$	-27.3
$\text{LiC}_2\text{O}_6^{3-} + \text{Li}^+ \rightarrow \text{Li}_2\text{C}_2\text{O}_6^{2-}$	-12.5
$\text{Li}_2\text{C}_2\text{O}_6^{2-} + \text{Li}^+ \rightarrow \text{Li}_3\text{C}_2\text{O}_6^-$	-4.1
$\text{Li}_3\text{C}_2\text{O}_6^- + \text{Li}^+ \rightarrow (\text{Li}_2\text{CO}_3)_2$	-6.3
$(\text{Li}_2\text{CO}_3)_2 (\text{soln.}) \rightarrow (\text{Li}_2\text{CO}_3)_2 (\text{gas})$	106.05
$(\text{Li}_2\text{CO}_3)_2 (\text{gas}) \rightarrow \text{Li}_2\text{CO}_3 (\text{cryst.})$	-119.42 ^a
Overall: $\text{O}_2 + 2\text{CO}_2 + 4\text{Li}^+ + 4\text{e}^- \rightarrow (\text{Li}_2\text{CO}_3)_2$	-351.22^b

Table 5-2. Most probable reaction pathway for Li_2CO_3 formation using DMSO electrolyte, as determined from DFT calculations

^a Calculated using periodic density functional theory method implemented in Vienna Ab-initio Software Package (VASP) with PBE functional.

^b Using the Nernst equation, $\Delta E = -nFV$, the value can be converted into the reduction potential (V) of 3.81 V, where F is the Faraday constant and n=4.

Elementary Reaction	Reaction Energy (kcal/mol)
$4\text{O}_2 + 4\text{e}^- (\text{electrode}) \rightarrow 4\text{O}_2^-$	-34.8×4
$\text{O}_2^- + \text{CO}_2 \rightarrow \text{CO}_4^-$	-4.2
$\text{CO}_4^- + \text{Li}^+ \rightarrow \text{LiCO}_4$	-16.3
$\text{LiCO}_4 + \text{O}_2^- \rightarrow \text{LiCO}_4^- + \text{O}_2$	-22.9
$\text{LiCO}_4^- + \text{Li}^+ \rightarrow \text{Li}_2\text{CO}_4$	-17.7
$\text{Li}_2\text{CO}_4 + \text{CO}_2 \rightarrow \text{Li}_2\text{C}_2\text{O}_6$	-7.4
$\text{Li}_2\text{C}_2\text{O}_6 + \text{O}_2^- \rightarrow \text{Li}_2\text{C}_2\text{O}_6^- + \text{O}_2$	-31.7
$\text{Li}_2\text{C}_2\text{O}_6^- + \text{Li}^+ \rightarrow \text{Li}_3\text{C}_2\text{O}_6$	-22.0
$\text{Li}_3\text{C}_2\text{O}_6 + \text{O}_2^- \rightarrow \text{Li}_3\text{C}_2\text{O}_6^- + \text{O}_2$	-31.9
$\text{Li}_3\text{C}_2\text{O}_6^- + \text{Li}^+ \rightarrow (\text{Li}_2\text{CO}_3)_2$	-25.0
$(\text{Li}_2\text{CO}_3)_2 (\text{soln.}) \rightarrow (\text{Li}_2\text{CO}_3)_2 (\text{gas})$	84.98
$(\text{Li}_2\text{CO}_3)_2 (\text{gas}) \rightarrow \text{Li}_2\text{CO}_3 (\text{cryst.})$	-119.42 ^a
Overall: $\text{O}_2 + 2\text{CO}_2 + 4\text{Li}^+ + 4\text{e}^- \rightarrow (\text{Li}_2\text{CO}_3)_2$	-352.74 ^b

Table 5-3. Most probable reaction pathway for Li_2CO_3 formation using DME electrolyte, as determined from DFT calculations

^a Calculated using periodic density functional theory method implemented in Vienna Ab-initio Software Package (VASP) with PBE functional.

^b Using the Nernst equation, $\Delta E = -nFV$, the value can be converted into the reduction potential (V) of 3.82 V, where F is the Faraday constant and $n=4$.

Elementary Reaction	Reaction Energy (kcal/mol)	
	DMSO	DME
$\text{O}_2 + \text{e}^- (\text{electrode}) \rightarrow \text{O}_2^-$	-61.0	-34.8
$\text{O}_2^- + \text{Li}^+ \rightarrow \text{LiO}_2$	-1.6	-19.8
$\text{LiO}_2 + \text{e}^- (\text{electrode}) \rightarrow \text{LiO}_2^-$	-47.4	-19.7
$\text{LiO}_2^- + \text{Li}^+ \rightarrow (\text{Li}_2\text{O}_2)_1$	-9.7	-33.7
$(\text{Li}_2\text{O}_2)_1 (\text{soln.}) \rightarrow (\text{Li}_2\text{O}_2)_1 (\text{gas})$	64.46	51.81
$(\text{Li}_2\text{O}_2)_1 (\text{gas}) \rightarrow \text{Li}_2\text{O}_2 (\text{cryst.})^a$	-78.57	-78.57
Overall: $\text{O}_2 + 2\text{Li}^+ + 2\text{e}^- \rightarrow (\text{Li}_2\text{O}_2)_1$	-133.804^b	-134.755^c

Table 5-4. Most probable reaction pathway for Li_2O_2 formation using DMSO and DME electrolytes

^a Calculated using periodic density functional theory method implemented in Vienna Ab-initio Software Package (VASP) with PBE functional.

^b Using Nernst equation of $\Delta E = -nFV$, the value can be converted into the reduction potential (V) of 2.90 V, where F is the Faraday constant and $n=2$.

^c Using Nernst equation of $\Delta E = -nFV$, the value can be converted into the reduction potential (V) of 2.92 V, where F is the Faraday constant and $n=2$.

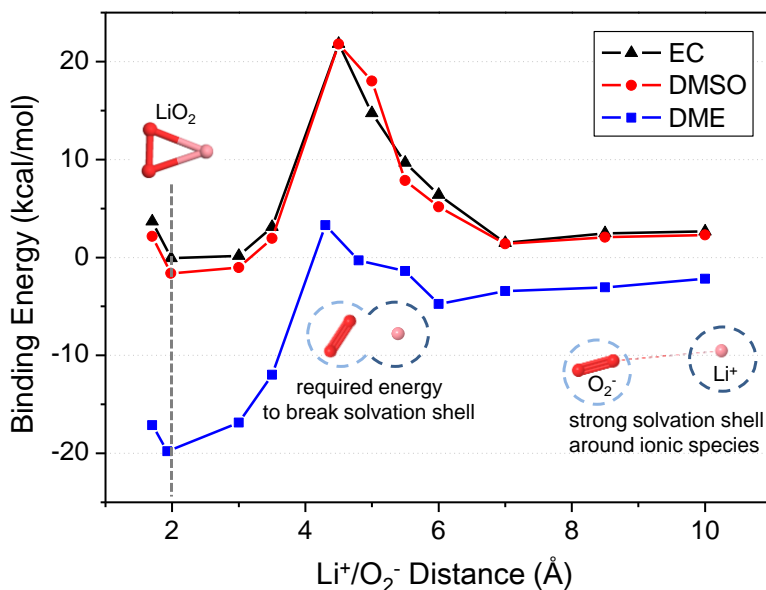
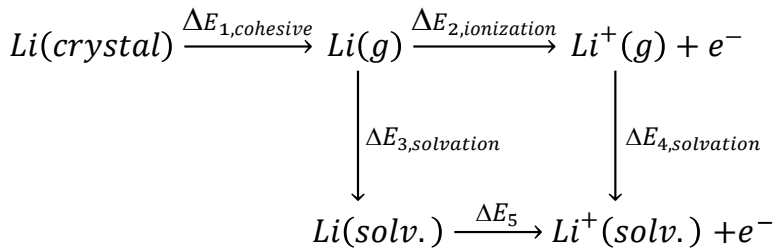


Figure 5-1. Binding energy trend of relaxed coordinate scan between O_2^- and Li^+ under Poisson-Boltzmann solvation model within EC (triangle, black), DMSO (circle, red) and DME (square, blue).

Because of the strong Coulombic interaction between ionic species, the binding energy trend of O_2^- with Li^+ in gas phase along with the distance is substantial downhill process with no activation barrier. The activation barrier is determined by choosing highest energy from relaxed coordinate scan energies under implicit solvation model. Activation barrier can be referred as the factor solely that comes from solvation effect.

[Reference energy calculation of electron]

Quantum mechanical energy of electron is basically “0” value. However, considering the source of electron in Li-air battery system, some amount of energy is always required to generate electron from counter electrode. To calculate reasonable energy changes of reaction which is including electron, we have to take account of energy cost to dissolve a Li⁺ into the electrolyte from Li solid. Calculation detail is as follows.



*Required energy to generate electron

$$\begin{aligned}
 \Delta E_{\text{electron}} &= \Delta E_1 + \Delta E_3 + \Delta E_5 \\
 &= \Delta E_1 + \Delta E_3 + (\Delta E_2 - \Delta E_3 + \Delta E_4) \\
 &= \Delta E_1 + \Delta E_2 + \Delta E_4
 \end{aligned}$$

(kcal/mol)	ΔE_1	ΔE_2	ΔE_3	ΔE_4	ΔE_5	$\Delta E_{\text{electron}}$
EC	39.0 ¹	129.6	0.0	-135.7	-6.1	32.9
DMSO				-134.4	-4.8	34.2
DME				-118.1	11.5	50.5

(1) Silverman, R. A. et al. *Phys. Rev.* **1950**, *80*, 912

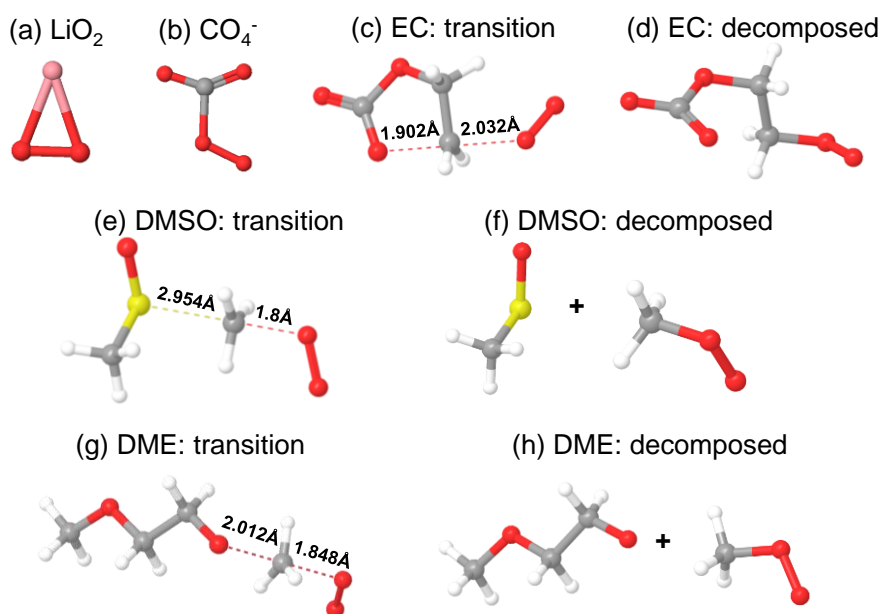


Figure 5-2. Structures of chemical species which are derived by initial reaction step with O_2^- ; (a) $\text{O}_2 + \text{Li}^+ \rightarrow \text{LiO}_2$, (b) $\text{O}_2^- + \text{CO}_2 \rightarrow \text{CO}_4^-$, transition and decomposed state of EC (c and d), DMSO (e and f) and DME (g and h). (Atomic species: red-O, pink-Li, grey-C, white-H, yellow-S)

In case of EC, above decomposed structure (d) is not final decomposition state but intermediate state which is going to be decomposed further to CO_2 and lithium carbonate complexes.² Decomposition states of DMSO and DME are referred from previous research.³

(2) Freunberger, S. A. et al. *J. Am. Chem. Soc.* **2011**, 133, 8040

(3) Bryantsev, V. S. et al. *J. Phys. Chem. A.* **2011**, 115, 12399

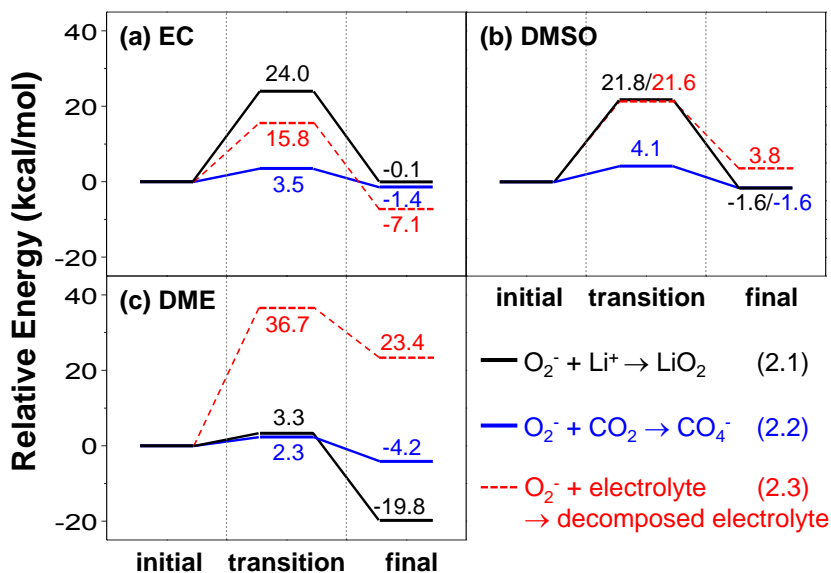


Figure 5-3. Activation barrier and binding reaction energy from DFT calculations at the *initial complex formation (ICF)* step, during which O_2^- is coordinating with Li^+ (black), CO_2 (blue) and electrolyte (red) using (a) EC (b) DMSO, (c) DME electrolytes. To evaluate the activation barrier of the LiO_2 complex, which without solvation is a barrier-less downhill reaction, we scanned the reaction coordinate under an implicit solvation environment, with the maximum value determining the height of barrier.

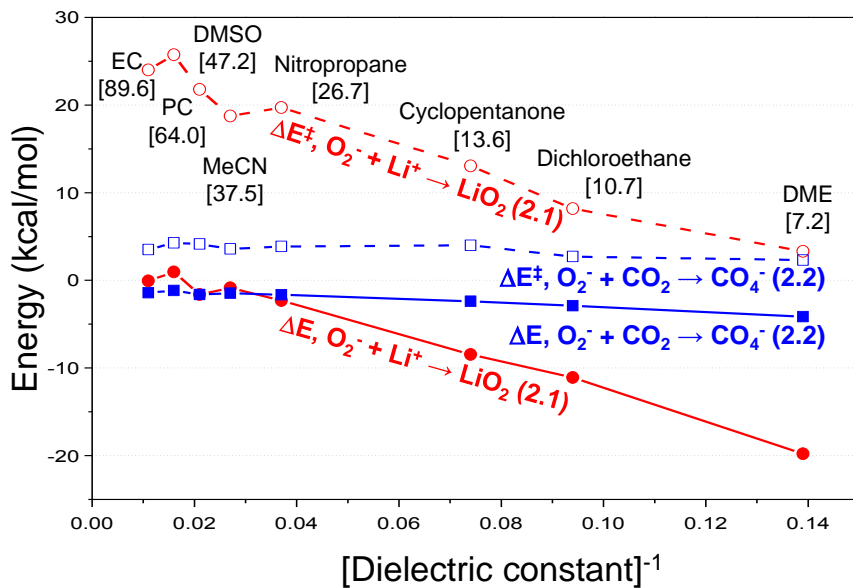


Figure 5-4. DFT predicted trend of activation barrier (ΔE^\ddagger , dashed) and binding reaction energy (ΔE , solid) plotted against $[\text{dielectric constant}]^{-1}$ for the *initial complex formation (ICF)* steps of reaction (2.1) and reaction (2.2), forming LiO_2 (red, circle) and CO_4^- (blue, square), respectively. The values enclosed in brackets are the dielectric constants of various solvents.

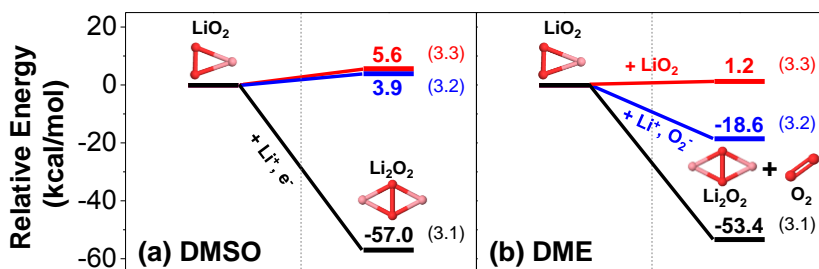


Figure 5-5. DFT relative energy changes from LiO_2 to Li_2O_2 for three possible reaction pathways using (a) DMSO and (b) DME electrolytes. Energies shown are for the direct reduction reaction (3.1) by electron transfer from electrode, for reduction by electron transfer from O_2^- (3.2), and for the dimerization of LiO_2 (3.3). The direct reduction reaction (3.1) is the most favored.

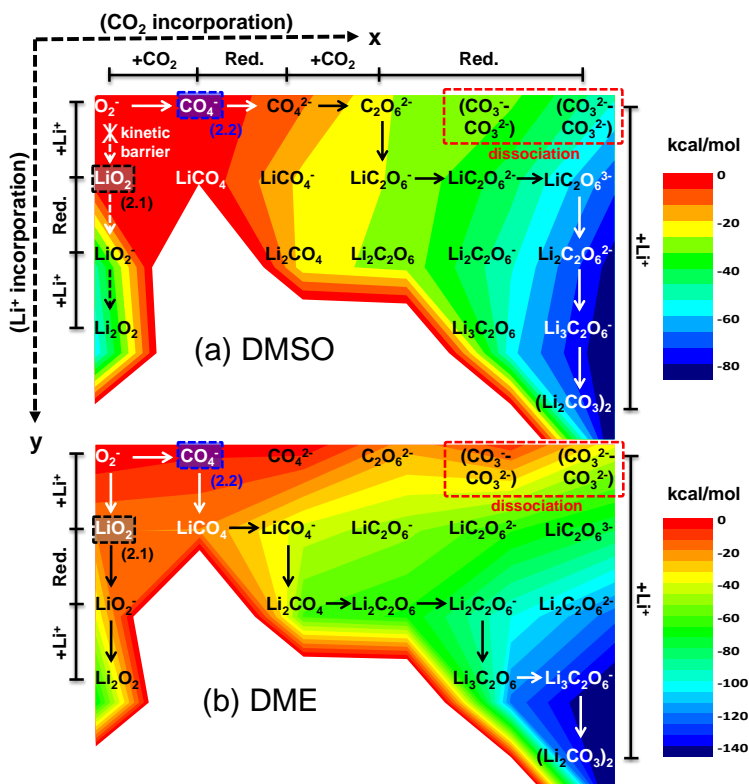


Figure 5-6. Two-dimensional energy surface map including every possible intermediate species from the dioxygen anion radical of O₂⁻ (formed after ORR reaction) to (Li₂O₂)₁ and (Li₂CO₃)₂ using DME and DMSO electrolytes. The most favorable reaction pathways to form the final products (the steepest descending pathways on the energy surface) are denoted using arrows.

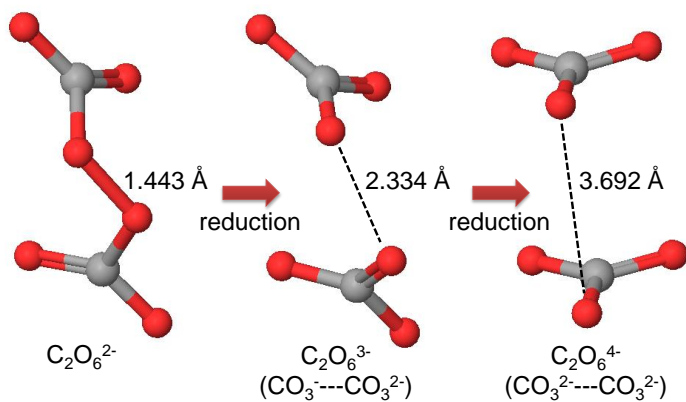


Figure 5-7. Detailed structures of dissociation process from $C_2O_6^{2-}$ to $(CO_3^{2-} \cdots CO_3^{2-})$ by reduction under DMSO implicit solvation model.

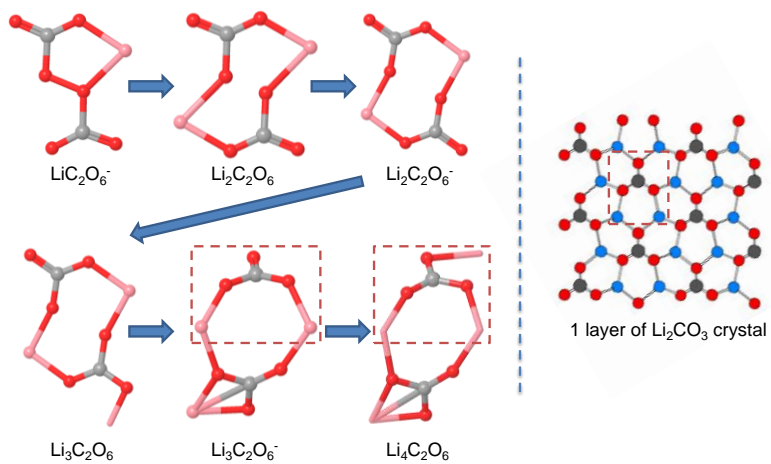


Figure 5-8. Reduction processes which include Li^+ effect from $\text{C}_2\text{O}_6^{2-}$ to $\text{C}_2\text{O}_6^{4-}$ under DMSO implicit solvation model. Result structure has same topology with basic unit of actual Li_2CO_3 crystal.

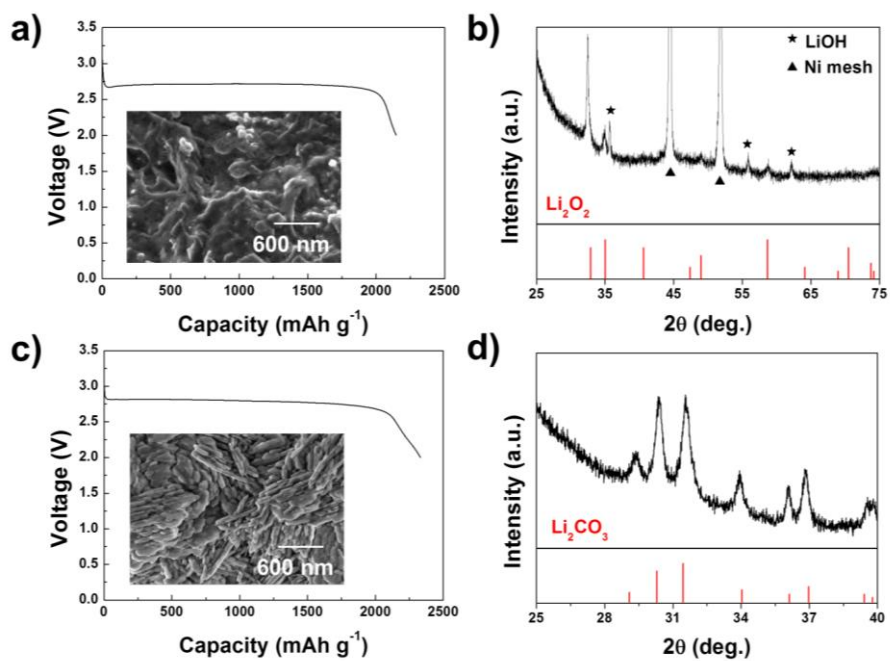


Figure 5-9. Electrochemical properties, SEM images, and XRD results of (a, b) a Li-O₂ cell and (c, d) a Li-O₂/CO₂ cell with DMSO electrolyte.

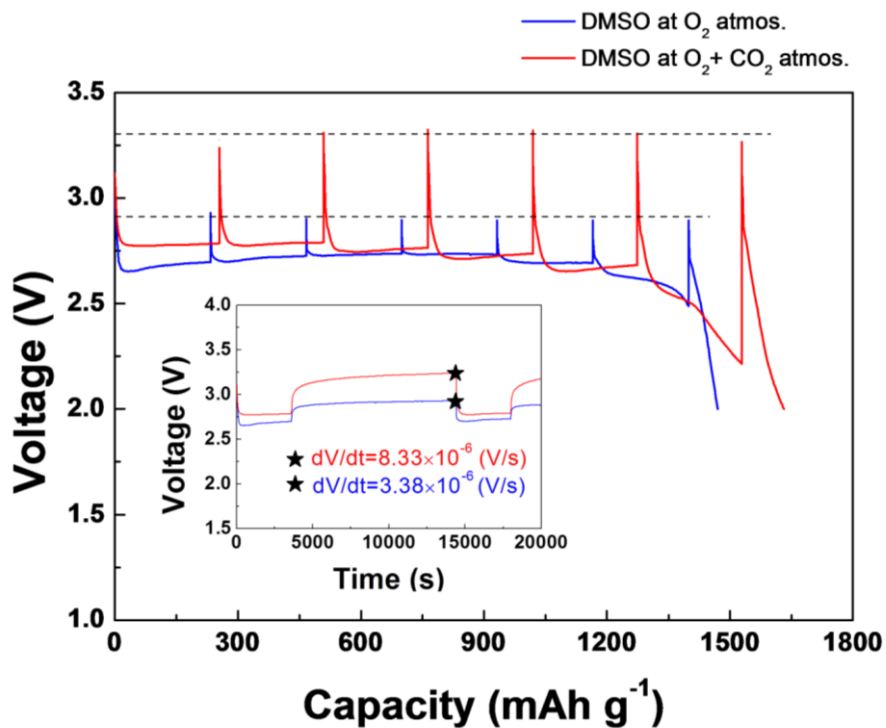


Figure 5-10. GITT discharge voltage profile obtained for a Li-O₂ cell (blue) and a Li-O₂/CO₂ cell (red) with DMSO electrolyte (inset: the potential vs. time plot). The inset shows that the relaxation time is sufficient for each cell.

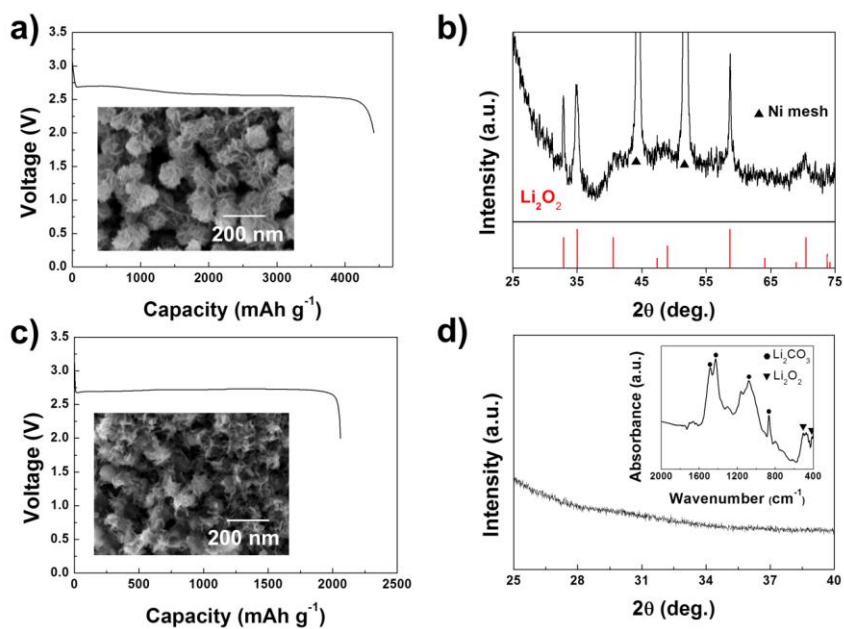


Figure 5-11. Electrochemical properties, SEM images, and XRD results of (a, b) a Li-O₂ cell and (c, d) a Li-O₂/CO₂ cell with DME electrolyte.

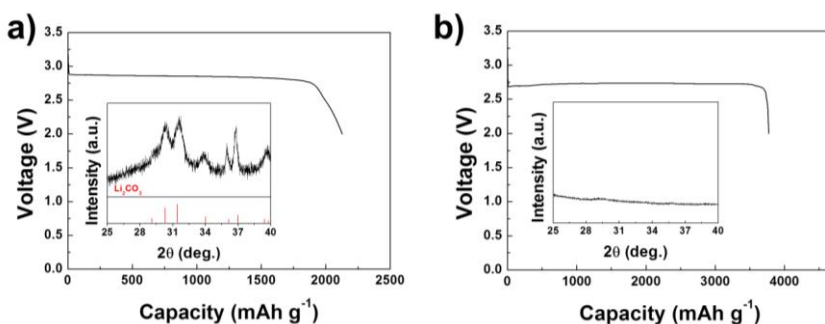


Figure 5-12. Electrochemical properties and XRD results of Li-O₂/CO₂ cells with (a) DMSO electrolyte and (b) DME electrolyte at a 9:1 pressure ratio of O₂ and CO₂.

Since the actual air condition always has a relatively lower CO₂ concentration than O₂, we further investigate the effect of CO₂ incorporation in an oxygen rich condition, which is closer to the ambient air condition. While the total outer pressure of 770 Torr is constantly maintained, the partial pressure ratio of O₂ and CO₂ is controlled at 9:1. Interestingly, the Li-O₂/CO₂ cell with DMSO electrolyte in Figure 5-12a shows very similar reaction profile with Figure 5-9c, which implies that the CO₂ incorporation could be activated even in a relatively low CO₂ concentration. The final discharge product of Li₂CO₃ is also solely detected. In comparison, amorphous phase of discharge products were formed in DME electrolyte (Figure 5-12b), which is very similar case with the cell at 1:1 ratio of gases

as in case of Figure 5-11d. The discharge products are Li_2O_2 and Li_2CO_3 from the FT-IR results (data not shown here). The discharge capacity has increased compared to the cell of $\text{O}_2:\text{CO}_2 = 1:1$ ratio indicating that the overall discharge capacity is proportional to the partial pressure of oxygen in DME unlike the case of DMSO. This result is quite meaningful because it is revealed that CO_2 can greatly affect on the cell performance, even in the CO_2 deficiency atmosphere and it also suggest that we have to consider the effect of CO_2 incorporation in further designing of Li-air cells operated in an ambient air system.

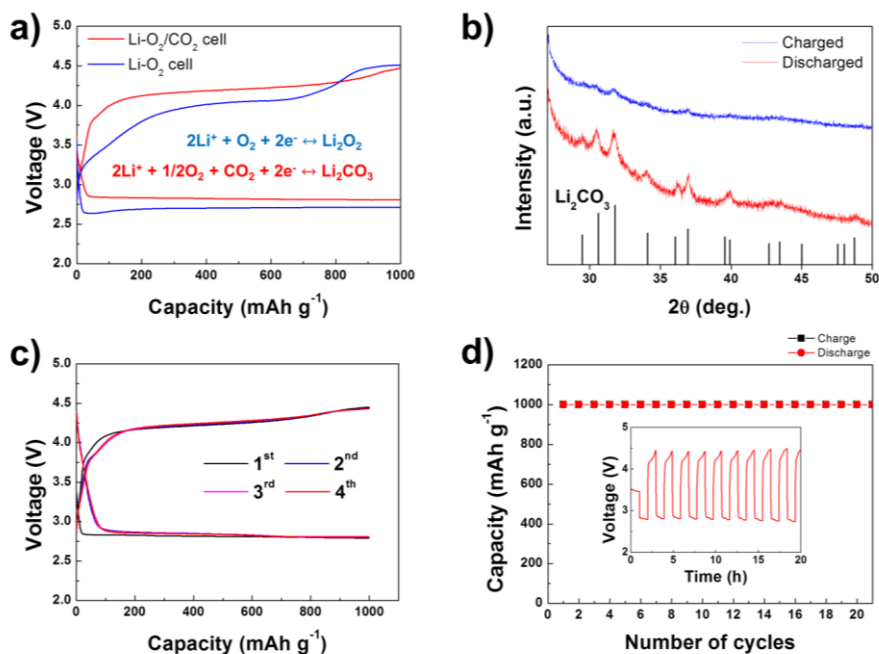


Figure 5-13. (a) The first discharge/charge profiles in each system with DMSO electrolyte, (b) XRD patterns after discharge and charge of the Li-O₂/CO₂ cell with DMSO electrolyte, (c) the initial 4 cycle profiles and (d) the related cyclability of the Li-O₂/CO₂ cell, utilized up to 1000 mAh g⁻¹ at a constant rate of 0.4 mA cm⁻².

5.5. References

1. P. G. Bruce, S. A. Freunberger, L. J. Hardwick, J.-M. Tarascon, *Nat. Mater.* **2012**, *11*, 19-29.
2. M. Leskes, N. E. Drewett, L. J. Hardwick, P. G. Bruce, G. R. Goward, C. P. Grey, *Angew. Chem.* **2012**, *124*, 8688-8691.
3. R. Black, S. H. Oh, J.-H. Lee, T. Yim, B. Adams and L. F. Nazar, *J. Am. Chem. Soc.* **2012**, *134*, 2902-2905.
4. P. Hartmann, C. L. Bender, M. Vračar, A. K. Dürr, A. Garsuch, J. Janek and P. Adelhelm, *Nat. Mater.*, **2012**, *12*, 228–232.
5. Y. Li, J. Wang, X. Li, J. Liu, D. Geng, J. Yang, R. Li, X. Sun, *Electrochem. Commun.* **2011**, *13*, 668-672.
6. Z.-L. Wang, D. Xu, J.-J. Xu, L.-L. Zhang, X.-B. Zhang, *Adv. Funct. Mater.* **2012**, *22*, 3699-3705.
7. S. H. Oh, L. F. Nazar, *Adv. Energy Mater.* **2012**, *2*, 903-910.
8. S. A. Freunberger, Y. Chen, N. E. Drewett, L. J. Hardwick, F. Bardé, P. G. Bruce, *Angew. Chem.* **2011**, *50*, 8609-8613.
9. A. Débart, A. J. Paterson, J. Bao, P. G. Bruce, *Angew. Chem.* **2008**, *120*, 4597-4600.
10. H.-D. Lim, K.-Y. Park, H. Song, E. Y. Jang, H. Gwon, J. Kim, Y. H. Kim, M. D. Lima, R. O. Robles, X. Lepró, R. H. Baughman and K. Kang, *Adv. Mater.* **2013**, *25*, 1348-1352.
11. J.-L. Shui, N. K. Karan, M. Balasubramanian, S.-Y. Li, D.-J. Liu, *J. Am. Chem. Soc.* **2012**, *134*, 16654-16661.
12. K.-N. Jung, J.-I. Lee, W. B. Im, S. Yoon, K.-H. Shin, J.-W. Lee, *Chem. Commun.* **2012**, *48*, 9406-9408.

13. H.-D. Lim, K.-Y. Park, H. Gwon, J. Hong, H. Kim, K. Kang, *Chem. Commun.* **2012**, 48, 8374-8376.
14. X. Lin, L. Zhou, T. Huang, A. Yu, *J. Mater. Chem. A* **2013**, 1, 1239-1245.
15. Y. Li, J. Wang, X. Li, D. Geng, M. N. Banis, Y. Tang, D. Wang, R. Li, T.-K. Sham, X. Sun, *J. Mater. Chem.* **2012**, 22, 20170-20174.
16. Y. Cui, Z. Wen, X. Liang, Y. Lu, J. Jin, M. Wu, X. Wu, *Energy Environ. Sci.* **2012**, 5, 7893-7897.
17. S. C. Nam, Y. S. Yoon, W. I. Cho, B. W. Cho, H. S. Chun, K. S. Yun, *J. Electrochem. Soc.* **2001**, 148, A220-A223.
18. J. A. Dean, In *Lange's Handbook of Chemistry*; 12th Ed. ed.; McGraw-Hill: New York, **1979**; Vol. 9, p 4.
19. J. Christensen, P. Albertus, R. S. Sanchez-Carrera, T. Lohmann, B. Kozinsky, R. Liedtke, J. Ahmed, A. J. Kojic, *Electrochem. Soc.* **2012**, 159, R1.
20. J. D. Wadhawan, P. J. Welford, E. Maisonhaute, V. Climent, N. S. Lawrence, R. G. Compton, H. B. McPeak, C. E. W. Hahn, *J. Phys. Chem. B* **2001**, 105, 10659-10668.
21. K. Takechi, T. Shiga, T. Asaoka, *Chem. Commun.* **2011**, 47, 3463-3465.
22. S. R. Gowda, A. Brunet, G. M. Wallraff, B. D. McCloskey, *J. Phys. Chem. Lett.* **2012**, 276-279.
23. Suite 2012: Jaguar version 7.9, S., LLC, New York, NY, **2012**.
24. A. D. Becke, *J. Chem. Phys.* **1993**, 98, 5648-5652.
25. C. T. Lee, W. T. Yang, R. G. Parr, *Phys. Rev. B* **1988**, 37, 785-789.
26. P. C. Harihara, J. A. Pople, *Chem. Phys. Lett.* **1972**, 16, 217-219.

27. D. Xu, Z.-l. Wang, J.-j. Xu, L.-l. Zhang, X.-b. Zhang, *Chem. Commun.* **2012**, 48, 6948-6950.
28. B. D. McCloskey, D. S. Bethune, R. M. Shelby, G. Girishkumar, A. C. Luntz, *J. Phys. Chem. Lett.* **2011**, 2, 1161-1166.
29. H. Wang, K. Xie, *Electrochim. Acta* **2012**, 64, 29-34.
30. D. Xu, Z.-l. Wang, J.-j. Xu, L.-l. Zhang, L.-m. Wang, X.-b. Zhang, *Chem. Commun.* **2012**, 48, 11674-11676.
31. D. J. Tannor, B. Marten, R. Murphy, R. A. Friesner, D. Sitkoff, A. Nicholls, M. Ringnalda, W. A. Goddard, B. Honig, *J. Am. Chem. Soc.* **1994**, 116, 11875-11882.
32. B. Marten, K. Kim, C. Cortis, R. A. Friesner, R. B. Murphy, M. N. Ringnalda, D. Sitkoff, B. Honig, *J. Phys. Chem.-Us* **1996**, 100, 11775-11788.
33. C. O. Laoire, S. Mukerjee, K. M. Abraham, E. J. Plichta, M. A. Hendrickson, *J. Phys. Chem. C* **2010**, 114, 9178-9186.
34. J. Hassoun, F. Croce, M. Armand, B. Scrosati, *Angew. Chem.* **2011**, 50, 2999-3002.
35. J. Hassoun, H.-G. Jung, D.-J. Lee, J.-B. Park, K. Amine, Y.-K. Sun, B. Scrosati, *Nano Lett.* **2012**, 12, 5775-5779.
36. V. S. Bryantsev, V. Giordani, W. Walker, M. Blanco, S. Zecevic, K. Sasaki, J. Uddin, D. Addison, G. V. Chase, *J. Phys. Chem. A* **2011**, 115, 12399-12409.
37. D. Xu, Z.-l. Wang, J.-j. Xu, L.-l. Zhang, L.-m. Wang, X.-b. Zhang, *Chem. Commun.* **2012**, 48, 11674-11676.
38. C. O. Laoire, S. Mukerjee, E. J. Plichta, M. A. Hendrickson, K. M. Abraham, *J. Electrochem. Soc.* **2011**, 158, A302-A308.
39. S. A. Freunberger, Y. Chen, Z. Peng, J. M. Griffin, L. J. Hardwick,

- F. Bardé, P. Novák, P. G. Bruce, *J. Am. Chem. Soc.* **2011**, *133*, 8040-8047.
40. Z. Zhang, J. Lu, R. S. Assary, P. Du, H. H. Wang, Y. K. Sun, Y. Qin, K. C. Lau, J. Greeley, P. C. Redfern, H. Iddir, L. A. Curtiss, K. Amine, *J. Phys. Chem. C* **2011**, *115*, 25535-25542.
41. J. S. Hummelshøj, J. Blomqvist, S. Datta, T. Vegge, J. Rossmeisl, K. S. Thygesen, A. C. Luntz, K. W. Jacobsen, J. K. Nørskov, *J. Chem. Phys.* **2010**, *132*, 071101.
42. W. J. Albery, D. Clark, H. J. J. Drummond, A. J. M. Coombs, W. K. Young, C. E. W. Hahn, *J. Electroanal. Chem.* **1992**, *340*, 99-110.
43. J. Hassoun, F. Croce, M. Armand, B. Scrosati, *Angew. Chem.* **2011**, *50*, 2999-3002.
44. B. D. McCloskey, A. Speidel, R. Scheffler, D. C. Miller, V. Viswanathan, J. S. Hummelshøj, J. K. Nørskov, A. C. Luntz, *J. Phys. Chem. Lett.* **2012**, 997-1001.
45. H.-G. Jung, J. Hassoun, J.-B. Park, Y.-K. Sun, B. Scrosati, *Nat. Chem.* **2012**, *4*, 579-585.
46. T. Zhang, H. Zhou, *Angew. Chem.* **2012**, *124*, 11224-11229.
47. M. Morita, M. Goto, Y. Matsuda, *J. Appl. Electrochem.* **1992**, *22*, 901-908.
48. M. Anouti, Y. R. Dougassa, C. Tessier, L. El Ouatani, J. Jacquemin, *J. Chem. Thermodyn.* **2012**, *50*, 71-79.

Chapter 6. Li-SO₂ battery

(The contents of this chapter has been published in *Angewandte Chemie International Edition*. Reprinted from [H.-D. Lim *et al.*, *Angew. Chem., Int. Ed.*, **2015**, *127*, 9799-9803] Copyright 2015 WILEY-VCH

6.1. Introduction

Revisiting conventional primary batteries sometimes inspires new chemistry that can be adopted in rechargeable batteries. The recent rapid growth of the Li-O₂ battery field is an example of the successful evolution from a primary battery to a secondary battery.^{1,2} Although it was previously conceived that a metal-O₂ system was only suitable for primary batteries, the current Li-O₂ system has become one of the most promising candidates for next-generation secondary batteries, specifically considering that it can deliver an exceptionally high energy density at a level unattainable by conventional lithium-ion batteries.³⁻⁵ Exploring a new chemistry in metal-gas systems plays a key role in the development of ultra-high energy density batteries, as it enables electrochemical energy storage without the use of a heavy transition metal redox host. Recent reports on various metal-gas rechargeable batteries, such as Na-O₂, K-O₂, Al-O₂, and Li-CO₂ systems,

reveal their potential applicability as high-energy-storage media with unique electrochemical properties depending on the combination of metal and gas.⁶⁻

12

The concept of a primary Li-SO₂ cell was first reported in the late 1960s.^{13,14} It operates based on the reaction between lithium ions and sulfur dioxide, which produces Li₂S₂O₄ (lithium dithionite) as a discharge product, delivering an energy density of ~ 330 Wh kg⁻¹.¹⁵⁻¹⁷ The sulfur dioxide is initially dissolved or liquefied in the electrolyte of a sealed cell with lithium metal as the anode and porous carbon as the cathode. Earlier Li-SO₂ systems needed to use a pressurized cell; however, recent works have successfully demonstrated that an ambient pressure cell is also achievable with the proper selection of an electrolyte that can dissolve a sufficiently large amount of sulfur dioxide.¹⁶ Although the Li-SO₂ cell has never been demonstrated in rechargeable conditions with a gas inlet and outlet, the chemistry resembles that of the Li-O₂ system in many ways. During discharging, the gas phase receives electrons from the electrode surface, which subsequently combine with lithium ions to finally form lithium-containing solid discharge products. The porous electrode accommodates a large amount of solid products to achieve a high capacity and gradually fill the pores, which results in an increase in the impedance of the cell and finally the end of the discharge.

Herein, we demonstrate that the charging reaction is also feasible in Li-SO₂ batteries, similar to Li-O₂, which can be reversibly operated using an organic electrolyte through the formation/decomposition of Li₂S₂O₄. The initial discharge capacity is as high as that of Li-O₂ batteries (~5,400 mAh g⁻¹); however, the energy efficiency is significantly better without the use of catalysts. The working mechanism of rechargeable Li-SO₂ batteries can guide the development of a new metal-gas system and also aid in our understanding of the current limitation of the Li-O₂ system.

6.2. Experimental Details

6.2.1. Preparation of Li-SO₂ cells

The cathode was prepared from a mixture of Ketjen black (KB) and Kynar 2801 as a binder at a ratio of 8:2. The mixture was pasted onto a Ni-mesh current collector. The individual cells were assembled in the sequence of Li metal (3/8 inch diameter), glass fiber separator (Whatman GF/D microfiber filter paper, 2.7 μm pore size), and prepared KB electrode in a Swagelok-type cell. The cathode was open to sulfur dioxide gas. Before the test, all the cells were stabilized for 30 min. The electrolyte consisted of 1 M lithium bis(trifluoromethylsulfonyl)imide (LiTFSI) in tetraethylene glycol dimethylether (TEGDME). In the catalyst-loaded electrolyte, 0.05 M LiI was added to the solvent.

6.2.2. Electrochemical characterization and analyses

The electrochemical performances of Li-SO₂ cells were investigated using a potentiogalvanostat (WonA Tech, WBCS 3000, Korea). For the electrode characterization, X-ray diffractometry (XRD, Rigaku, D/MAX-RB diffractometer, Tokyo, Japan), X-ray photoelectron spectroscopy (XPS, Thermo VG Scientific, Sigma Probe, UK), and field-emission scanning

electron microscopy (FE-SEM, Philips, XL 30 FEG, Eindhoven, Netherlands) were used. To measure the gas evolution *in-situ*, differential electrochemical mass spectroscopy (DEMS) was used. The DEMS system consisted of a mass spectrometer (MS) (HPR-20, Hiden Analytical) and a potentiogalvanostat (WonA Tech, WBCS 3000, Korea). After the discharge process, the cell was transferred to the DEMS cell. Then, the DEMS cell was fully relaxed for 12 h with argon gas flowing (10 cc min^{-1}). The evolved gases were swept by argon gas to the MS chamber during the charge process.

6.3. Results and Discussion

6.3.1. Working principles and properties of Li-SO₂ battery

The working principle of a rechargeable Li-SO₂ battery is described in Figure 6-1a. Unlike the primary battery setup, the cell design consists of an electrode that is open to a SO₂ atmosphere using a Swagelok-type cell. During the discharge process, the porous carbon cathode enables an influx of SO₂ gas and provides reaction sites for the lithium ions and SO₂ to accommodate the discharge product, Li₂S₂O₄. During the charging process, the discharge products are expected to be decomposed and evolve SO₂ gas from the electrode. Figure 6-1b shows a typical discharge/charge profile of the Li-SO₂ battery along with that of the reference Li-O₂ battery under the same operation conditions. The discharge potential and profile are in a good agreement with those of the primary cell, indicating that the SO₂ reacted electrochemically with Li ions.^{18,19} It is notable that the charging process is possible with overall electrochemical profiles similar to those of Li-O₂ cells. We observed that the charging process results in a significant amount of sulfur dioxide gas evolution, as demonstrated in Figure 6-1c. The *in-situ* DEMS experiment in Figure 6-1c detected the evolution of sulfur dioxide throughout the charging process without other gases such as carbon dioxide,

oxygen, or hydrogen. The absence of other gases implies a stable charging reaction in the cell, in contrast to conventional Li-O₂ cells, which exhibit a detectable level of carbon monoxide or dioxide evolution resulting from the partial corrosion of the carbon electrode or decomposition of the electrolyte.²⁰ The discharge capacity is comparable to that of a Li-O₂ cell; however, the voltage of the Li-SO₂ cell is higher by approximately 300 mV because the formation of the Li₂S₂O₄ discharge product yields a greater Gibbs free energy change in the reaction.²¹ Note that the charging polarization of the Li-SO₂ cell is markedly lower than that of the Li-O₂ cell even without a catalyst. The completion of the charging process could be done below 4 V. Consequently, the observed energy efficiency of the Li-SO₂ system is significantly higher than that of the Li-O₂ system. In Figure 6-1d, we used the galvanostatic intermittent titration technique (GITT) to determine the thermodynamic potential of the reaction. After full relaxations, the quasi-open circuit potential of each step is close to the theoretical voltage of Li₂S₂O₄ formation, which also supports the conclusion that the discharge/charge reaction mainly involves the formation/decomposition of Li₂S₂O₄.

6.3.2. Rechargeability of Li-SO₂ battery

Using *ex-situ* analyses, we attempted to verify that the charging process was the result of the electrochemical decomposition of Li₂S₂O₄. Figure 6-2 presents *ex-situ* X-ray diffraction (XRD) patterns of the cathode in the Li-SO₂ battery at a few stages of discharge and charge. At each step, the cathode was carefully washed using the TEGDME solvent and dried before the test. All the procedures were performed in a glove box without air exposure. The results clearly demonstrate that the gradual formation and decomposition of Li₂S₂O₄ occur on the cathode. Upon discharge to step 1, the XRD peaks begin to evolve at 33.5° and 35.4°, which correspond to the characteristic peaks observed for Li₂S₂O₄. After further discharge, the peaks grow substantially with additional peaks appearing at 27.5° and 30.1°. However, the intensities of these peaks decrease during charging and completely disappear at the end of the charge, suggesting that the decomposition of Li₂S₂O₄ primarily occurs during charging. The relatively sharp peaks of Li₂S₂O₄ appearing during a cycle are slightly different from those of the Li-O₂ cell, where the XRD signature of lithium peroxide (Li₂O₂) is sometimes difficult to detect.²²⁻²⁵ This result hints at the relatively high crystallinity of the discharge product for the Li-SO₂ battery.

Consistent with the XRD results, the crystalline size of the discharge

products was large after discharge, as observed in the SEM images in Figure 6-2. In the porous carbon electrode, the $\text{Li}_2\text{S}_2\text{O}_4$ gradually grows into a nano-ribbon-like morphology from discharge steps 1 to 3. The nano-ribbon shape of the discharge product with a length of a few micrometers and a width of hundreds of nanometers differs from the toroid or film-like morphology of Li_2O_2 ^{26,27} in Li-O₂ cells or the cubic shape of NaO_2 ^{8,28} in Na-O₂ cells. Because the morphology of the discharge products is closely related to the reaction mechanism involving the soluble intermediate discharge phase, a more detailed study will be required on this phenomenon.^{29,30} Upon full discharge to 2.0 V, the nano-ribbon fills up nearly all of the void spaces of the carbon electrode (step 3). During the charging process, the discharge product gradually disappears; after step 5 (charge to ~3.8 V), most of the ribbon-like discharge products cannot be observed, and the pristine state of the carbon electrode is recovered. Additional SEM images of the cathode at lower magnification are presented in Figure 6-3.

6.3.3. Catalyst for efficient Li-SO₂ battery

The use of catalysts could further enhance the efficiency of the Li-SO₂ cell by further reducing the charging polarization. As a model catalyst, a lithium iodide (LiI) soluble catalyst was adopted in the system, which was recently

demonstrated to be an efficient redox mediator in the decomposition of Li_2O_2 in Li-O_2 batteries.^{4,11,31} Figure 6-4a compares the electrochemical profiles of Li-SO_2 cells with (red) and without (blue) the catalyst. The addition of the catalyst led to a clear and significant decrease of the polarization during the charging process. The overall charge polarization was reduced to less than 0.3 V, which leads to a significant enhancement of the energy efficiency. Note that the oxidized form of LiI (I_2 or I_3^-) effectively decomposes $\text{Li}_2\text{S}_2\text{O}_4$ via a chemical reaction, similar to the reaction with Li_2O_2 ; however, it is more effective in the Li-SO_2 system because the equilibrium potential of $\text{Li}_2\text{S}_2\text{O}_4$ formation (~ 3.1 V) is closer to the redox potential of I/I^{3-} (or I/I_2) (~ 3.4 V) than that of Li_2O_2 formation (~ 2.96 V). Therefore, the theoretical charging efficiency using LiI in Li-SO_2 batteries can be as high as 91%, which is substantially higher than that in Li-O_2 batteries. The *ex-situ* XRD analysis (Figure 6-4b) demonstrates the reversible formation and decomposition of $\text{Li}_2\text{S}_2\text{O}_4$ within a much narrower voltage range (2.0–3.2 V) using the catalyst, which indicates that LiI could effectively decompose the discharge product. The catalytic activity of LiI in Li-SO_2 cells was also confirmed by *in-situ* DEMS analysis. The DEMS result in Figure 6-4c shows that sulfur dioxide (SO_2) was solely evolved during the charging process without any other gas evolution. Cycling of the

cell using LiI was thus possible, and under a capacity-limited condition of 500 mAhg^{-1} , the cycling continued for more than 25 cycles, as demonstrated in Figure 6-4d.

The capacity retention was not remarkable at this stage, even though $\text{Li}_2\text{S}_2\text{O}_4$ could be electrochemically decomposed as demonstrated above. Less than $1,000 \text{ mAh g}^{-1}$ could be retained after 10 cycles when operated without catalysts between 2.0–4.2 V, as shown in Figure 6-5. This performance level is only comparable to that of early Li-O₂ batteries.^{32,33} To investigate the origin of the cycle degradation, we examined the cathode after the end of the cycling process using XRD, and the results are presented in Figure 6-6a. In addition to the main discharge product, $\text{Li}_2\text{S}_2\text{O}_4$, a trace of the Li_2SO_4 phase could also be detected, which was observed to cover the surface of the cathode by SEM (inset of Figure 6-6a). It implies that the rapid deterioration of the cell is most likely due to the residual byproducts on the surface of the cathode. For a closer investigation of the formation of byproducts on the surface, the surface was characterized by X-ray photoelectron spectroscopy (XPS), as shown in Figure 6-6b and 6-6c. After the first discharge, two major peaks dominated, corresponding to $\text{Li}_2\text{S}_2\text{O}_4$ and Li_2SO_3 in Figure 6-7 (S 2p XPS) with a trace of Li_2SO_4 .¹⁶ Although the peak of $\text{Li}_2\text{S}_2\text{O}_4$ disappears after charging, which again indicates the

reversible decomposition of $\text{Li}_2\text{S}_2\text{O}_4$ during the charging process, the peaks from Li_2SO_3 and Li_2SO_4 do not completely disappear (Figure 6-6b). At the end of the cycling, residual amounts of Li_2SO_3 are still detected along with the unreacted $\text{Li}_2\text{S}_2\text{O}_4$. It is presumed that the byproducts remaining after charging are gradually deposited onto the carbon surface during cycling. This passivation layer may block the active pores while also contributing to the decrease in the electrical conductivity of the cathode. Suppression or elimination of the byproducts will be key to further enhancing the cyclability. Another practical barrier for the realization of a 'rechargeable Li-SO₂ battery' is the use of sulfur dioxide gas. Although sulfur dioxide is naturally released by volcanic activity and is widely used in winemaking as a preservative,³⁴ it is inherently a harmful gas. The emission of the gas into the atmosphere will not be desirable when charging the battery. As an alternative, in this respect, the rechargeable Li-SO₂ battery can be designed with a closed-cell type, where the circulation of the gas is confined within the cell. An interesting characteristic of SO₂ gas is that a substantially large amount of gas can be dissolved in the organic solvent, representing one of the highest solubilities among gases.³⁵ In addition, with slight pressurization, the soluble amount can be significantly increased, which explains why pressurized Li-SO₂ was one of the first systems to be commercialized in

metal-gas batteries. Even without pressurization, it is noteworthy that the recent finding on ionic liquids as an electrolyte in primary Li-SO₂ could achieve a large amount of SO₂ gas dissolution at ambient pressure, resulting in a high energy density.¹⁶ This finding implies that closed-type rechargeable Li-SO₂ batteries without the emission of harmful gases are feasible and that consideration of a smart cell design can make use of the high-energy rechargeable Li-SO₂ chemistry.

6.4. Conclusion

In summary, a rechargeable Li-SO₂ battery was demonstrated for the first time. The electrochemical formation and decomposition of Li₂S₂O₄, the major discharge product of a Li-SO₂ battery, was reversibly possible with a remarkably small charging polarization even without a catalyst. With the aid of a LiI redox mediator, it could exhibit a polarization lower than 0.3 V with one of the highest energy efficiencies achieved for Li-gas battery systems to date. The rechargeable Li-SO₂ battery could deliver approximately 5,400 mAh g⁻¹ at 3.1 V, which is slightly higher than that of the Li-O₂ battery. However, at this stage, the level of cycle performance is limited because of the formation of byproducts, which gradually deposit on the cathode and hinder the efficient cycling. Although a step forward has been made for the secondary Li-SO₂ battery system, issues such as suppression of the byproducts to enhance the cyclability and the identification of an electrolyte capable of dissolving a large amount of SO₂ gas to minimize the emission remain to be resolved. This report may provide an interesting new direction for designing rechargeable battery systems by applying a conventional primary battery chemistry to a viable secondary battery system.

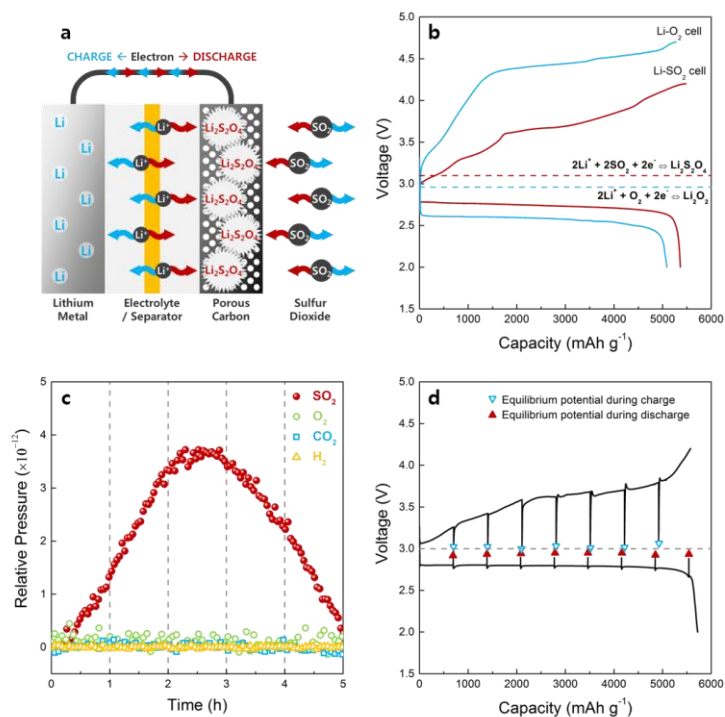


Figure 6-1. a) Schematic illustration of the concept of a rechargeable Li-SO₂ battery during discharge and charge. b) Comparison of the electrochemical profiles of Li-O₂ and Li-SO₂ batteries at a current density of 0.2 mA cm⁻². The theoretical formation potentials of Li₂O₂ and Li₂S₂O₄ are 2.96 and 3.1 V vs. Li/Li⁺, respectively. c) Gas evolution profile during charge process of Li-SO₂ cell with limited capacity of 1 mAh obtained using *in-situ* DEMS analysis. d) Galvanostatic intermittent titration technique (GITT) voltage profile of Li-SO₂ cell. The discharge capacities were calculated based on the cathode carbon weight.

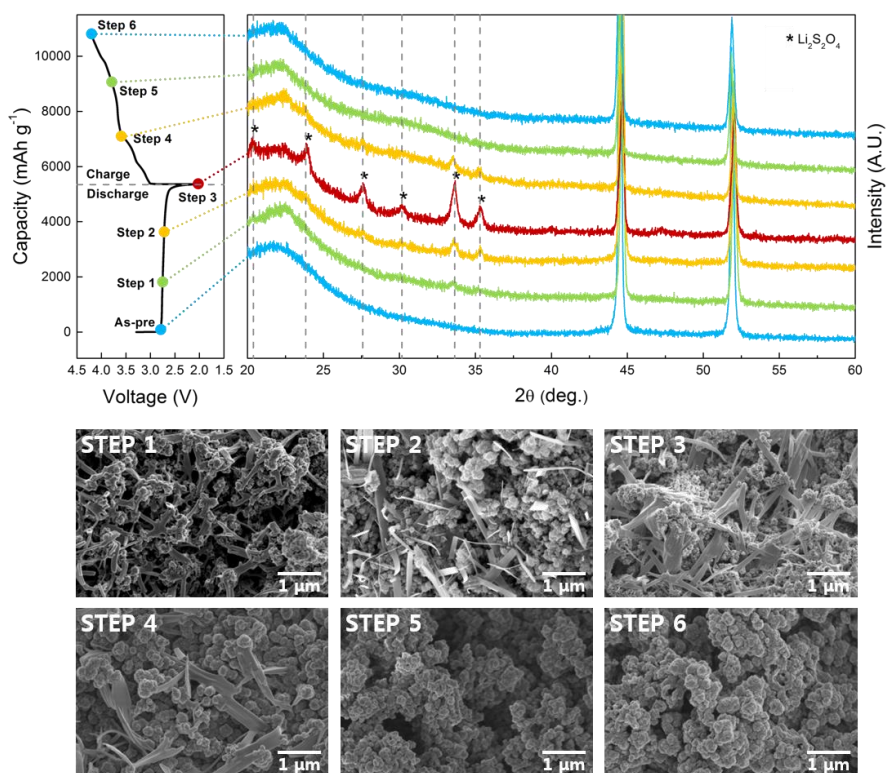


Figure 6-2. *Ex-situ* XRD and SEM analysis of a Li-SO₂ battery at each step. The dotted lines correspond to Li₂S₂O₄, and the high intensity peaks near 44° and 52° correspond to the Ni mesh current collector. All of the figures were viewed under the same magnification.

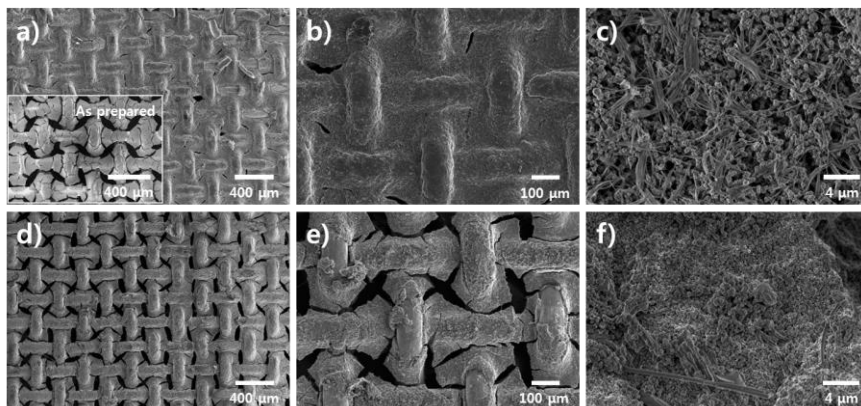


Figure 6-3. SEM images of cathode at low magnification (a-c) after the first discharge and (d-f) after re-charge (inset: SEM image of the as-prepared cathode).

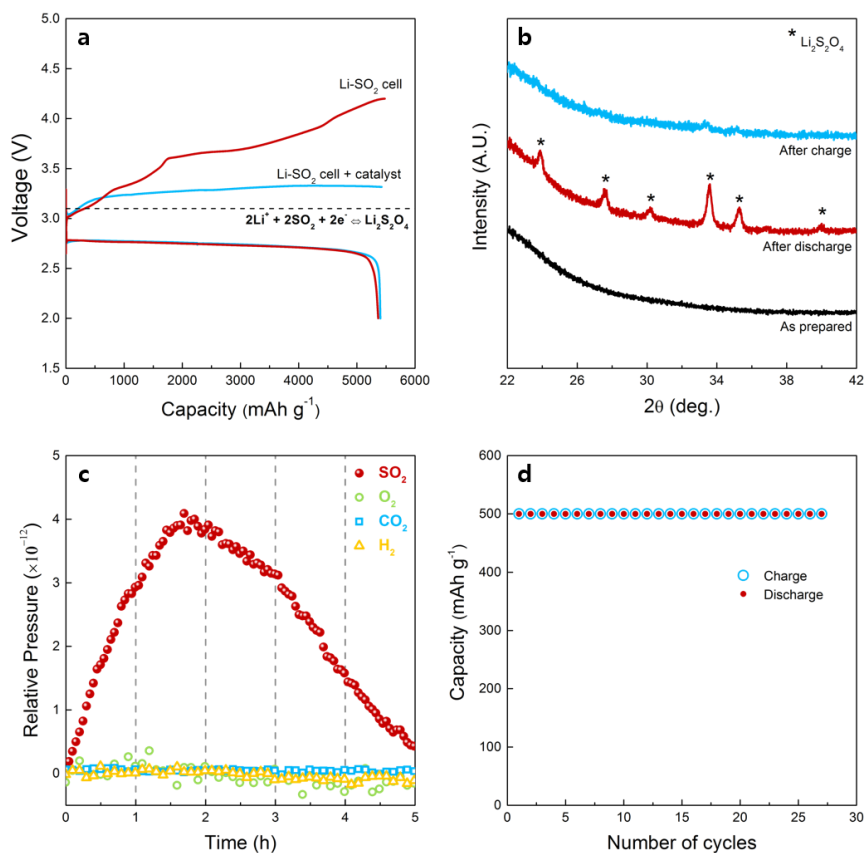


Figure 6-4. a) Comparison of the electrochemical profiles of the Li-SO₂ cell without and with a catalyst. b) XRD results of the Li-SO₂ cell using a catalyst. c) *In-situ* DEMS result; gas evolution as a function of time during the charge process of the Li-SO₂ cell with LiI catalyst. d) Cyclability of the Li-SO₂ cell with the catalyst utilized up to 500 mAh g⁻¹.

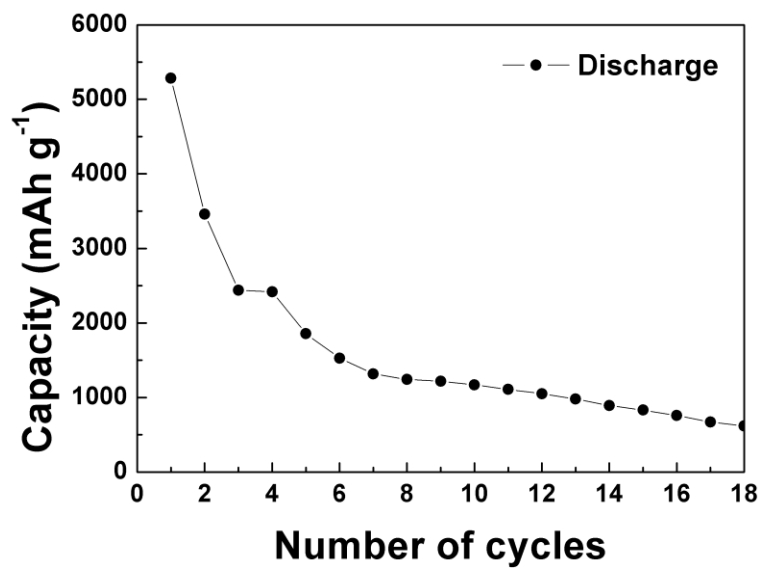


Figure 6-5. The cyclability of a Li-SO₂ battery at a constant current rate of 0.2 mA/cm² between 2.0–4.2 V.

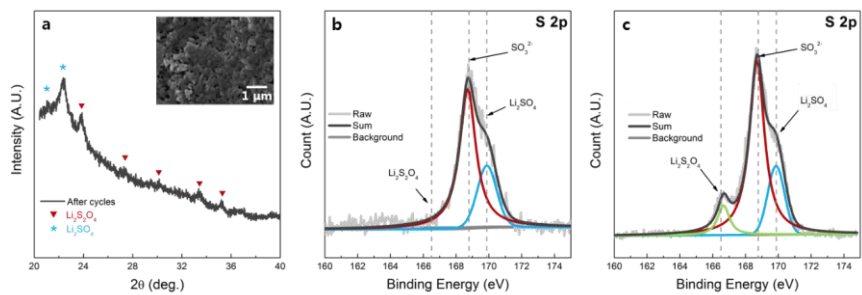


Figure 6-6. a) XRD pattern of the cathode after cycling (inset: SEM image of the cathode after cycling). XPS spectra of S 2p: b) after re-charge, and c) at the end of cycling. The overall peaks are arranged based on the reference C-C bond at 284.5 eV.

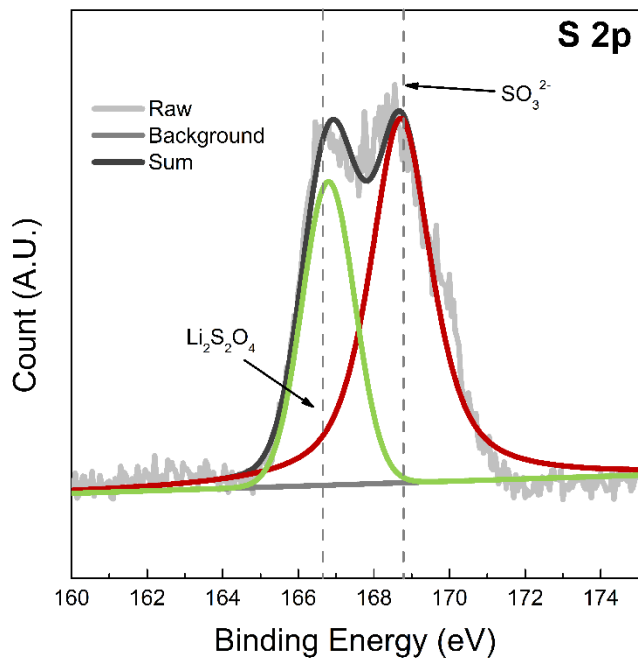


Figure 6-7. XPS spectra of S 2p after the first discharge.

6.5. References

1. K. M. Abraham, Z. Jiang, *J. Electrochem. Soc.* **1996**, *143*, 1-5.
2. P. G. Bruce, S. A. Freunberger, L. J. Hardwick, J.-M. Tarascon, *Nat. Mater.* **2012**, *11*, 19-29.
3. A. Débart, A. J. Paterson, J. Bao, P. G. Bruce, *Angew. Chem.* **2008**, *120*, 4597-4600.
4. H.-D. Lim, H. Song, J. Kim, H. Gwon, Y. Bae, K.-Y. Park, J. Hong, H. Kim, T. Kim, Y. H. Kim, X. Lepró, R. Ovalle-Robles, R. H. Baughman, K. Kang, *Angew. Chem., Int. Ed.* **2014**, *53*, 3926-3931.
5. Z. Peng, S. A. Freunberger, Y. Chen, P. G. Bruce, *Science* **2012**, *337*, 563-566.
6. R. Mori, *RSC Adv.* **2014**, *4*, 1982-1987.
7. X. Ren, Y. Wu, *J. Am. Chem. Soc.* **2013**, *135*, 2923-2926.
8. P. Hartmann, C. L. Bender, M. Vračar, A. K. Dürr, A. Garsuch, J. Janek, P. Adelhelm, *Nat. Mater.* **2013**, *12*, 228-232.
9. S. R. Gowda, A. Brunet, G. M. Wallraff, B. D. McCloskey, *J. Phys. Chem. Lett.* **2013**, *4*, 276-279.
10. K. Takechi, T. Shiga, T. Asaoka, *Chem. Commun.* **2011**, *47*, 3463-3465.
11. T. Shiga, Y. Hase, Y. Kato, M. Inoue, K. Takechi, *Chem. Commun.* **2013**, *49*, 9152-9154.
12. Y. Liu, R. Wang, Y. Lyu, H. Li, L. Chen, *Energy Environ. Sci.* **2014**, *7*, 677-681.
13. W. F. Meyers, B. Bell, J. W. Simmons, *U.S. Patent* **1969**, *3 423 242*.
14. G. T. K. Fey, *J. Power Sources* **1991**, *35*, 153-162.

15. R. L. Ake, D. M. Oglesby, W. P. Kilroy, *J. Electrochem. Soc.* **1984**, *131*, 968-974.
16. H. Xing, C. Liao, Q. Yang, G. M. Veith, B. Guo, X.-G. Sun, Q. Ren, Y.-S. Hu, S. Dai, *Angew. Chem., Int. Ed.* **2014**, *53*, 2099-2103.
17. M. W. Rupich, L. Pitts, K. M. Abraham, *J. Electrochem. Soc.* **1982**, *129*, 1857-1861.
18. B. V. Ratnakumar, M. C. Smart, R. C. Ewell, L. D. Whitcanack, A. Kindler, S. R. Narayanan, S. Surampudi, *J. Electrochem. Soc.* **2007**, *154*, A715-A724.
19. D. Linden, B. McDonald, *J. Power Sources* **1980**, *5*, 35-55.
20. M. M. Ottakam Thotiyl, S. A. Freunberger, Z. Peng, P. G. Bruce, *J. Am. Chem. Soc.* **2012**, *135*, 494-500.
21. R. A. Huggins, *Advanced batteries: materials science aspects*, Springer Science **2008**, New York, pp. 159-195.
22. D. Zhai, H.-H. Wang, K. C. Lau, J. Gao, P. C. Redfern, F. Kang, B. Li, E. Indacochea, U. Das, H.-H. Sun, H.-J. Sun, K. Amine, L. A. Curtiss, *J. Phys. Chem. Lett.* **2014**, *5*, 2705-2710.
23. D. Oh, J. Qi, Y.-C. Lu, Y. Zhang, Y. Shao-Horn, A. M. Belcher, *Nat Commun* **2013**, *4*, 2756.
24. J. Hassoun, H.-G. Jung, D.-J. Lee, J.-B. Park, K. Amine, Y.-K. Sun, B. Scrosati, *Nano Lett.* **2012**, *12*, 5775-5779.
25. C. Shang, S. Dong, P. Hu, J. Guan, D. Xiao, X. Chen, L. Zhang, L. Gu, G. Cui, L. Chen, *Sci. Rep.* **2015**, *5*, 8335.
26. S. Ganapathy, B. D. Adams, G. Stenou, M. S. Anastasaki, K. Goubitz, X.-F. Miao, L. F. Nazar, M. Wagemaker, *J. Am. Chem. Soc.* **2014**, *136*, 16335-16344.

27. B. D. Adams, C. Radtke, R. Black, M. L. Trudeau, K. Zaghbi, L. F. Nazar, *Energy Environ. Sci.* **2013**, *6*, 1772-1778.
28. P. Hartmann, C. L. Bender, J. Sann, A. K. Durr, M. Jansen, J. Janek, P. Adelhelm, *Phys. Chem. Chem. Phys.* **2013**, *15*, 11661-11672.
29. L. Johnson, C. Li, Z. Liu, Y. Chen, S. A. Freunberger, P. C. Ashok, B. B. Praveen, K. Dholakia, J.-M. Tarascon, P. G. Bruce, *Nat Chem* **2014**, *6*, 1091-1099.
30. N. B. Aetukuri, B. D. McCloskey, J. M. García, L. E. Krupp, V. Viswanathan, A. C. Luntz, *Nat Chem* **2015**, *7*, 50-56.
31. M. Yu, X. Ren, L. Ma, Y. Wu, *Nat Commun* **2014**, *5*, 5111.
32. S. A. Freunberger, Y. Chen, Z. Peng, J. M. Griffin, L. J. Hardwick, F. Bardé, P. Novák, P. G. Bruce, *J. Am. Chem. Soc.* **2011**, *133*, 8040-8047.
33. H.-D. Lim, K.-Y. Park, H. Gwon, J. Hong, H. Kim, K. Kang, *Chem. Commun.* **2012**, *48*, 8374-8376.
34. B. W. Compton, *Sulfur Dioxide: Properties, Applications and Hazards*, Nova Science Publishers **2011**, New York.
35. P. G. T. Fogg, W. Gerrard, *Solubility of gases in liquids : a critical evaluation of gas/liquid systems in theory and practice*, J. Wiley **1991**, New York.

초 록

차세대 대용량 전지의 개발은 미래 전기자동차 시장에 핵심 요소로 평가되고 있다. 다양한 차세대 전지 후보군 중, 금속-공기 시스템이 가장 유력하다. 이는 금속-공기 전지가 기존의 리튬 이차전지 보다 월등히 뛰어난 에너지 밀도를 갖고 있기 때문이다. 그 중에서도 특히, 리튬-산소 전지는 차세대 대용량 에너지 저장소재로 큰 관심을 받고 있다. 기존의 리튬 이차 전지는 LiCoO_2 나 LiFePO_4 와 같이 무거운 전위 금속이나 결정 구조체를 필요로 하는 반면, 리튬-산소 전지는 무거운 결정 구조체 없이 리튬 이온과 산소가 직접적으로 전극 표면에서 반응하기 때문에, 다양한 배터리 종류 중에서 가장 높은 이론 에너지 밀도를 갖고 있다. 하지만, 이러한 높은 에너지 밀도의 장점에도 불구하고, 낮은 수명 특성과 율 특성이 문제가 되고 있다. 많은 연구자들이 이 문제들을 해결하려고 노력했지만, 여전히 리튬-산소 전지의 단점으로 남아있다. 따라서, 최근에는 리튬-산소 전지의 전반적인 전기화학 특성을 향상 시키기 위한 다양한 연구가 진행 되고 있다.

본 논문의 각 장에서는 리튬-산소 전지의 성능 향상을 위한 다양한 접근 방법들이 제시되어 있다. 또한 새로운 종류의 금속-공기 시스템인 리튬-이산화탄소 전지와 리튬-이산화황 전지도 다루고 있다. 각 장의 요약은 아래와 같다.

제 2장에서는 탄소나노튜브 직물을 이용하여 새로운 리튬-산소 전지용 양극 구조체를 설계한 것을 다루고 있다. 정렬된 탄소나노튜브로부터 다공성 탄소 전극을 제작하였으며, 이 구조체가 리튬-공기전지의 수명특성과 율 특성을 크게 향상시켰다. 제작된 직물 탄소나노튜브 구조체는 과산화리튬(Li_2O_2)의 생성과 분해를 용이하게 하였으며, 이를 통해 전지의 수명특성을 향상시켰다. 리튬-산소 전지용 전극 소재로써의 탄소나노튜브 직물의 기계적 성질과 높은 전기 전도성에 대한 내용을 다루고 있다.

제 3장에서는 다공성의 탄소나노튜브 구조체에 촉매를 담지 한 새로운 형태의 전극을 다루고 있다. 간단한 촉매 담지 방법을 이용하여 촉매 특성 발현에 효율적인 구조체를 설계 하였으며, 이를 통해 빠른 전류 속도에서도 100회 넘는 수명특성을 달성 하였다. 추가적으로 Pt 촉매가 방전 산화물에 끼치는 영향을 분석하였으며 수명 특성과의 관계를 설명하고 있다.

제 4장에서는 나노 다공성 구조체에 리튬-산소 전지용 액상 촉매를 적용한 분석 결과를 다루고 있다. 나노 다공성의 공기극에 LiI 액상 촉매를 동시에 적용함으로써 전지 성능을 크게 향상시켰다. 탄소나노튜브 직물 구조체는 많은 기공들을 갖고 있으며, 이 기공을 통해 액상 촉매가 자유롭게 이동할 수 있다. 액상 촉매의 이동에 용이한 구조를 사용하여 촉매 효율을 증가 시켰기 때문에, 에너지 효율과 수명특성이 동시에 증가하였다. 액상 촉매의 사용과 효율적인 구조체의 동시 적용은 앞으로의 에너지 저장 소재 개발에 중요한 지표가 될 것이라 평가 된다.

제 5장에서는 CO₂가 리튬-산소 전지에 미치는 영향을 양자 계산과 실험을 통해 다루고 있다. 지금까지의 리튬-공기 전지는 순수한 산소 분위기에서 연구 되었으며, 이러한 이유로 주로 리튬-산소 전지라 불린다. 따라서 본질적 의미로써의 리튬-공기 전지를 달성 하려면, 실제 공기 중에 있는 다른 성분 (예: N₂, Ar, CO₂) 의 영향에 대해 연구 되어야 한다. 특히, CO₂는 전지에 사용되는 전압 내에서 리튬과 반응하여 Li₂CO₃를 형성 할 수 있기 때문에 고려 되어야 한다. 본 장에서는 CO₂가 리튬-산소 전지에 끼는 영향을 분석 하였으며, CO₂가 존재 할 경우 반응 경로가

전해질에 따라 변한다는 것을 증명하였다. 제일계산을 통해 반응 경로를 예측하고 실험을 통해 증명 하였다.

새로운 유형의 금속-공기 전지 시스템에 대한 연구는 차세대 대용량 에너지 저장소재를 개발하는데 중요 발판이 된다. 제 6장에서는 새로운 종류의 금속-공기 전지 인 리튬-이산화황 전지에 대해서 다루고 있다. 이산화황 전지는 넓은 가용 온도 범위와 큰 에너지 밀도 및 긴 유통기한으로 군용으로 널리 사용 되었다. 그동안의 리튬-이산화황 전지는 일차 전지로서 사용 되었지만, 본 연구에서는 반응물인 $\text{Li}_2\text{S}_2\text{O}_4$ 를 가역적으로 형성/분해 시킴으로써 2차 전지로서의 리튬-이산화황 전지의 가능성을 평가 하였다. 결과적으로 촉매 없이도 기존의 리튬-산소 전지 보다 높은 에너지 효율을 보인다.

본 논문에 제시되어 있는 다양한 접근 방법들은 금속-공기 전지의 발전에 기여할 수 있을 것이며, 차세대 금속-공기 전지의 방향에 대한 새로운 시각을 제시해 줄 것이다.

주요어: 배터리, 에너지 저장, 공기 전지, 산소 전지, 촉매, 리튬 이산화황 전지, 액상 촉매

학 번: 2011-30942